Commissioning of the GEM Detectors in the COMPASS Experiment

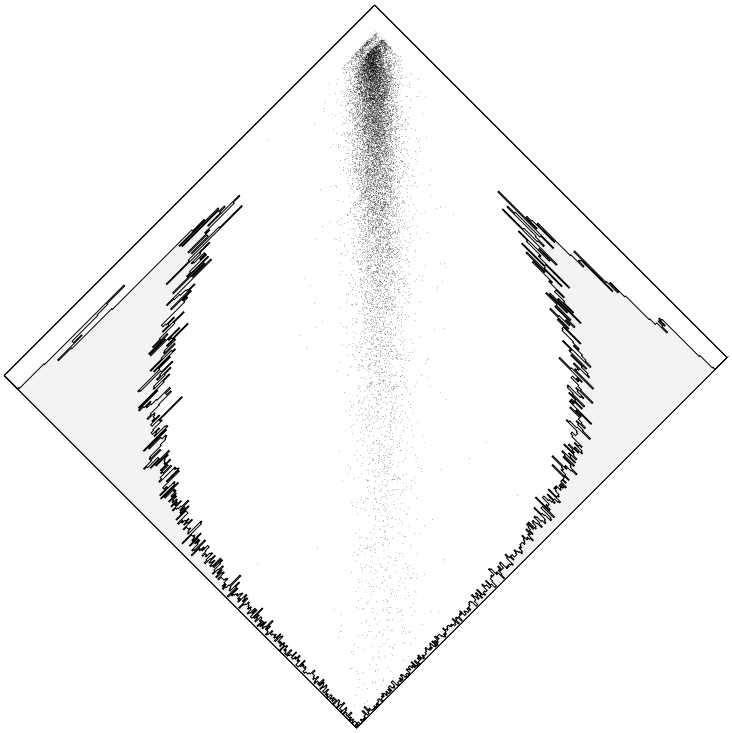

Diploma Thesis

Frank Simon

Physik–Department E18
Technische Universität München
November 2001

The cover picture shows the charge correlation between both readout coordinates of a COMPASS triple–GEM, as observed with a mixed proton and pion beam of 3.6 GeV/c. The projections on the axes yield the Landau distribution of the generated charge.

Abstract

The COMPASS experiment at the SPS accelerator at CERN uses GEM detectors as the main components of the inner tracking system. This thesis starts with a review of the physical principles of these micro–pattern gas detectors and with a survey of the COMPASS triple–GEM design and then covers the commissioning phase of the detectors, the main part of this work. The properties of the detectors have been studied in the laboratory and in particle beams. With an X–ray source, the gain and its homogeneity were measured, showing a non–uniformity of less than $\pm 15\%$ over the detector surface. The analysis of test beam data, taken with a 3.6 GeV/c mixed proton and pion beam from the CERN PS, yields an efficiency of $99.0 \pm 0.1\%$ in active regions at nominal gain and a spatial resolution of $46 \pm 3\,\mu$m. Successful operation of the GEMs in the start–up phase of the COMPASS physics running shows that these detectors fulfill the requirements for high-resolution tracking in the environment of intense muon beams.

Contents

Appendix

List of Figures

Chapter 1

Introduction

The aim of particle physics is the understanding of the constituents of matter and of the interactions that govern their behavior. The powerful microscopes used in this research are the accelerators which enable physicists to penetrate to ever deeper levels of the structure of matter. Today we know that the nucleons, the protons and neutrons that make up the atomic nucleus, are themselves made up of constituents, the quarks. The quarks in the nucleon are confined by the strong interaction which is mediated by massless messenger particles dubbed gluons. The gluons carry the charge of the strong interaction, called color, unlike the photon in Quantum Electrodynamics. This leads to the rich structure of Quantum Chromodynamics.

A new experiment set out to study the properties of hadrons, particles consisting of quarks held together by gluons, is COMPASS [1] which currently begins with data taking at CERN. COMPASS is a scattering experiment, where a beam of high energy particles scatters off a fixed target which contains the matter under study or which provides a suitable arena, if it is the projectile that is to be investigated.

In order to measure the desired quantities, the reactions in the target have to be reconstructed from the particles that fly out into the experimental setup. To trace these particles through the complex apparatus, tracking detectors are used. They record the positions where they were traversed by charged particles and permit the reconstruction of each particle track.

Tracking detectors exist in many different varieties and operate on different physical principles, depending on the type of particle that has to be tracked, on the desired spatial resolution, and on the area that has to be covered. Micro–pattern gas detectors, operating on the principle of electron amplification in gases, provide good spatial resolution for charged particles down to 50 μm and can be built with large sensitive areas. Following the invention of the micro–strip gas chamber (MSGC) by A. Oed in 1988 [2], a variety of such micro–pattern detectors has been developed, based on photolithographic production techniques. The newest development is the gas electron multiplier (GEM) [3].

The study of the properties and the commissioning of GEM–based tracking detectors for the COMPASS experiment is the topic of this thesis. It describes the principles of these detectors leading to the design used for the COMPASS GEMs. A quality control procedure was developed to ensure the functionality of the detectors prior to their installation in the COMPASS experiment by measuring in the laboratory properties such as gain and energy resolution for X–rays. During a test beam time in April 2001, two complete GEM detectors were studied extensively using a mixed secondary beam of 3.6 GeV/c protons and pions from the CERN Proton Synchrotron. The analysis of the test beam data and the results concerning efficiency, signal timing, and spatial resolution are presented, as well as first results from the operation of 14 GEM detectors in the COMPASS spectrometer for the physics running that started in July 2001.

Chapter 2

The COMPASS Experiment

COMPASS (**CO**mmon **M**uon and **P**roton **A**pparatus for **S**tructure and **S**pectroscopy) [1] is a new high–luminosity fixed–target experiment. Over the last years it has been installed at the Super Proton Synchrotron accelerator (SPS) at CERN[1] and began data taking in Summer 2001.

The COMPASS experiment is a multi–purpose experiment designed to investigate the properties of the nucleon, the building block of the atomic nucleus. This chapter gives a short overview of the various physics objectives and of the detector itself.

2.1 Physics Objectives

The physics program of COMPASS is based on two approaches, requiring either a muon or a hadron beam.

The main goal of the muon program is the measurement of the gluon polarization of the nucleon. As first observed by the EMC experiment [4, 5] and further established by the SMC experiment [6], the experiment E142 [7] at SLAC, and the HERMES experiment [8] at DESY, the spin of the nucleon is not simply given by the spins of the valence u and d quarks. One possible explanation of this phenomenon is that the gluons in the nucleon also contribute to the total nucleon spin. The spin contribution of the gluons will be measured using deep inelastic scattering of a polarized muon beam on a polarized target. This is done by studying the cross section asymmetry for open–charm production in a process called photon–gluon fusion. In this process the incident muon interacts with a gluon in the nucleon via a virtual photon. The gluon and the photon form a $c\overline{c}$ pair which subsequently breaks up into charmed hadrons.

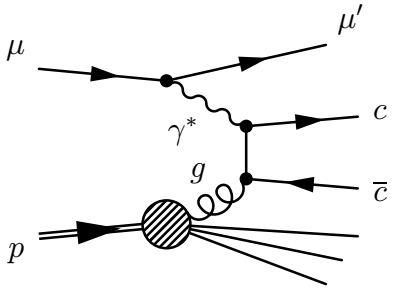

Figure 2.1: Photon–gluon fusion.

[1] European Laboratory for Particle Physics, Geneva, Switzerland

Figure 2.1 shows the principle of open–charm production via photon–gluon fusion. The reaction offers a clean way to determine the gluon polarization since due to the large charm quark mass the background of charmed hadrons originating from possible $c\overline{c}$ fluctuations in the nucleon is negligible.

Another possible contribution to the spin of the nucleon is due to the existence of a negatively polarized sea of strange quarks and antiquarks. This component is accessible via the measurement of the polarization of Λ hyperons created in target fragmentation. To study this, a polarized muon beam is scattered on an unpolarized target.

The second part of the COMPASS physics program uses hadron beams (protons, pions, and kaons). One intention is the search for exotic hadrons. Since gluons carry color charge, it is in principle possible to construct bound states containing valence gluons. Such particles are called glueballs if they contain only gluons, or hybrids if they consist of valence quarks and valence gluons. So far, the best candidate for a glueball is the $f_0(1500)$[11]. To find exotic hadrons, high statistics and a good reconstruction of the decay mechanisms is necessary.

Another aspect of the hadron program is the study of charmed baryons. Up to now, 10 singly–charmed baryons are known. Their mass scale is given by $m(\Lambda_c^+) = 2284.9$ MeV/c^2, the lightest singly–charmed baryon with a quark structure of $\Lambda_c^+ = udc$. So far, no experimental information exists about doubly–charmed baryons. They probably resemble structures with a heavy cc–diquark in the center surrounded by a third light quark. States such as ccu are expected to have a mass around 3.6 GeV/c^2. A problem in the study of these ccq baryons is their very low production cross section. It is expected that a high–rate experiment such as COMPASS will yield about 100 fully reconstructed ccq events.

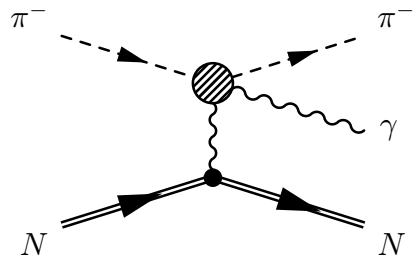

Figure 2.2: Primakoff scattering.

An additional goal of COMPASS is the study of mesonic structure via Primakoff scattering [10]. This is Compton scattering with a virtual photon in inverse kinematics. A pion scatters off a nucleus via a quasi–real photon from the electric field of the nucleus, producing a real photon as illustrated in figure 2.2. Reactions like this offer access to quantities such as the polarizability of the pion.

2.2 Experimental Arrangement

The COMPASS spectrometer is a two–stage magnetic spectrometer. Due to their different angular acceptance, the stages cover different momentum regions. Par-

ticles with a momentum above 10 GeV/c enter the second stage. Thus, the full spectrometer allows precise measurements over an extended momentum range.

Both stages are equipped with small area and large area tracking, particle identification, electromagnetic and hadronic calorimeters, and with muon identification. To a large extent the setup remains unchanged for the different physics programs.

All measurements envisaged at COMPASS require high statistics and a precise reconstruction of the reactions of interest, thus good resolution and high rate capability throughout the spectrometer are mandatory. The intensities of the different beam types and the expected trigger rates are summarized in table 2.1.

Particles	Intensity / pulse	Momentum	trigger rate
μ	2×10^8	up to 190 GeV/c	100 kHz
p, π, K	1×10^8	up to 300 GeV/c	10 - 100 kHz

Table 2.1: COMPASS beam parameters.

The SPS beam has a time structure with ~ 4 s particle extraction (spill) in a cycle of ~ 18 s. The high trigger rates require elaborate readout systems with data reduction at the detector front–ends and are a challenge for the DAQ system.

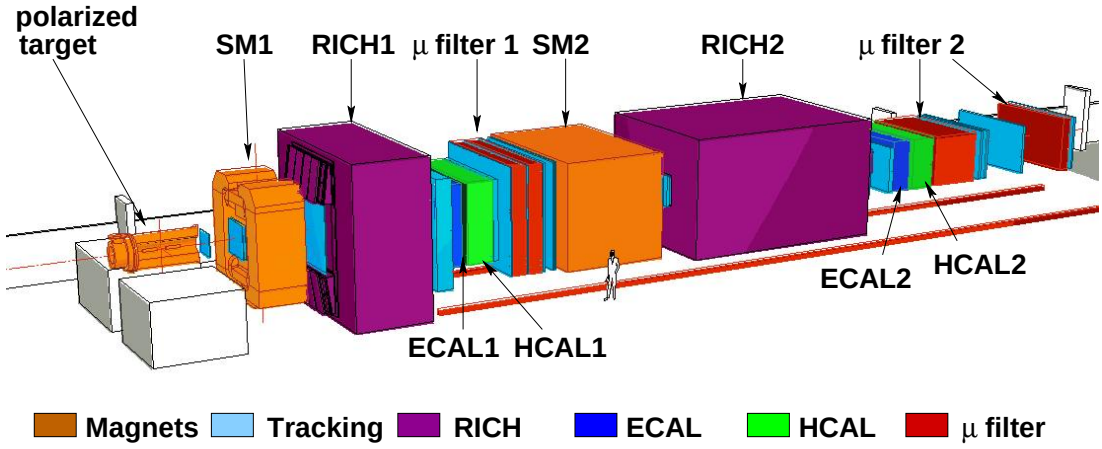

Figure 2.3: Artist's view of the COMPASS spectrometer.

Figure 2.3 shows a sketch of the full COMPASS setup with target and both spectrometer stages. The detectors are colored according to their task in the experiment.

For the muon program a polarized target is used. It consists of a superconducting solenoidal magnet, a dilution refrigerator to reach the necessary low temperatures, and the target material itself. To be able to extract quantities for protons and neutrons, two target materials are used: NH_3 and ^{6}LiD. NH_3 contains three independent protons and is well polarizable. To measure neutron data, polarized deuterons are used, since free neutrons are not polarizable. Here, ^{6}LiD is chosen because the ^{6}Li

nucleus resembles an α particle together with a deuteron, which can be polarized, in addition to the deuteron in the LiD molecule.

For the hadron program different target types will be used, depending on the goal of the measurements. For the reconstruction of the short–lived charmed baryons, tracking in the target is needed. This can be achieved by an active target, a dense arrangement of target material and silicon micro–strip detectors. For Primakoff measurements a heavy target will be used.

Upstream of the target, silicon micro–strip trackers and scintillating fibers are used for beam definition. Between the target and the first spectrometer magnet (SM1), scintillating fibers and micromegas[2] are used for small area tracking, and drift chambers for large area tracking. The tracking immediately behind SM1 is done with straw trackers for large angles and GEM detectors, the subject of this work, for small angles. Downstream of the first RICH all tracking stations are made up out of MWPCs[3] for large angles and GEMs for small angles. To have tracking inside the beam, the center of the GEM detectors will be covered by silicon micro–strip detectors.

Separation of pions, kaons, and protons is provided by the two RICH[4] detectors. Currently, the first RICH is installed. It provides pion, kaon, and proton identification in the momentum interval of 3 - 55 GeV/c. The second RICH, to be installed in the future, is foreseen to allow particle identification up to momenta of 120 GeV/c.

The energy of the particles is measured in the electromagnetic (for photons and electrons) and hadronic calorimeters (for hadrons). Since they stop the particles they are intended to measure, the calorimeters are located at the downstream end of each spectrometer stage.

The final part of the COMPASS spectrometer are the muon filters. Muons do not interact via the strong interaction and have a small energy loss due to their large mass. In order to isolate muons other particles are filtered out by iron absorbers. The muons are tracked by drift tubes behind the absorbers. This muon identification is especially important in the muon program and to detect muons from semi–leptonic decays ($\Lambda_c^+ \to \Lambda\mu^+\nu_\mu$ for example) in the hadron program.

[2] **Microme**sh **gas** detector
[3] **M**ulti**W**ire **P**roportional **C**ounter
[4] **R**ing **I**maging **CH**erenkov counter

Chapter 3

The GEM Concept

This chapter gives an overview of the physical processes exploited in the Gas Electron Multiplier and outlines the principles of GEM detectors.

3.1 The Primary Process

A fast charged particle, traversing a detector, will interact with the detector medium in many different ways. Ideally, the impact on the tracked particle has to be kept to a minimum in order not to disturb the track. For the GEM concept, incoherent Coulomb interaction with the electrons in the atomic shells of the detector medium is exploited. Other interaction types do not contribute to the signal in the detector and have to be suppressed as much as possible by the design of the detector.

3.1.1 Ionization Energy Loss of charged Particles

For not too high energies, relativistic charged particles, except electrons, lose energy in matter primarily by ionization. The mean rate of energy loss dE/dx is described by the well known Bethe–Bloch equation, for a discussion see for example [11]. Figure 3.1 shows the calculated energy loss for muons in argon over a wide momentum range. The density effect, which leads to a truncation of the logarithmic rise of the energy loss for very high energies, is not included in the calculation. Since this effect scales with the density of the material, it is much larger for solids and liquids than for gases. The error introduced by this omission is less than 4% at a momentum–over–mass ratio $\beta\gamma$ of 1000. The particles in COMPASS have $\beta\gamma$ between ~ 10 and ~ 1000.

The energy loss has a global minimum for particles with $\beta\gamma$ between 3.0 and 3.5, depending on the Z of the stopping medium. Particles with an energy loss close to this minimum are called minimum–ionizing particles or MIPs. In practical cases,

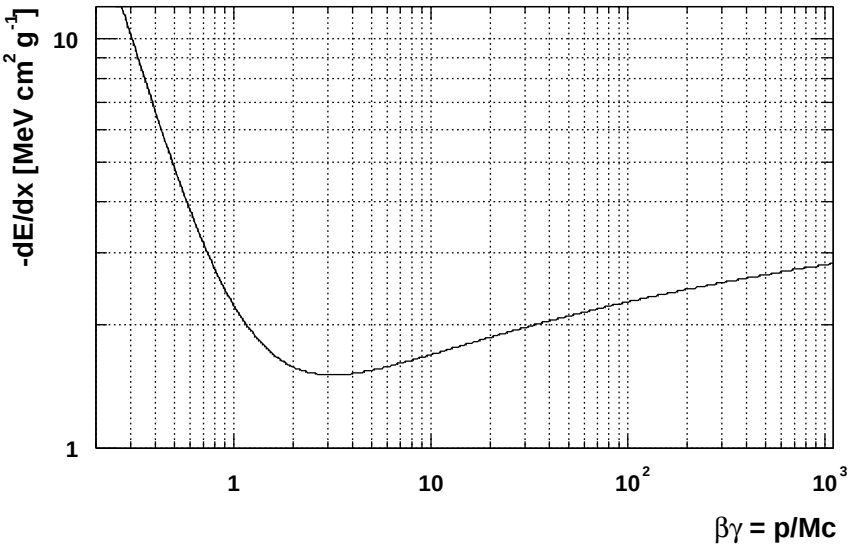

Figure 3.1: dE/dx according to Bethe–Bloch for pions in gaseous argon, without density effect.

most relativistic particles have an energy loss close to this minimum and can be regarded as MIPs. Since the ionization energy loss scales with the square of the particle's charge and increases significantly for low momenta, nuclear fragments generated in strong interaction processes of the MIP particles with the detector material have an energy loss several orders of magnitude higher than MIPs. This can cause discharges in the detectors.

3.1.2 Energy Loss Distribution

The interaction of particles passing through matter is taking place via discrete events. Therefore the energy loss in a layer of thickness δx, given by $(dE/dx)\delta x$, is a statistical quantity. The distribution is skewed towards high values and can be described by a Landau distribution. Only for thick absorbers and correspondingly large energy loss the distribution is nearly Gaussian. The large fluctuations in the energy loss are due to a small number of collisions with large energy transfers, leading to the so–called δ–electrons[1].

In order to limit scattering processes in the detector material tracking detectors have to be constructed as thin as possible. As a consequence, the energy loss has to be treated according to the thin layer model. In a classical formulation due to Landau

[1]Electrons ejected with an energy above a few keV are called δ–electrons

the energy loss distribution in thin media is expressed as

$$f(\lambda) = \frac{1}{\sqrt{2\pi}} e^{-\frac{1}{2}(\lambda + e^{-\lambda})}, \tag{3.1}$$

where λ is the normalized deviation of the energy loss from the most probable energy loss ΔE_{mp},

$$\lambda = \frac{\Delta E - \Delta E_{mp}}{\xi}. \tag{3.2}$$

In this equation, ΔE is the actual energy loss of a particle in the layer. ξ is given by [13]

$$\xi = 0.153 \frac{Z}{A} \frac{\text{MeV}}{\text{g/cm}^2} X_{Layer}. \tag{3.3}$$

Here the numerical factor is half of the corresponding factor in the Bethe–Bloch equation (see [11]), which gives the scale of the energy loss of the particle, Z is the atomic and A the mass number of the medium, and X_{Layer} is the thickness of the layer in units of g/cm^2. The parameter ξ is related to the full width at half maximum of the Landau distribution by the relation $\Delta_{fwhm} = 4.02\,\xi$. A Landau distribution with $\xi = 0.5$ and $\Delta E_{mp} = 1$ (both in arbitrary energy units) is shown in figure 3.2.

For a discussion of the dynamics of energy loss, one has to distinguish between primary ionization and total ionization. If a charged particle passes through matter it loses its energy by a discrete number of primary ionizing collisions. These collisions liberate electron–ion pairs in the medium. The ejected electrons can have enough energy to ionize, thus producing secondary ion pairs. The sum of the primary and secondary ionizations is the total ionization, and the total number of ion pairs produced per unit length by the passage of the charged particle can be expressed by

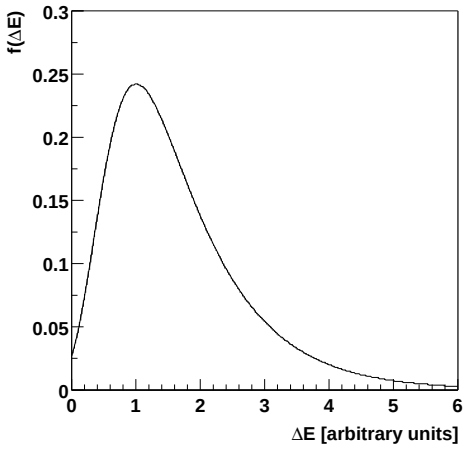

Figure 3.2: Landau distribution.

$$n_t = \frac{1}{W_i} \frac{dE}{dx}, \tag{3.4}$$

where dE/dx is the specific energy loss and W_i is the effective average energy needed to produce one electron–ion pair. In Argon, a frequently used detector gas, $W_i = 26$ eV. This value is substantially larger than the ionization energy (15.7 eV for Ar), since in addition to ionization, excitation processes occur, lifting electrons to higher bound states, but which do not lead to electron–ion pairs.

The number of primary pairs n_p is roughly linearly dependent on the average atomic number of the gas. For gaseous Argon, $n_p = 29.4$ ion pairs/cm at atmospheric pressure. These primary reactions lead to a total of $n_t \sim 100$ electron–ion pairs/cm.

The interactions that cause the primary ionization follow Poisson statistics, since they are a small number of independent events. For a distribution characterized by an average number n of primary interactions, the probability for k interactions in a given event is

$$P_k^n = \frac{n^k}{k!} e^{-n} . \tag{3.5}$$

Since the detection of a particle requires at least one primary interaction, the maximum possible efficiency of a detector is given by

$$\epsilon = 1 - P_0^n = 1 - e^{-n} . \tag{3.6}$$

For the COMPASS GEM detectors with a drift gap of $\delta x = 3$ mm, and thus $n = n_p \delta x \approx 9$, the maximum theoretical efficiency (if the detector is able to detect single electrons) is 99.99%. For a real detector, the signal has to be above the noise level to be detected, thus reducing the efficiency from this theoretical number.

3.2 Diffusion, Drift, and Gas Multiplication

Diffusion and drift influence the behavior of the charge cloud in the gas volume outside the amplification region of a detector. In the amplification region, the principle of gas multiplication is exploited.

3.2.1 Diffusion

In the absence of an electric field charged particles assume the average thermal energy distribution of the gas by multiple collisions. They diffuse following a Gaussian law. The diffusion is characterized by the diffusion coefficient D. The standard deviation of the distribution of charge originating from a localized charge at $t = 0$ after a time t is given by

$$\sigma_x = \sqrt{2Dt}, \tag{3.7}$$

with the diffusion coefficient D depending on the mass of the charged particles. For free electrons, the diffusion coefficient is much higher than for ions. Diffusion coefficients for electrons in Ar are of the order of 200 - 300 cm^2/s.

3.2.2 Uniform Drift

The application of a uniform electric field across the gas volume causes a movement of the charge carriers along the field direction (positive particles move in the direction of the field, negative particles in the opposite direction). This behavior is called drift. The drift velocity depends on the electric field and on the mean free path between collisions in the gas.

In the plane perpendicular to the field, the diffusion is unchanged from the field–free case, but in the direction of the electric field, the diffusion coefficient changes, depending on the magnitude of the field. The drift velocity of electrons in Ar:CO_2 (70/30) (the gas mixture used in the COMPASS GEM detectors) can be taken from figures in [17]. For drift fields between 2 kV/cm and 3 kV/cm (typical for the GEM detectors), the drift velocity is about 6 cm/μs.

Due to the statistical nature of the primary ionization the drift limits the time resolution of a gas detector to approximately 5 ns, given by the uncertainty of the time of arrival for the electron cluster produced at the end of the drift gap.

3.2.3 Gas Multiplication

The main feature of a gaseous detector, such as the GEM detectors, is gas multiplication. Since the total charge n_t generated by the passage of a minimum–ionizing particle is much too small to be detected by readout electronics, this charge has to be amplified before it can be read out. For this amplification, the behavior of electrons in electric fields inside a gas filled volume is exploited.

While electrons drift in moderate electric fields, an increase of this field above a few kV/cm lets the electrons receive enough energy between two collisions to participate in inelastic processes, namely excitation and ionization. If the energy of an electron exceeds the first ionization potential of the gas (15.7 eV for Argon), the result of a collision can be an ion pair, leaving the incident electron free to continue in the electric field. The probability for ionization rapidly increases above threshold and in typical gases has a maximum for electron energies around 100 eV (see [12]).

The number of electron ion–pairs produced per unit length of drift by one primary electron is called the first Townsend coefficient, α. It is the inverse of the mean free path for electrons. For small α the coefficient increases linearly with the energy of the electrons.

Inelastic processes are the basis of avalanche multiplication, as can be seen from the increase of the number of electrons after a path dx, i.e., $dn = n\alpha\, dx$. By integration, the total number of electrons n and the gain G after a distance x are

$$n = n_0 e^{\alpha x} \quad \text{and} \quad G = \frac{n}{n_0} = e^{\alpha x}\,. \tag{3.8}$$

However, there is a limit for the multiplication process, given by the increase of probability for secondary processes, such as avalanches induced by photon emission, and by space–charge deformation of the electric field. The electric field is strongly increased near the front of the avalanche and can lead to a spark breakdown. A phenomenological limit for the gain before breakdown is given by the Raether condition $\alpha x \sim 20$ which is equivalent to $G \sim 10^8$. The statistical distribution of the electron energy and the resulting uncertainty in α limit the gain for safe operation to $G \sim 10^6$.

3.3 Detector Gas

In principle, avalanche multiplication is possible in any gas or gas mixture. For detector applications however the choice of the gas is restricted by specific requirements such as a low operating voltage, high stability, and high gain.

In noble gases, gas multiplication occurs at lower fields than in gases composed of complex molecules, making noble gases the main component of most detector gas fillings. To detect minimum–ionizing particles, high specific ionization is necessary to generate a sufficient amount of primary charge. The specific ionization increases with the atomic number of the gas atoms, and since xenon and krypton are expensive the natural choice is argon.

In the avalanche process excited and ionized atoms are produced, which have to return to their ground state. Excited noble gas atoms can only return to their ground state through the emission of a photon. The minimum energy of this photon is 11.6 eV for argon, which is well above the ionizing potential of the copper electrodes in the detector, and which therefore can release electrons that cause new avalanches. The same effect can be caused by ionized argon atoms being neutralized on the cathode, radiating the energy balance as a photon.

Since these additional avalanches can cause permanent discharges, the photons responsible for their creation have to be absorbed before they reach the electrodes. For this, polyatomic molecules are well suited, since they have a large amount of non–radiative rotational and vibrational excited states which allow the absorption of photons over a wide energy range. The energy is subsequently dissipated by collisions or by dissociation of the molecule. Such gases are called quenchers and make up the smaller part of a detector gas mixture.

The quenching efficiency increases with the number of atoms in the molecule, making isobutane an often used component. However, organic gases cause polymer deposits on the electrodes which change the detector characteristics and lead to discharges after extended irradiation (aging). In addition, organic gases are flammable and often toxic and thus require special safety measures.

A simple non–flammable quencher gas which shows no aging effects is CO_2. However, the quenching efficiency is significantly lower than for organic gases, limiting the gain before breakdowns appear. In the GEM detectors typical gains are $\sim 10^4$, making CO_2 a well suited, easy to handle quencher gas.

Charge carriers created in a gas volume can recombine, i.e., positive ions and electrons or positive and negative ions. In addition, free electrons can be lost by attachment to an electro–negative atom or molecule. The probability for attachment is essentially zero for noble gases and for hydrogen, while it assumes finite values for other gases. The average time it takes for an electron to become attached depends on the attachment probability and the number of collisions. For oxygen at atmospheric pressure this time is 140 ns, while for CO_2 it is 710 μs. It is therefore essential to limit the oxygen contamination in a detector in order not to lose charge due to attachment.

For the GEM detectors in COMPASS a mixture of Ar and CO_2 with the volume ratio 70/30 is used. The ratio 70/30 was chosen because it provides good discharge protection and less gain change with a changing electrical field than a mixture with a smaller CO_2 content. This relaxes the mechanical tolerances for the detectors. However, the 30% CO_2 content makes it necessary to use rather high operating voltages in order to achieve sufficiently high gains.

3.4 The Gas Electron Multiplier

The **G**as **E**lectron **M**ultiplier (GEM) was introduced in 1996 by Fabio Sauli [3].

3.4.1 The Foils

The GEM is a device for charge amplification in gas–filled volumes and consists of a thin insulating polymer foil which is on both sides coated with thin metal layers. The whole structure is perforated with a large number of circular holes. The holes are arranged in a regular pattern, corresponding to a two–dimensional hexagonal lattice, see figure 3.3. A typical GEM (the so–called standard design) is made from 50 μm thick kapton foil clad on both sides with 5 μm copper. The hole diameter in the copper is 75 μm, the center–to–center distance between holes is 140 μm.

The GEM foils are produced at CERN workshop using photolithographic methods[2]. The pattern of holes is first engraved in the copper on both sides of the foils, then the channels are opened with a kapton–specific solvent using the pattern in the metal as a mask. Since the unprotected polymer is dissolved from both sides, the holes have a double–conical shape with the diameter in the middle of the insulator

[2]Technology developed by A. Gandi and R. de Oliveira, CERN-EST-MT

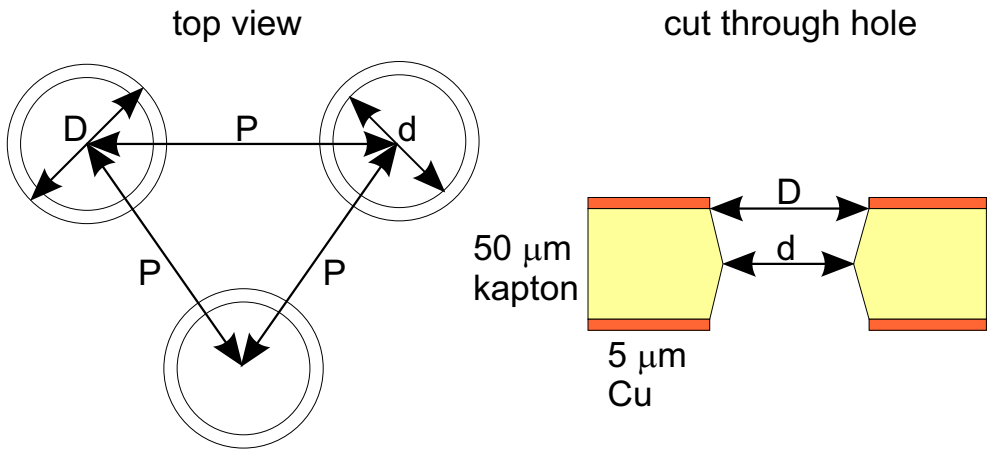

Figure 3.3: Geometric parameters of GEM foil; P = 140 μm, D = 75 μm, d = 65 μm.

slightly smaller ($\sim$ 65 μm for the standard GEM) than at the metal surface. Figure

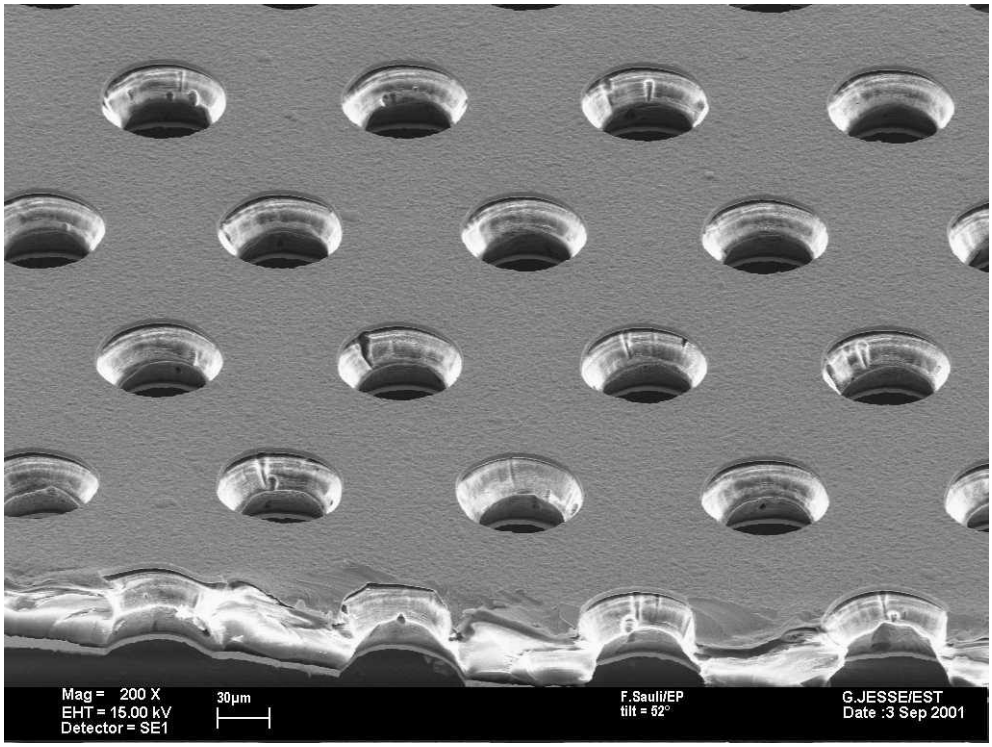

Figure 3.4: Picture of GEM foil taken with an electron microscope.

3.4 shows a picture of a standard GEM foil as they are used for the COMPASS GEM detectors, taken with an electron microscope.

The critical process in the GEM foil production is the alignment of the two masks on the upper and lower metalized side of the foil. Especially for large–sized foils, special care has to be taken. Any misalignment of the two masks will result in

slanted holes, causing lower gain and significant charging up when irradiated.

3.4.2 Operation

Upon the application of a potential difference between the two electrodes of the foil, a high electric field is generated inside the holes. For a voltage difference of ΔU_{GEM} = 200 V, fields of $\sim$ 40 kV/cm are reached, and avalanche multiplication occurs if electrons drift into the hole region [3]. This is ensured by placing the GEM foil in a parallel plate field. Figure 3.5 shows the electric field lines in a GEM hole calculated with MAXWELL, a field simulation program. With a single multiplier foil gains well above 10^3 can be reached.

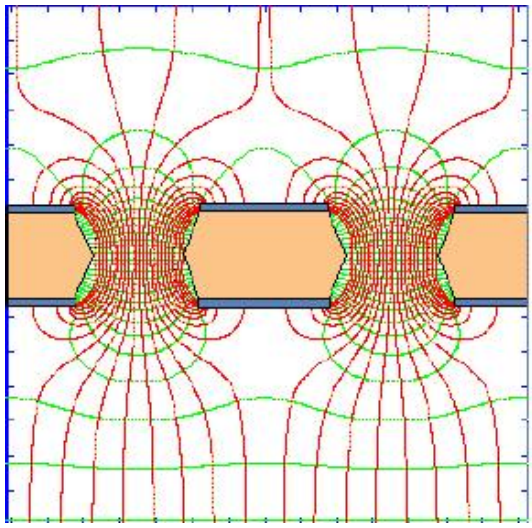

Figure 3.5: Electric field in GEM hole.

It is apparent that most of the field lines from the region above the multiplier enter the holes and exit on the lower side. Therefore, most electrons drifting towards the multiplier will be ensnared by the foil, undergo avalanche multiplication and exit on the lower side, leading to a high electrical transparency. The optical transparency, however, is significantly lower. It is given by $(\pi\sqrt{3}/6)(d/P)^2 = 0.20$.

Some field lines enter the kapton (which becomes polarized in the field, since it is a dielectric). This leads to the deposition of electrons on the surface in the region of the hole where the diameter is smallest. This additional charge causes an increased field in the center of the hole and thus an increase in gain. Due to this phenomenon, called charging up, the gain of a GEM increases by $\sim$ 30% when irradiated. However, the charging up is a fast process (in the order of seconds, depending on the radiation intensity), while the discharging is very slow (in the order of hours) and an equilibrium is quickly reached. The problem of charging up could be reduced considerably by a cylindrical hole geometry. This would cause severe complications in the production, leading to a much smaller production yield, making this option unattractive for mass production.

3.5 Multi–GEM Detectors

Since the GEM is a charge amplification device, it can be used as preamplifier for other detectors. It is possible to use one GEM as preamplifier for another GEM foil. The possibility to cascade several GEM stages to reach high gains is exploited in

multi–GEM detectors and allows the construction of purely GEM–based detectors capable of efficient detection of MIPs.

Purely GEM–based detectors consist of three individual parts: the drift region, the multiplier layers, and the readout plane. Figure 3.6 provides a schematic view of a

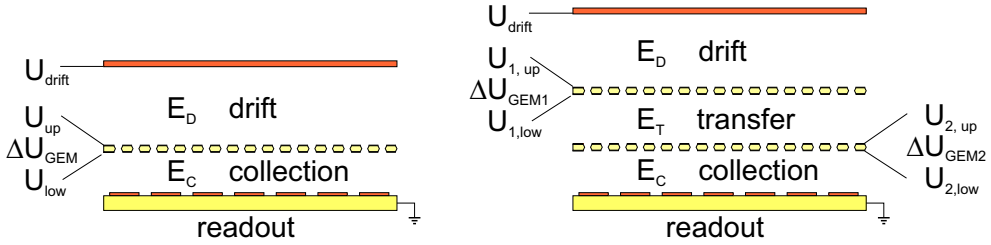

Figure 3.6: Schematics of single and double–GEM detector.

single and a double–GEM detector, including the definition of relevant parameters.

An ionizing particle traversing the detector produces charge along the entire track through the gas volume. However, only the charge produced in the gap between the drift foil and the first multiplier stage contributes significantly to the signal, since for all other primary charge at least one amplification step is missing. For particles which are not absorbed in the detector, the direction in which they traverse the GEM detector is irrelevant.

Due to the drift field E_D the electrons that are produced in the drift gap move towards the topmost multiplier. They undergo avalanche multiplication in the strong electric field caused by the voltage difference ΔU_{GEM1} between the two sides of the foil. In the case of a double–GEM detector, the bigger electron cloud drifts in the transfer field E_T towards the second GEM, where the multiplication process is repeated. After this second GEM foil (in the case of a single–GEM detector after amplification), the electron cloud is ejected into the collection gap and drifts towards the readout plane under the influence of the collection field E_C. Here the charge is collected and read out with electronics. The separation of the readout circuit from the amplification region is one of the big advantages of pure GEM detectors. This limits the risk of damaging the fragile readout strips or the front–end electronics in case of discharges.

The performance of GEM detectors has been studied over a wide range of geometrical parameters [19]. As expected, the proportional gain increases with decreasing hole diameter since the electric field in the hole increases. However, a plateau is reached at diameters around 70μm due to increasing losses of electrons to the bottom electrode, if the hole diameter is reduced below a value close to the GEM thickness. This effect actually relaxes the mechanical tolerances on the GEM foils, since a small decrease in hole diameter for nominal diameters around 70 μm does not change the gain of the multiplier.

The effective gain of the whole detector increases with the collection field, up to the point where the detector enters a parallel plate multiplication regime (in Ar:CO_2 above 8 kV/cm) and avalanche multiplication occurs in the collection gap. This increases the overall gain of the detector, however, it also increases the risk of discharges propagating to the readout electrode, since it means giving up the separation of readout and amplification.

The electric transparency of the GEM depends on the drift field and on the voltage difference across the GEM. For $\Delta U_{GEM} \sim 400$ V, a plateau with high transparency is reached at a drift field around 2 kV/cm for the standard GEM geometry. Field calculations indicate a transparency in the order of 90%, neglecting charging–up of the kapton inside the holes.

A double–GEM geometry allows high gain at moderate voltages across the individual multipliers. The total gain of the structure is to a good approximation the product of the effective gains of the two elements. Moreover, the total gain depends almost exclusively on the sum of both voltages. Therefore voltage sharing between the two stages does not necessarily have to be symmetric. In the case of triple–GEM detectors, charge losses become apparent, so that the total gain is no longer given by the product of the three individual gains. The principle that the amplification can be split asymmetrically between the multipliers still holds.

In the construction of multi–GEM detectors no special care has to be taken to align the holes, because the electron diffusion in the drift between two multiplier stages is around 200 μm, thus largely obliterating the hole structure.

Several applications of the GEM concept have been examined or are still under development. Detectors based on the GEM principle show high rate capability and thus are well suited for applications in high–rate environments. Multi–GEM detectors are not only used as tracking devices, they are also well suited for X–ray imaging applications. Since a GEM foil is an electron multiplication device, it can also be used as a preamplifier stage for other detectors, such as MSGCs[3]. A large number of large–size MSGC+GEM detectors are used in the inner tracker of HERA-B [18]. Another field where GEM detectors show promising results is their use in TPCs[4], where their strong ion feedback suppression capability when operated at low gain is exploited.

3.6 Discharges

A limiting factor in the operation of all micro–pattern gas detectors is the occurrence of discharges at high gain, especially under the influence of heavily ionizing particles

[3] **M**icro–**S**trip **G**as **C**hambers
[4] **T**ime **P**rojection **C**hamber

[20]. The minimization of the discharge probability is reflected in the design of the COMPASS GEM detectors.

The transition of a normal avalanche to a streamer leading to a discharges occurs if the total charge in the avalanche exceeds a value between 10^7 and 10^8 electron–ion pairs (Raether limit), leading to an enhancement of the electric field in the region of the avalanche. This causes the fast growth of secondary avalanches, leading to a breakdown of the gas rigidity.

Since heavily ionizing particles, such as α particles create about 10^4 electron–ion pairs per cm, the Raether limit is reached at gains between 10^3 and 10^4. This is in the same order as the gains necessary to efficiently detect minimum–ionizing particles, leaving only a small, if any, safety margin for detectors that operate in the presence of a heavily ionizing background.

Studies of discharges in single and multiple GEM structures are reviewed in detail in [21]. In most cases (of course depending on the collection field), the discharge remains localized in the multiplier foil (non–propagated discharge), with a very large electron cloud drifting to the readout. However, it can happen that the discharge propagates through the collection gap onto the readout plane (propagated discharge). The probability for a discharge to propagate rises with the strength of the collection field. This type of discharge delivers very high currents to the readout plane, since the full capacitance between the GEM foil and the readout board is discharged. This can lead to the destruction of the front–end electronics.

For non–propagated discharges, the amount of charge transferred to the readout plane and thus to the front–end electronics also depends on the capacitance of the foil. The risk of damages can be significantly reduced by sectorizing the GEM foil on one side, thus reducing the energy available in case of a discharge. The segmentation of the foils also reduces the probability for a discharge to evolve into a fully propagated discharge and to spread out laterally.

For multi–GEM detectors, the discharges take place in the last multiplication step, where the avalanche is the biggest. It has been shown that the probability for a discharge to occur at a certain avalanche size depends on the gain of the GEM, probably caused by a field dependence of the Raether limit. This feature leads to an increase by one order of magnitude of the maximum gain before discharges appear when introducing an additional multiplication step. Figure 3.7 shows the discharge probability as function of gain for single, double, and triple–GEM detectors. These measurements, made with small area experimental detectors and discharges induced by α particles from an ^{241}Am source, show the significant increase in reachable gain caused by the addition of one or two multiplication stages. This result suggests the use of triple–GEM detectors to detect MIPs.

An additional decrease of the discharge probability based on the field dependence of the Raether limit can be reached by an asymmetric gain sharing between the foils in

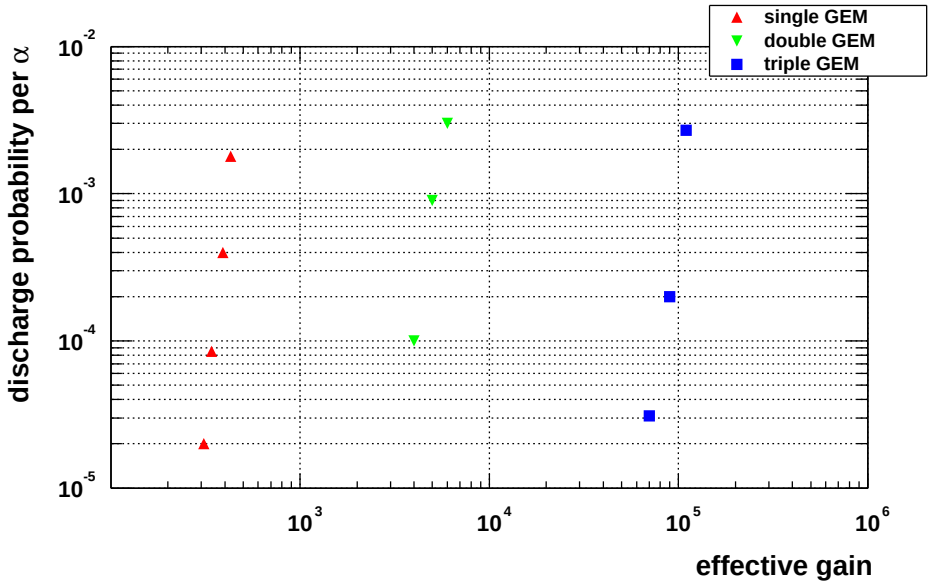

Figure 3.7: Discharge probability as function of gain for different geometries [21].

a multi–GEM detector. Optimal performance for a triple–GEM detector has been reached by a $\sim$ 10% increase of the voltage ΔU_{GEM} across the topmost foil and a $\sim$ 10% decrease of the voltage across the bottom GEM with respect to the one in the middle [21].

The water content of the detector gas has a significant influence on the discharge probability. An increase of the water content from $\sim$ 60 ppm to $\sim$ 80 ppm leads to an increase of the discharge probability by one order of magnitude. It is therefore mandatory to keep the water content in the detector as low as possible.

Chapter 4

GEM Realization for COMPASS

The task of the GEM detectors in the COMPASS experiment is the tracking of charged particles. The special requirements of COMPASS are a good spatial resolution and high rate capability as well as stable operation in the presence of a heavily ionizing background due to nuclear fragments generated by the hadron beam. This chapter describes the technical solutions developed for the COMPASS small area tracker.

4.1 The Geometry

The COMPASS GEM detectors are triple–GEM detectors, comprising three multiplication stages. The triple–GEM design was chosen because COMPASS needs a high gain for the efficient detection of MIPs and a high safety margin for the operation in a heavily ionizing background.

4.1.1 The Foils

The multiplier foils used in the COMPASS detectors are produced from 50 μm thick kapton with 5 μm copper coating on both sides. The holes are of a double conical shape, the diameter in the metal is 75 μm, in the midplane of the foil it is 65 μm. The distance of the holes is 140 μm center to center (see figure 3.3). The foils are 330 $\times$ 330 mm^2 in size. The choice of metal thickness and hole diameter is restricted by availability of the material and by production yield. For thinner metal layers etching becomes increasingly delicate, often leading to defects in the structure.

To reduce the available energy in case of a discharge, the foils are divided into twelve parallel sectors on the top side. Studies have shown that this segmentation does not degrade the discharge behavior as long as no holes are intercepted by a sector boundary. A pierced hole leads to sharp metal edges, where the increased electric

field can cause breakdowns and discharges. In order not to disturb the uniformity of the detector response, the separation between the sectors, an area without holes and metal coating, has to be as small as possible. The nominal value for the width of the sector boundary is 200 μm. For some detectors however the sector boundaries are up to 500 μm in width. Both detectors that were tested in particle beams show this defect, as will be discussed in chapter 6.

In addition to the twelve parallel sectors, there is a central region in the shape of a disc with 50 mm diameter. Separately powered, this sector can be activated independent from the remaining foil (see section 4.2). The voltage to this sector is provided by a thin copper strip in the middle of the extra wider central boundary (600 μm). The central boundary is aligned with the spacer grid (4.1.3) to avoid additional loss of efficiency.

Figure 4.1 shows a photograph of a GEM foil, with the foil placed on a light table and illuminated from the back. This picture shows the segmentation of the foils as

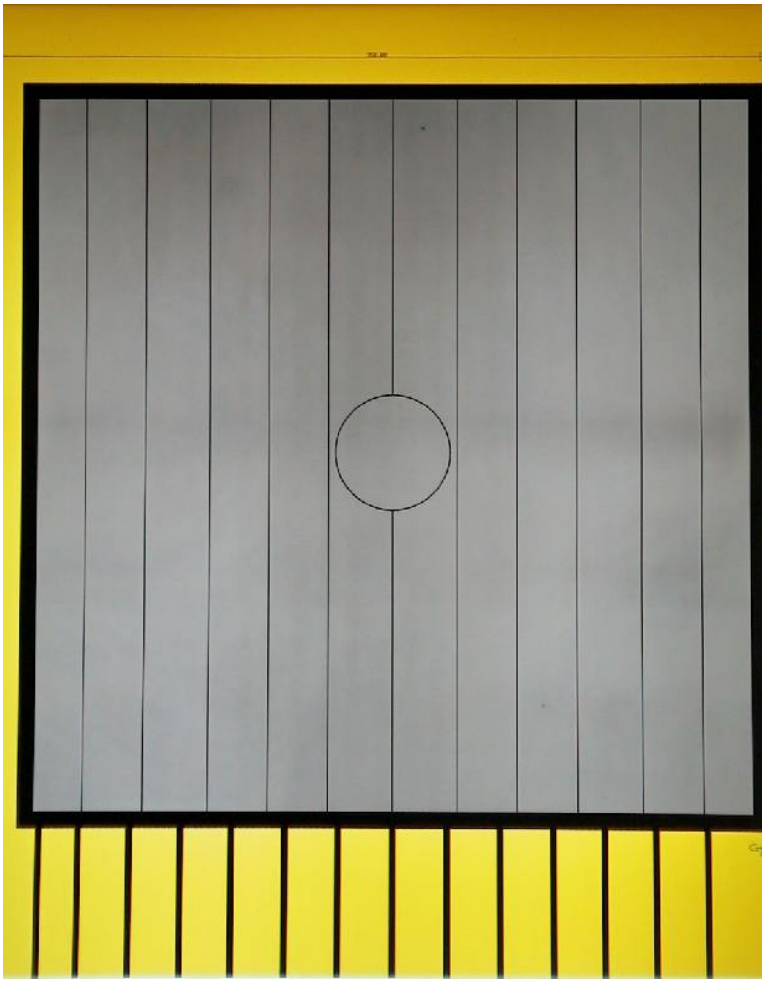

Figure 4.1: Photograph of a GEM foil.

well as the conductor strips at the bottom that are used to connect the individual

sectors to the high voltage network. The connecting strip in the middle of the foil leads to the narrow strip going to the central sector, the six lines left and right of the center provide the connection to the 12 parallel sectors. The strip on the outer left edge connects the back side of the GEM foil, which is not segmented. The 3 mm wide metal border all around the active area prevents glue from diffusing into the holes during the final assembly.

Before a foil is accepted to be installed in a detector it has to undergo several electrical tests. The HV quality of the foils is controlled by applying 550 V to each sector (with the foil in a nitrogen flushed dry box). During the first raising of the voltage it is common that discharges occur, due to residual dirt from the production process. However, after a short training period, each sector has to stand 550 V at a leakage current of less than 5 nA without discharges.

4.1.2 The Readout Plane

The charge from the three multiplier stages is collected on a two–dimensional readout plane, consisting of a PCB[1] with two layers of 768 perpendicular copper strips at a pitch of 400 μm. The two layers are separated by 50 μm thick kapton ridges. The production is similar to the method used for the GEM foils: 50 μm thick kapton foil coated on both sides with 5 μm of copper is used. After etching of the strip pattern into the metal layers on both sides of the foil, the foil is glued onto a 120 μm thick fiberglass support, and the bare kapton between the topmost strips (covering the lower strips from above) is chemically removed, partially exposing the lower strips. Figure 4.2 shows a schematic drawing of the two dimensional readout structure. The

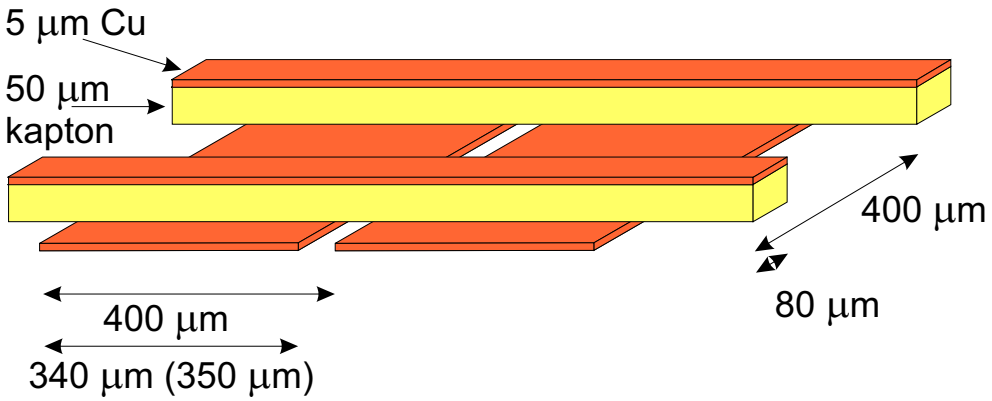

Figure 4.2: Schematic of the readout structure, the width of the lower strips has been reduced from 350 μm to 340 μm to avoid short circuits between strips.

strip width, 80 μm for the upper layer and 350 μm for the lower layer, was chosen to get equal charge sharing between both readout coordinates.

[1] **P**rinted **C**ircuit **B**oard

To facilitate wire bonding to the readout strips, the pads at the end of the strips outside the gas volume have to be coated with a thin gold layer. For the first detectors the whole readout structure was chemically gold plated, leading to several short–circuits between adjacent readout strips in the lower layer. This problem was solved by restricting the gold treatment to the bond pads and by decreasing the strip width on the lower coordinate to 340 μm.

The noise of the front–end electronics depends strongly on the capacitance of the readout structure. Crucial is the capacitance of one single strip versus the other readout coordinate. With the permitivity $\epsilon_r = 3.9$ of kapton, this capacitance is 15 pF.

4.1.3 The full Detector

A cut through a COMPASS triple–GEM detector is shown in Figure 4.3. The whole

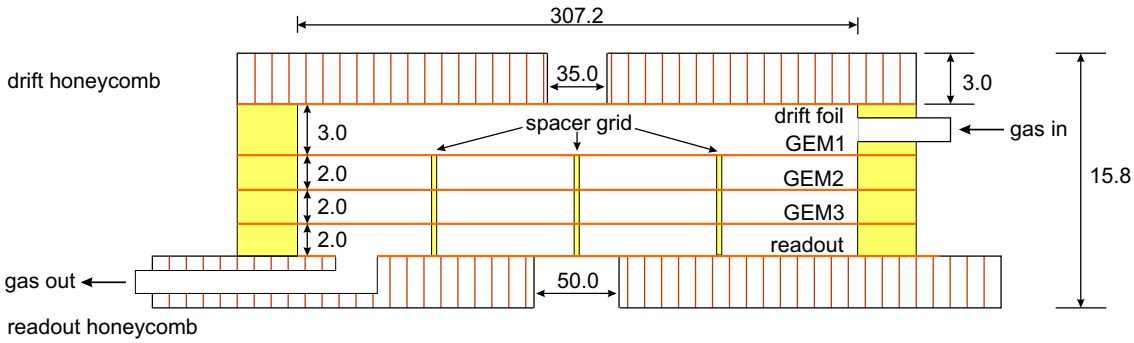

Figure 4.3: Cut through a COMPASS triple–GEM, all lengths in millimeters.

detector structure is sandwiched between two honeycomb support plates that give the structural stability. The honeycomb plates are 330 × 330 mm^2 and 500 × 500 mm^2 in size, made out of a sandwich of two fiberglass foils (120 μm Stesalit) and a 3 mm cellular spacer. To reduce material in the central beam region, the honeycomb plates have circular holes in the center, 35 mm in diameter for the top plate, 50 mm for the bottom plate. The hole in the top plate is smaller to avoid deformation of the drift foil glued to the structure.

The space of 3 mm between the drift foil and the first GEM foil is defined by a 3 mm thick fiberglass frame. The frames between the GEM foils and between the last foil and the readout plane are 2 mm thick. In addition, since these foils do not have any support structure to withstand the electrostatic forces between the foils without bending, the frames contain a spacer grid dividing the whole detector into 16 cells and the central sector, with $\sim$ 300 μm wide strips. The spacer grid introduces a local loss of efficiency that will be discussed in chapter 6. To avoid discharges at residual spikes or broken glass fibers on the grid, the structure is coated with a thin layer of two–component polyurethane.

The readout PCB is glued onto the lower honeycomb plate. This plate is covered with a 10 μm thick aluminum foil for noise screening. In addition, precision holes for the fixation of readout electronics are drilled into the support plate.

Figure 4.4 shows an exploded view of a COMPASS triple–GEM detector. It illustrates the design of the detectors and the orientation of the different components. The topmost GEM foil is rotated 90° with respect to the other two foils to realize sufficient spatial separation of the high voltage supply chains. The supply for the topmost foil is most critical, since here the voltage difference to ground is highest.

The assembly of the detectors proceeds from the top down. First, the drift foil is glued to the top honeycomb plate, then the drift frame is mounted. After this, the pre–stretched GEM foils and the spacer grids are mounted one after the other. The last step is the closing of the detector with the bottom honeycomb, onto which the readout board was glued.

After the closing of the chamber, the edges are sealed with a thin layer of silicone resin (Dow Corning R4-3117) which covers the high voltage leads and prevents external discharges. Also eventual gas leaks are prevented with the HV sealant. The finished chamber is tested for gas leaks and afterwards released for electrical connections and for final testing.

The finished GEM detector is 15.8 mm thick and has a material budget of 0.71 % radiation length without electronics and high voltage distribution (see section 4.1.4). In a later stage, the front–end electronics is mounted onto the larger honeycomb and bonded to the readout pads. Figure 4.5 shows the top view of a COMPASS GEM detector with high voltage distribution and readout electronics.

Before the detectors are installed in the spectrometer, the upper side is covered with aluminized mylar foil supported on a 50 μm thick kapton frame over the HV distribution and the readout electronics to protect the electronics and as a noise shielding.

4.1.4 Material Budget

An important parameter that describes the influence of the GEM detector on the performance of the spectrometer is the material budget, expressed in radiation lengths[2]. For GEM detectors, the material budget is position dependent, even in the active area, due to features such as the holes in the foils, the location of the spacer grid, or the strip structure of the readout plane. As a reference value the material budget averaged over the active area of the detector is given. It is calculated from the individual contributions of the detector components, weighted with the fraction

[2]One radiation length is the mean distance over which a high energy electron loses all but 1/e of its energy by bremsstrahlung [11]

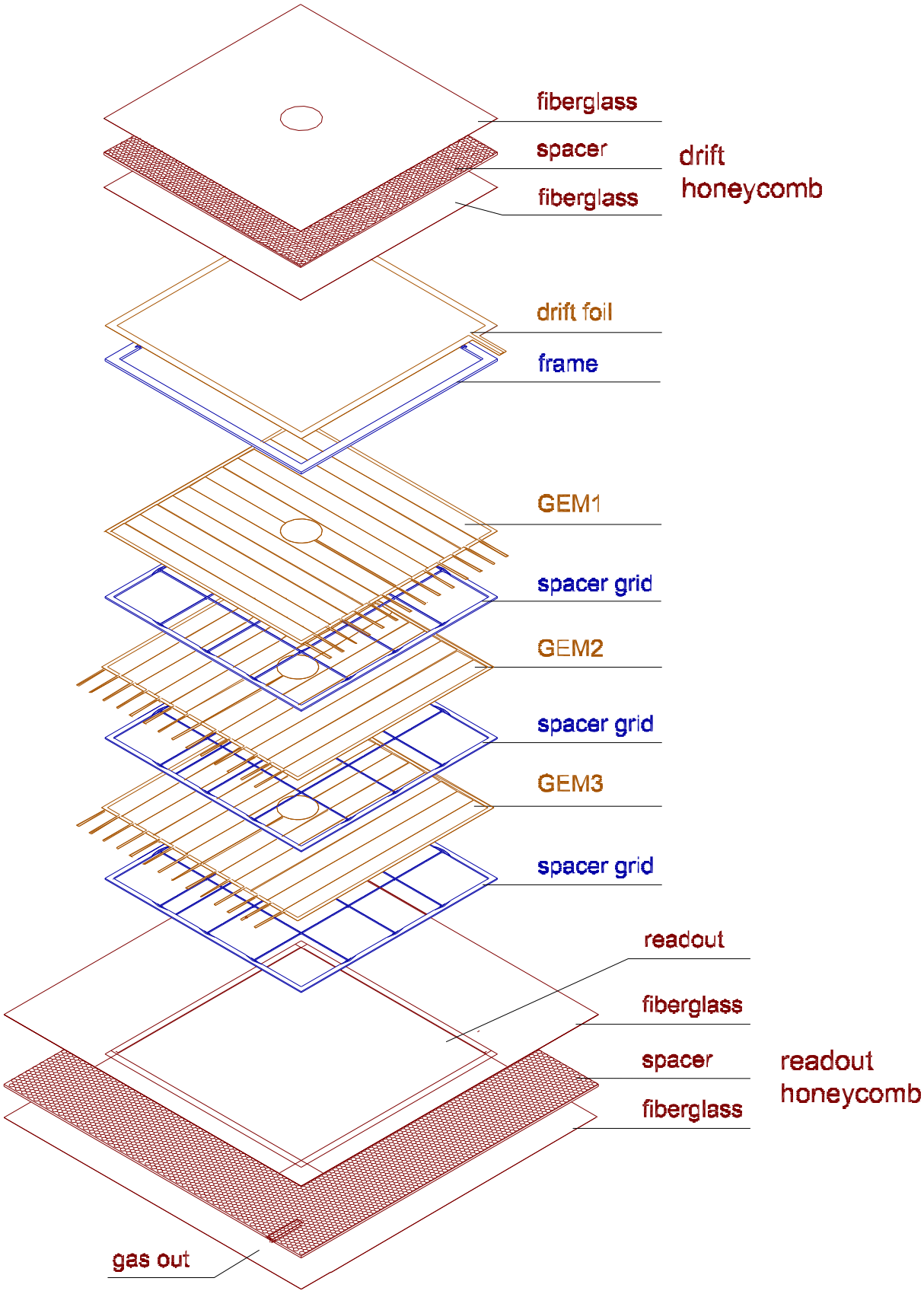

Figure 4.4: Exploded view of GEM detector.

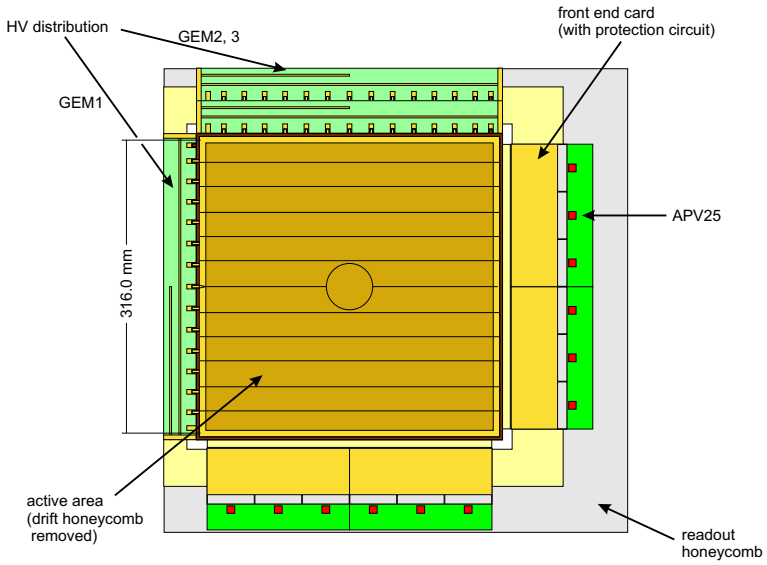

Figure 4.5: Top view of a COMPASS GEM detector.

of the area they cover. Values for the radiation length of the different materials are taken from [11].

Table 4.1 gives the contributions of each detector component. The material budget of a complete COMPASS GEM detector is $7.1 \times 10^{-3}\ X_0$.

In the central region (diameter 35 mm), where the beam passes through the detector, the material budged is reduced by holes in the honeycomb support plates. The reduced budget in the central region is $4.2 \times 10^{-3}\ X_0$.

4.2 High Voltage

A COMPASS triple–GEM detector has 8 different high voltage potentials: The drift voltage, the 6 voltages for the top and bottom of the three GEM foils and the separate voltage for the central sector of the last GEM foil. A resistor network is used to generate the necessary voltages from one single HV channel. The schematic of this network is shown in figure 4.6. Given the individual resistors, the ratio of the voltages is fixed. Under beam load, the voltages can change slightly due to the current caused by the electron avalanches.

At nominal operation conditions typical currents through the resistor network are in the order of 750 μA, leading to a drift field of 2.5 kV/cm and transfer and collection fields of 3.75 kV/cm. The GEM voltages range from $\sim$ 350 V across the last GEM foil to $\sim$ 500 V across the first GEM foil.

The loading resistors to the different sectors of the GEM foils are chosen in such a way that, when a discharge occurs, the voltage of the upper side drops significantly,

component	coverage	material	X_0 [mm]	X	total X
drift foil	1	5 μm Cu	14.3	0.35	
	1	50 μm kapton	286	0.17	0.52
GEM foil	0.74	2 $\times$ 5 μm Cu	14.3	0.52	
	0.77	50 μm kapton	286	0.13	0.65
spacer grid	0.006	2 mm G10	194	0.06	0.06
readout board	0.2	5 μm Cu (80 μm strips)	14.3	0.07	
	0.2	50 μm kapton	286	0.03	
	0.875	5 μm Cu (350 μm strips)	14.3	0.31	
	1	120 μm G10	194	0.62	1.03
honeycomb	1	3 mm Nomex	13125	0.23	
	2×1	120 μm fiberglass (G10)	194	1.24	1.47
shielding	1	10 μm Al	89	0.11	0.11
total glue	1	60 μm glue	200	0.30	0.30
gas filling	1 $\times$ 0.981	9.18 mm Ar:CO_2 (70/30)	131570	0.07	0.07
total detector					7.10

Table 4.1: Material Budget, X is the thickness in units of $10^{-3}\,X_0$. Multiple components are GEM foils and spacer grids (3 each) and honeycombs (2). The central region of 35 mm diameter for passage of the beam has a thickness of $4.16 \times 10^{-3}\,X_0$.

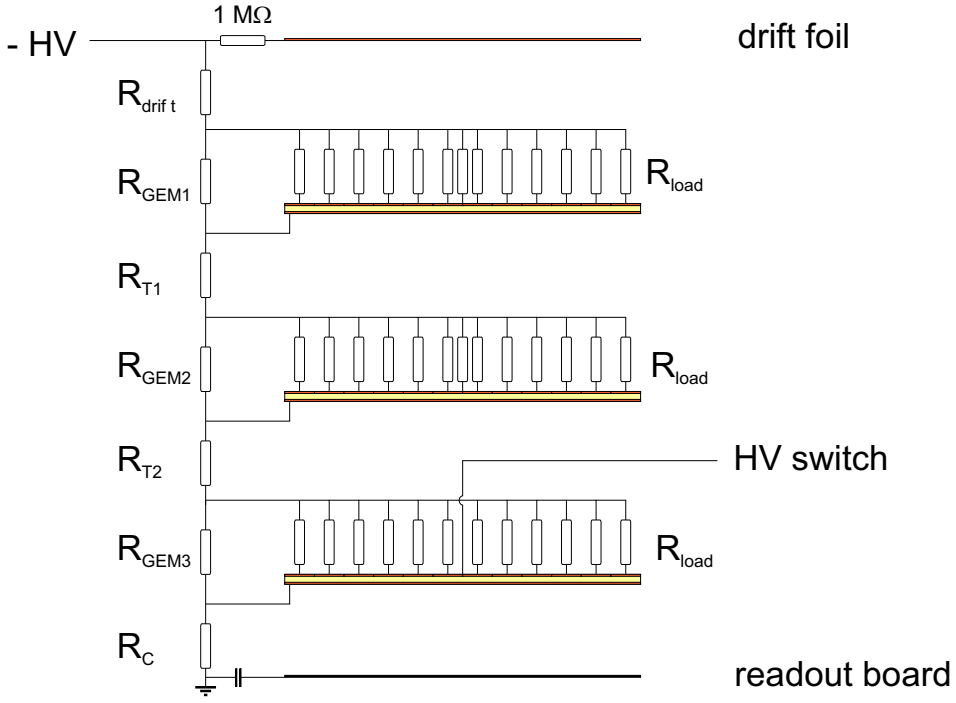

Figure 4.6: Resistor network.

while the voltage of the lower side of the foil remains almost unchanged. In addition, in the case of a permanent short–circuit in one sector, the detector still has to be able to operate, with only a small change in gain. To guarantee that, the loading resistors have to be significantly larger than the resistors in the voltage divider chain. However, it is also desirable to have a high rate capability, and since the ions from the avalanche multiplication are neutralized on the foils, a high particle rate causes a high current through the loading resistors, and thus a voltage drop, that restricts the size of the resistors. On the other hand, the resistors in the divider chain cannot be decreased at will to avoid this limitation, since the maximum current available from the used HV modules is 1 mA.

The resistors for the different voltages across the three GEM foils reflect the asymmetric gain sharing chosen to minimize the discharge probability.

The nominal values for the resistors in the high voltage distribution scheme are given in table 4.2.

Resistor	Value [MΩ]
R_{drift}	1.0
R_{GEM1}	0.675
R_{T1}	1.0
R_{GEM2}	0.55
R_{T2}	1.0
R_{GEM3}	0.460
R_C	1.0
R_{load}	10.0

Table 4.2: Nominal resistor values.

The resistors are mounted on HV distribution boards manufactured from 200 μm thick fiberglass. After the soldering of the resistors the boards are cleaned and coated with an insulating HV sealant. Each board is tested to stand 5 kV without discharges, and each single resistor value is measured to facilitate the calculation of the individual voltages and currents in the detector. The contacts of the individual sectors are soldered to the HV boards and then covered with high voltage sealant.

The central sector of the lowest GEM foil (next to the readout plane) is powered independently through a high voltage switch that permits to decrease the potential of the central sector by $\sim$ 200 V, thus reducing the gain by more than an order of magnitude. This results in complete insensitivity of the central region (see chapter 6) and allows the operation of the detector in high–intensity beams.

The HV switch itself is a resistor network with a high voltage relais. The voltage in the "on" condition can be adjusted so that the gain in the center matches the gain in the straight regions. The central sector can be switched on remotely, without

having to lower the high voltage on the detector. For low intensity alignment runs of the COMPASS spectrometer the center will be activated.

4.3 Electronics

For the GEM detectors a system capable of reading 1536 channels per detector at high trigger rates is necessary. The readout system can be divided into several different components, starting from the front–end chip which is mounted directly on the detector and ending at the DAQ system which is located in the control room of the experiment. In this section mainly the front–end electronics on the detectors is covered. For a detailed treatment of the full readout chain see [22].

4.3.1 The APV25 Front–End Chip

The central part of the readout system on the detectors themselves is the APV25–S0 front–end chip [23, 24]. The chip was developed for the silicon tracker of the future CMS experiment at the Large Hadron Collider presently under construction at CERN, but it is also suited as a readout for the GEM detectors. It is an ASIC[3] fabricated in 0.25 μm technology, optimized for low noise and power consumption and high radiation tolerance. It has a size of 8.2×8.0 mm^2, with an active area of approximately 7.2×6.5 mm^2.

The APV chip has 128 input channels, each consisting of a 50 ns CR–RC type shaping amplifier, a pipeline with 192 memory elements and a pulse shape processing stage that provides a silicon–specific deconvolution operation not applicable to the GEM signals. The APV runs at a frequency of 40 MHz, sampling the signal after the amplifier stage of each channel.

The pipeline consists of 192 switched capacitor elements per channel. From these, 160 are used to buffer the data on the chip, allowing a maximum delay of 4 μs between the event and the arrival of the trigger at the chip. Every 25 ns, the amplitude behind the preamplifier stage is sampled and stored in the pipeline, which is operated as a circular buffer. This means that after 4 μs (corresponding to 160 samples), the first entry is overwritten. The remaining 32 memory cells of the pipeline are used to store events flagged for readout by a trigger until the time they can be read out. The time between the event and the trigger is called the latency. It defines how much time the chip goes back in the pipeline to find the correct signal to be read out. By using different latency with unchanging trigger conditions, the time dependence of the signal can be investigated. Figure 4.7 shows the result of a so–called latency scan. It was done with an APV chip not connected to a detector by injecting a δ - shaped charge pulse [25]. The signal rises in less than 50 ns, while

[3] **A**pplication **S**pecific **I**ntegrated **C**ircuit

the decay time is more than 250 ns. The response is represented by the product of two exponential functions,

$$P = A\,(1 - e^{-\frac{t-t_0}{\tau_1}})\,e^{-\frac{t-t_0}{\tau_2}}, \tag{4.1}$$

where A describes the amplitude, t_0 the begin of the rise, τ_1 the time parameter of the rising edge, and τ_2 the time parameter of the falling edge of the signal. The parameters for the plot in figure 4.7 are $A = 157$, $t_0 = -44$ ns, $\tau_1 = 22$ ns, and $\tau_2 = 100$ ns.

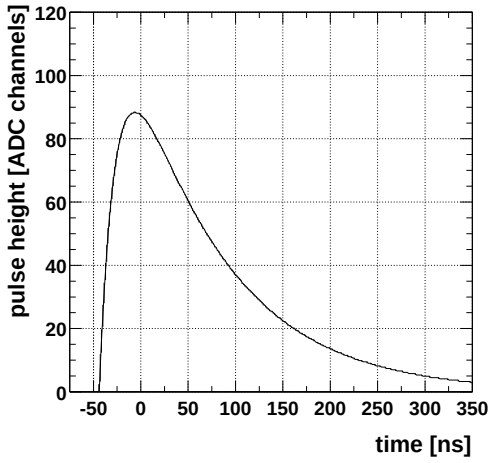

Figure 4.7: Response of APV chip to δ - shaped charge pulse.

With input from a GEM detector, the rise of the signal will be slower since it is influenced by the time distribution of the arrival of the charge from the detector as well as by the shaping time of the amplifier. The distribution of arrival times is caused by the different drift times for the charge released at different positions in the drift gap. The spread of the distribution can be calculated from the width of the drift gap divided by the drift velocity of the electrons, which is also in the order of 50 ns. The long decay time of the signal is dominated by the amplifier response. The characteristics of the signal allows a determination of the signal time with respect to the trigger time by comparing the amplitudes in consecutive samples. It is clear that for a good time resolution, the rising edge of the signal has to be examined, as will be discussed later (see section 6.4.2).

The chip can be operated in three different modes. The first mode is the peak mode, where only the contents of one memory cell per channel is read out. This memory cell should be the one containing the peak of the signal. In principle, this is enough to reconstruct hits as long as the beam intensity is very low.

At higher intensity, pile up might occur, meaning that signals from different events with different timing are in the detector at the same time. To select the signals with the right timing, the time evolution of the signals has to be studied. This is possible with the multi mode, where the content of three consecutive memory cells, corresponding to the evolution of the signal amplitude over a range of 75 ns (sampled at 0 ns, 25 ns, and 50 ns) is read out. This allows the determination of the time of the passage of the particle that caused the signal. Signals with the proper timing should be on the rising edge (see figure 4.7). This mode is used for the readout of the GEM detectors. A more thorough discussion of signal timing can be found in chapter 6.

The third mode is the deconvolution mode, which internally processes three consecutive samples to determine the timing of a signal and sends the information out as one single frame. This mode allows the transmission of information characterizing the signal in compact form. However, this mode is optimized for the characteristics of silicon detectors and cannot be used for the GEM detectors.

If the APV receives a trigger, it begins sending out data to the ADC with a differential signal. This means that the signal is sent over two signal lines, one line carrys the inverted signal of the other, the total signal is given by the difference of the two individual signals. This mode of signal transmission reduces the noise on the signal considerably, since a sizeable fraction of external noise is picked up by both lines, and thus cancels in the difference. The APV is able to send out data at two different frequencies, 20 MHz and 40 MHz. For the readout of the COMPASS detectors presently 20 MHz is used.

The three consecutive samples that are read out (defined by the latency) are sent out serially. Before transmitting amplitude values, the chip sends a header which contains error information and the number of the memory cell that is written out. After the header, the amplitudes of the different channels are transmitted. However, they are not sent out in linear order, but undergo three multiplexing steps and thus geometrically adjacent channels are not next to each other. A raw APV signal with all three samples is shown in figure 4.8. Here, a noise spectrum was recorded, so no signals are seen in the output. A true signal from a particle appears as negative spikes on the flat noise spectrum, as shown in figure 4.9. Here, a cluster with three strips above threshold (strips 49, 50 and 51) is shown. The increase of the amplitude from sample 0 to sample 2 shows the time evolution of the signal. The baseline of the APV chip can be adjusted according to the signal polarity (negative in the case of the GEM detectors, since electrons are collected), to allow a large dynamic range. The baseline differs slightly from channel to channel and has to be determined after each change of parameters. The baseline values of the individual channels are called pedestals. To recover the true signal, the pedestals have to be subtracted from the APV output.

After the end of the data of the third sample, the chip returns to its normal output. During the time periods when the APV is not triggered, it sends out a synchronization tick mark every 1.75 μs. This is used to enable the readout electronics to synchronize with the chip and to stay synchronized even if there are no triggers over an extended period.

The different settings of the chip (i.e. latency, baseline) can be programmed via a two–wire serial interface conforming to the Philips I2C standard.

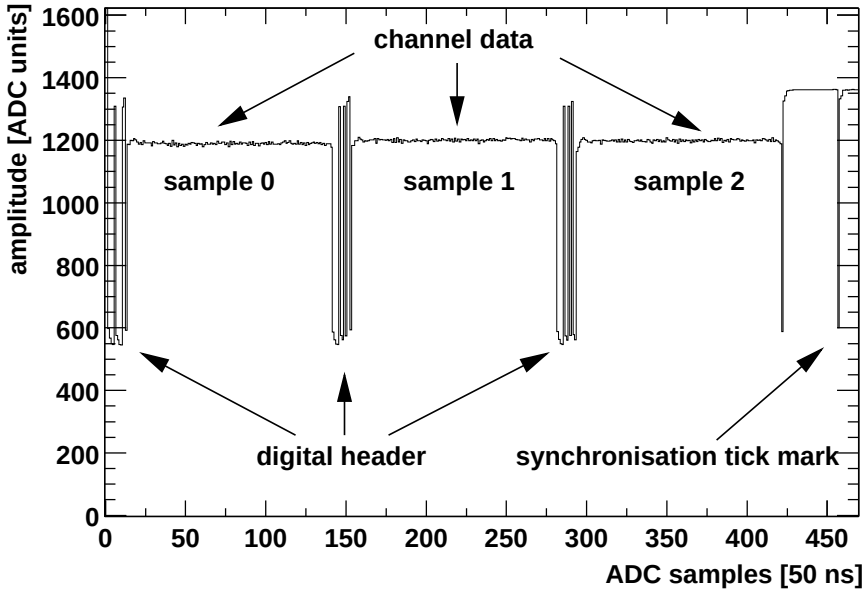

Figure 4.8: Raw APV output signal, noise spectrum.

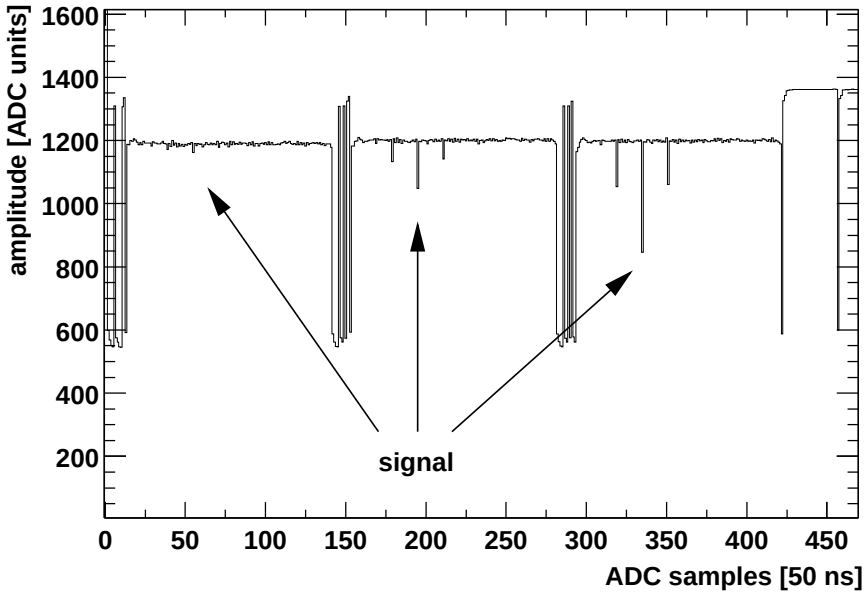

Figure 4.9: Raw APV output, with GEM signal.

4.3.2 Front–End Cards

The possibility of discharges in the detector induced by heavily ionizing tracks makes a protection of the front–end chip necessary. Since the chip was designed for silicon

detectors, it has no protection circuit against very high pulses on the input, which might upset or even damage the APV. This protection has to be provided by an external circuit.

This protection circuit and the pitch adapter, together with power and ground connection and connectors for the readout and the program interface of the APV chip are provided by the front–end cards, on which the chips are mounted. These cards have bond pads with 400 μm pitch and are bonded to the readout plane using standard wire bonding techniques with 17 μm wire.

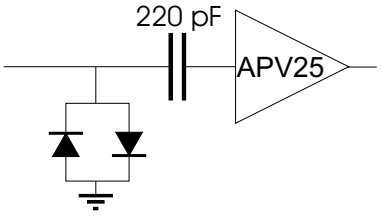

Figure 4.10: Protection circuit.

Since the purpose of the protection circuit is to protect the input of the front–end chip from pulses with high amplitudes, it is made up out of two anti–parallel diodes between the signal input and ground. With this configuration, any signal which rises to more than $\pm$ 0.7 V will be grounded, thus protecting the chips from high pulses with arbitrary polarity. Figure 4.10 shows a schematic drawing of the protection circuit.

Since a diode has a small but not negligible leakage current and since this current is slightly different for each diode, a circuit consisting only of two diodes may cause a constant current on the input of the APV chip, because its input is not on ground potential. This can lead to a saturation of one or more input channels and even to a malfunction of the entire chip due to an increased power consumption. The problem can be avoided by an AC coupling of the signal input by a serial capacitor. One drawback, however, is that the additional capacitance reduces the signal amplitude for a given amount of charge on the readout strip. The capacitance chosen is about a factor of 10 larger than the strip capacitance, thus causing a reduction of the amplitude of approximately 10%. In addition, the protection circuit introduces noise due to the diodes which act as a capacitance to ground. In order to be fully efficient for the detection of MIPs, the gain has to be increased to compensate the signal loss in the protection circuit and to account for the higher noise level on the readout. Both effects together require an increase of the gain necessary for full efficiency from $\sim$ 5000 to $\sim$ 8000.

The bond pads on the APV25 S0 chip have a pitch of 44 μm. This pitch has to be adapted to the 400 μm pitch of the GEM detector readout. For this, the fan out pattern of the pitch adapter is evaporated with aluminum onto a 200 μm thick glass plate. This technique is chosen because it allows the production of structures with very fine pitch. For comparison, the typical pitch feasible with standard PCB technology is around 100 μm. In order to have good production yields and relaxed tolerances during assembly, one pitch adapter per chip is used.

The boards themselves are fabricated in a standard multilayer PCB technology and

assembled with SMD[4] components. One front–end board hosts three APV chips, so that each detector has two front–end boards per coordinate. For the protection circuit, a package with a double diode (BAV99) is used, while the capacitors are integrated in capacitor arrays with 4 capacitors each. After the production and the assembly the boards are tested electrically by a specialized company to make sure that all diodes are working and that all electrical connections are functional.

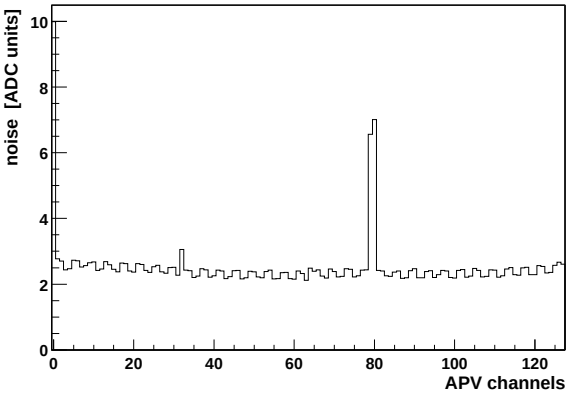

Figure 4.11: Noise spectrum of APV on front–end card, faulty bonds on channel 79, 80.

The pitch adapters and the chips are glued to the PCB. On the boards themselves three bonding steps are necessary: the output of the chip to the PCB, the input of the chip to the pitch adapter and the pitch adapter to the protection circuit. Between these bonding steps, the boards are tested by taking noise spectra of the APVs in order to recognize faulty chips or damaged bonds. Figure 4.11 shows a noise spectrum for a chip with two touching bonds on the chip readout. The faulty bonds are clearly visible by their significantly higher noise. Defects such as these are repaired before the front–end cards are mounted to the detectors. The very high noise in channel 0 and the elevated noise level in channel 32 are caused by cross talk in the long cables from the APV to the ADC employed in the laboratory setup. These channels are affected since they are the first two to be sent out after the error bit, due to the multiplexer stage in the chip. The online tests during the bonding and assembly procedure help to identify problems early enough to make repairs or even exchange components if necessary.

After the fully assembled front–end cards are tested, they are mounted to the detector and bonded to the readout. The total number of bonds per channel is three (see above): two on the front end card and one from the front–end card to the detector readout. This leads to a total number of 4608 bonds per detector, without counting the temporary bonding of test boards for quality control (see chapter 5).

4.3.3 The Readout Chain

The output of the APV25 chip is transmitted to a specialized ADC for digitization. This is done via the so–called repeater cards which act as amplifiers for the outgoing signal and which supply the power and the programming interface for the front–end cards and the APV chips.

The ADC module is a sampling ADC able to run at the two possible APV frequen-

[4] **S**urface **M**ounted **D**evice

cies of 20 MHz and 40 MHz. The ADC recognizes the APV header information and generates a new header for the data it sends out, containing error and event information. One ADC module is able to process the output of 12 chips (one full detector). In addition, the ADC provides the I2C interface used to program the front–end chips. The ADC module offers two modes of operation. In the latch–all mode, the amplitudes of all channels in all three samples are sent out. This limits the possible trigger rate to approximately 1 kHz due to the large amount of data that has to be transmitted through the readout chain. To reach higher trigger rates, the amount of data has to be reduced considerably. This is done in the sparse mode. In this mode of operation, the ADC sends out only data for channels which are above a certain threshold. To do this, the ADC has to subtract the pedestals for each individual channel and correct for common mode noise[5]. The pedestal values can be transmitted to the ADC via software. The sparse mode permits high trigger rates, depending on the occupancy[6] of the detector. However, in sparse mode data may be irrevocably lost since only a small fraction of the information is read out and recorded for analysis. The ADC module was developed within the COMPASS collaboration at TUM [26]. The ADC data format adheres to the standardized COMPASS data format [27].

Via an optical fiber (*HotLink*), the ADC is connected to a control unit called *GeSiCA*[7]. This unit is able to read and control up to 4 ADC modules and sends its data via optical link (*S-Link*) to the DAQ computers. The *GeSiCA* is installed in front–end VME computers and provides a programming interface for the APV chips.

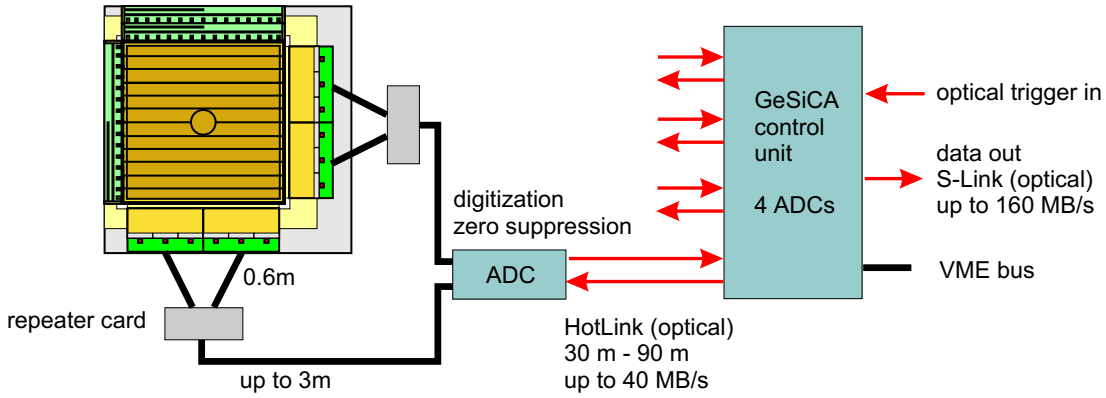

Figure 4.12: GEM detector readout chain.

A sketch of the full readout chain from the detector front–end to the data acquisition system in the experiment is shown in figure 4.12.

[5] collective change of all pedestals due to pickup noise
[6] number of strips above threshold
[7] **Ge**m and **Si**licon **C**ontrol and **A**cquisition

4.4 Discharge Studies

The effect of discharges in triple–GEM detectors was studied with a prototype of the COMPASS design. The main difference between this detector and the final version was a pitch of 200 μm at the bonding pads (the pitch of the readout strips was 400 μm as in the final design), making this detector unsuited for the standard readout electronics.

The discharges were induced by the α emitter ^{220}Rn (half–life 54.5 s, α energy 6.4 MeV). The detector gas was seeded with radon by letting the gas flow pass through a thorium oxide mesh which releases radon from the thorium decay chain.

The drift volume of the detector is uniformly exposed to the ionizing radiation. Since the direction of the emitted α particle is completely random, the energy loss distribution has a broad spectrum with an average around 400 keV. This energy loss is several orders of magnitude bigger than the energy loss of a minimum–ionizing particle ($\sim$ 800 eV) and can lead to discharges by exceeding the Raether limit.

For the study with α particles between 16 and 768 strips where grouped together and read out with an oscilloscope (set to 1 MΩ) over a 1 MΩ resistor. Thus, the effective discharging resistor was 500 kΩ. If a discharge occurs, the induced signal can be seen on all readout strips. Figure 4.13 shows a discharge with all 768 strips of one readout coordinate connected together.

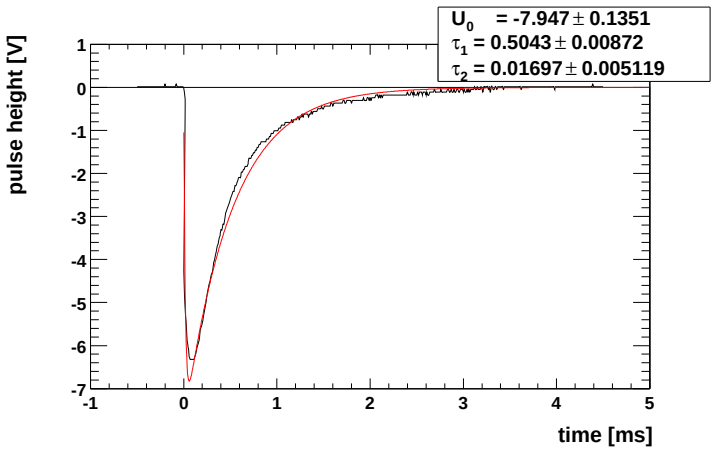

Figure 4.13: Discharge induced by α particle.

The shape of the pulse can be described by the difference of two exponential functions,

$$U(t) = U_0(e^{-\frac{t}{\tau_1}} - e^{-\frac{t}{\tau_2}}) \tag{4.2}$$

since a discharge corresponds to the fast charging up of the readout strips, followed by the slower discharging through the terminating resistor. The pulse shown in the

figure corresponds to about 4.5×10^{10} electrons, while the charge from a MIP at a nominal gain of 8000 is only 2.5×10^5. This figure clearly shows the potential danger to the readout electronics.

To be able to safely operate the detectors in the COMPASS experiment over a period of several years, a protection circuit for the front–end electronics is necessary to exclude the possibility of damage due to discharges.

Chapter 5

Quality Control and Laboratory Tests

The completed GEM detectors undergo a series of tests in the laboratory to determine their quality and their individual properties.

5.1 HV Validation and first Signals

After the high voltage distribution network is connected to the GEM foils the detector is ready for HV validation and signal tests. For proper shaping of the signal, simple readout electronics consisting of an ORTEC 147 preamplifier and an ORTEC 450 research amplifier is used [28]. The standard readout electronics via the APV chips is not suited for tests with X–rays, since it requires an external trigger.

To keep edge effects low, 32 adjacent readout strips are grouped together and read out. Tests have shown that for a grouping into 16 strips, edge effects have a considerable influence on the spectrum, while an increase above 32 strips does not yield additional improvement. This grouping is done by mounting a test board to the detector and bonding the detector readout pads to the bond pads on the test board. These test boards are thin PCBs with 24 groups of 32 strips, every group being terminated with 1 MΩ to ground.

5.1.1 External Discharges

As a first test the full detector is going to be put on high voltage. To minimize normal signals and to exclude internal discharges, the chamber is flushed with the quencher gas CO_2.

The voltage is raised carefully to an average level, while external discharges, i.e., sparks in the high voltage distribution system outside the detector gas volume, are

monitored on an oscilloscope via the preamplifier and amplifier. External discharges are visible on the readout strips due to the charge induced on the GEM foils and on the readout plane. It is quite usual that some discharges occur in the first minutes with high voltage on, due to dust and metal splinters, but their frequency should decrease quickly, since these impurities are burned away. Spots prone to external discharges are found by flushing the HV distribution system with argon, which increases the discharge probability and the signal amplitude. Defects in the high voltage sealing can be repaired by additional coating. Discharges are monitored for approximately one hour. If no discharges occur, the high voltage distribution network is validated.

5.1.2 Internal Discharges and Signals

To see signals from an X–ray source and to test the detector for internal discharges the counting gas Ar:CO_2 (70/30) is used. After flushing the detector for several hours the voltage is raised carefully, while monitoring the detector current with the ampmeter of the HV power supply. Whenever discharges occur, the raising of the voltage is suspended for some time. After this training procedure the detector can be brought to nominal voltage.

With an ^{55}Fe source (5.9 keV X–rays) first signals are seen. By fine–tuning the ancillary HV the gain of the central region is adjusted to match the gain in the straight sections.

5.2 Gain Maps and Calibration

Having passed the external and internal HV validation tests, the GEM detector is installed in an X–ray test setup. The radiation source is a Cu X–ray generator which emits the characteristic copper lines and continuous bremsstrahlung. The generator is operated at a voltage of 15 kV, and the X–ray beam is collimated to a beam spot of ~ 4 mm^2. At the level of GEM resolution for X–rays, it is sufficient to treat the spectrum as consisting of two components, the 8.0 keV K_α and the 8.9 keV (K_β) line, which have an intensity ratio of $I(K_\beta)/I(K_\alpha) = 0.135$ [31]. The X–ray tube can be moved in the horizontal and in the vertical direction, so that a scan over the full detector area can be performed. For optimal resolution, the X–ray beam has to be centered on a 32 strip sub–group. This is ensured by monitoring the spectrum while moving the generator. Within a sub–group, a plateau region with high amplitude and good resolution is observed. For the data taking, the X–ray beam is directed to the center of such a region.

The readout of the detector is again done with the ORTEC amplifier system, using the test boards bonded to the readout plane. However, to allow a quantitative

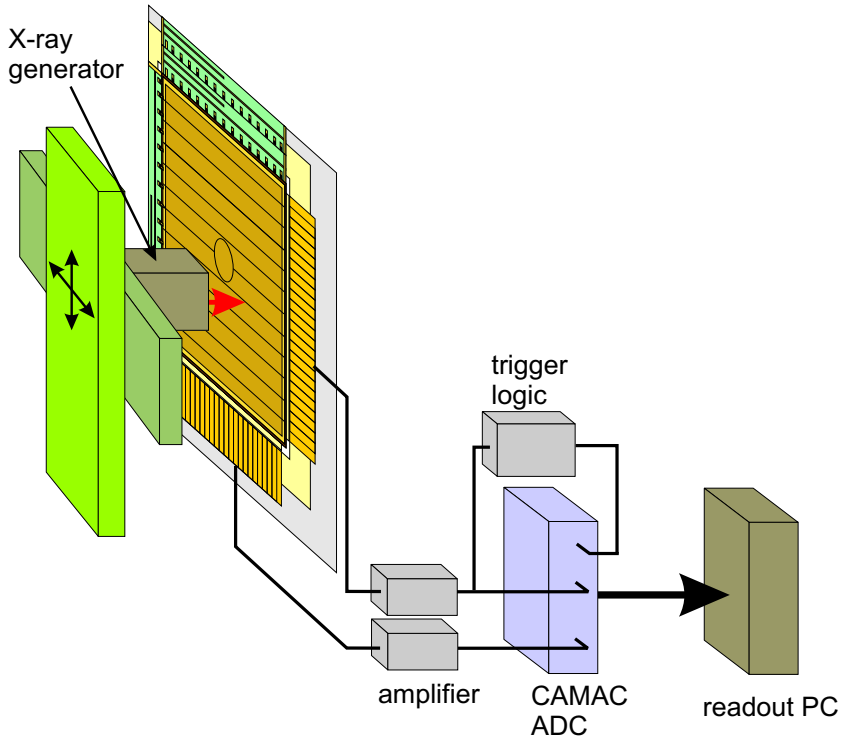

Figure 5.1: X–ray test setup.

analysis of the data, the data acquisition is realized with a CAMAC ADC read out via PC. For this purpose, special software adapted to read the CAMAC crate is used [29].

Figure 5.1 shows a schematic sketch of the test setup in the laboratory, including the data acquisition system. Both coordinates are read out simultaneously. The trigger for the CAMAC ADC is supplied by a discriminator that cuts low amplitude noise without influencing the spectrum.

For the offline analysis, CAOFF (**CA**MAC **OFF**line Analysis), a program written in C++ based on the use of ROOT libraries (see [30]) was developed. CAOFF automatically applies a fit to the spectrum to obtain pulse height and corresponding energy resolution. The fitting function is adapted to the two–component structure of the X–ray spectrum observed in the GEM detectors, composed of the full–energy peak of the unresolved Cu K lines and of the corresponding argon escape peak, where the 2.9 keV Ar X–ray leaves the detection volume. Since the drift gap is very thin, most photons escape and the ratio of the argon escape peak to the full–energy peak is given by the fluorescence yield of argon which is $\sim 15\%$.

In order to obtain start values for the final fit the spectrum is first fitted without taking into account that the Cu X–ray spectrum is composed of two lines. The spectrum function is a sum of two Gaussians, the first describing the full energy

peak, the second corresponding to the argon escape peak:

$$f(x,p) = p0 \times e^{-\frac{1}{2}\left(\frac{x-p1}{p2}\right)^2} + p3 \times e^{-\frac{1}{2}\left(\frac{x-p4}{p5}\right)^2} \tag{5.1}$$

Here, x is the ADC channel and $p0$ to $p5$ are the fit parameters that have to be determined. The background is represented by a third order polynomial so that the full fitting function is the sum of equation 5.1 and a third order polynomial, with a total of 10 free parameters.

To account for the two lines in the X–ray spectrum, a sum of two spectrum functions of the type defined in equation 5.1 is used, with a fixed intensity ratio of 0.135 and a ratio of the photo peak positions of 1.1, given by the intensity and energy ratios of the Cu K_α and K_β lines. The result for the two Cu lines is shown in figure 5.2. The 8.0 keV K_α photo peak and the corresponding argon escape peak dominate the

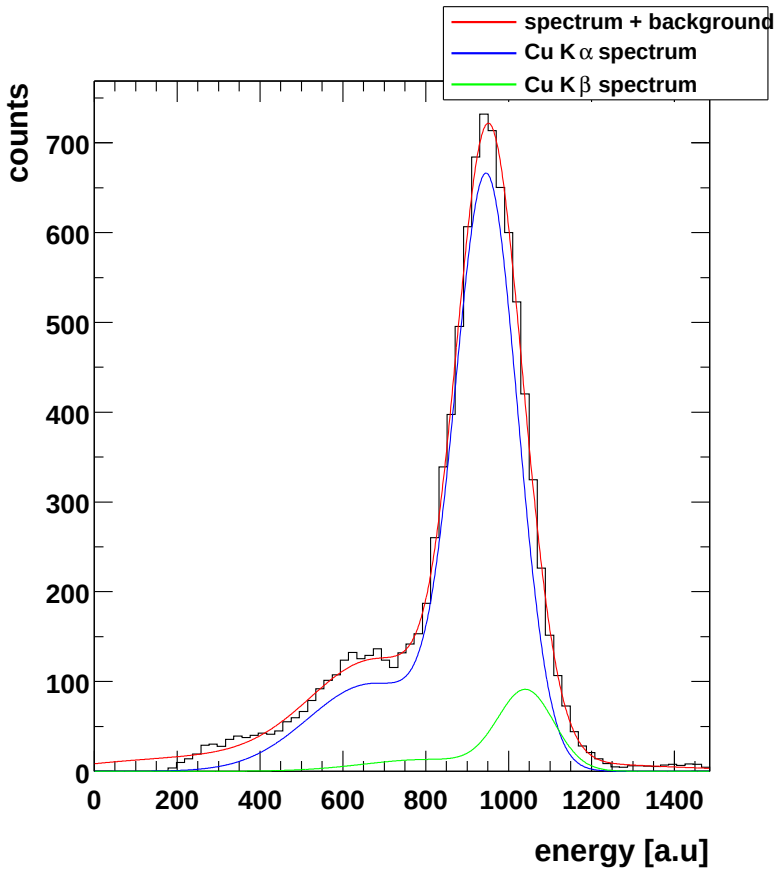

Figure 5.2: X–ray spectrum taken with a COMPASS triple–GEM detector. Energy zero is at channel 100, the Cu K_α full–energy peak is at channel 947, its energy resolution is $\Delta E/E = 0.19$.

spectrum. This shows that Cu X–rays are a good choice for the measurements, since their energy is high enough to penetrate into the drift region of the detector and the

K_β intensity is sufficiently small to treat the spectrum as a single–line spectrum in first approximation.

The energy resolution, defined as the ratio of the full width at half maximum over the mean of the photo peak, is of the order of 20%. The energy resolution is an indicator for the quality of the GEM foils, since good energy resolution requires good homogeneity of the foils over the irradiated area ($\sim$ 4 mm^2). Defects of the individual holes, such as cracks in the kapton, missing copper, or overhanging copper cladding change the amplification properties and result in a loss of resolution since several holes contribute to the signal.

With the setup shown in figure 5.1 X–ray spectra are taken for 16 different locations over the detector, always in the center of the cells defined by the spacer grid. To get clean spectra, a thin Cu absorber (5 μm) is placed in the X–ray beam to filter the bremsstrahlung spectrum. Its effect is the transformation of higher–energy X–rays from the spectrum (maximum energy 15 keV) into the characteristic Cu lines, and the absorption of the lower energy components. The drift foil of the GEM detector, 5 μm Cu on 50 μm kapton, as well as the fiberglass sheets of the drift honeycomb, also act as such a filter. Since the gain increases by about 30% due to charging up of the GEM foils when the detector is first irradiated, data taking is started only a few minutes after positioning of the X–ray generator. From the spread of amplitudes measured and from the quality of the spectra, maps of relative gain and energy resolution can be generated.

Figure 5.3 shows the gain map on the 80 μm coordinate of one of the detectors tested in the T11 test beam (TGEM10, see chapter 6). The units on the z axis

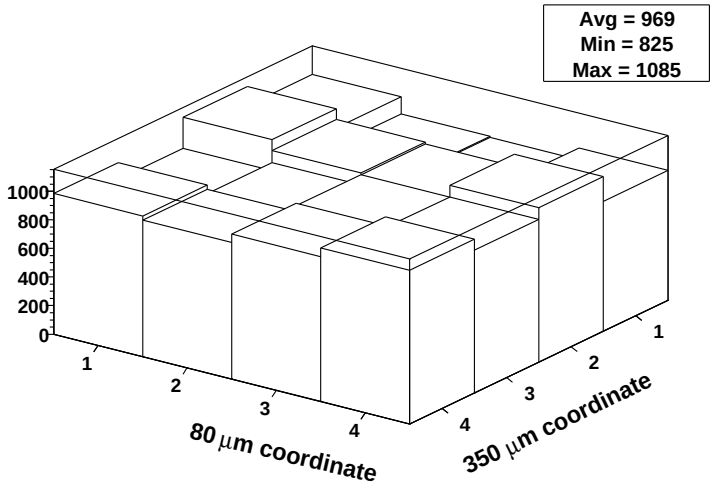

Figure 5.3: Map of effective gain, point (1,1) is given by the spectrum in figure 5.2.

are ADC channels (peak amplitude expressed in the arbitrary units of figure 5.2), while the coordinates on the x and y axis correspond to a four by four grid of the

detector surface. The map shows rather moderate deviations of about ± 15% from the average gain.

This also can be seen from the histogram of all 16 measured gains, normalized to the average gain, shown in figure 5.4. An unusually large spread of these values would indicate defects in the GEM foils, such as misalignment of the production masks. These problems would also cause a deterioration of the energy resolution.

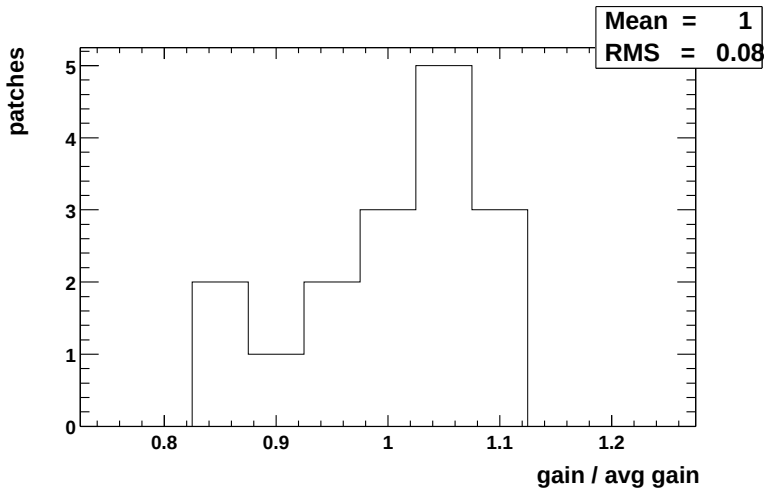

Figure 5.4: Distribution of gains for the 16 detector patches (see figure 5.3), normalized to the average value.

After the mapping of the relative gain an absolute calibration of the effective gain is needed. This is done by measuring the rate of the incident X–rays and the current on the readout plane. The current is calculated from the voltage drop over the 1 MΩ resistors on the test boards.

The total number of electrons produced by the absorption of an X–ray in the drift gas can be calculated from equation 3.4, if one takes the number of entries in the argon escape peak into account. For a photon energy of 8.9 keV, the average number of primary electron–ion pairs is 324, for an energy of 8.0 keV it is 289. Taking the relative intensity of the K_α and K_β lines into account as well as the Ar fluorescence yield, the average number of electron ion pairs produced per Cu X–ray detected in the drift region is $\nu = 293$.

The effective gain of the detector in a given point is calculated according to

$$gain = \frac{I_{total}}{\nu e f} \,. \tag{5.2}$$

Here, I_{total} is the sum of the currents on both readout coordinates, ν is the average number of electron ion pairs created by the absorption of the photon, e is the elementary charge, and f is the rate of interactions in the detector, measured by

counting the triggers for the CAMAC readout. Typical rates are in the order of 10 kHz.

The effective gain for each detector is measured in the regions with the highest and the lowest gain found in the gain map. The lowest gain defines the minimum voltage necessary for efficient operation of the detector, the maximum gain sets a limit on the voltage before discharges appear. Figure 5.5 shows the minimum and the maximum gain of TGEM10 (see chapter 6) as a function of the drift voltage, the total voltage over the detector. The gain increases exponentially with the voltage,

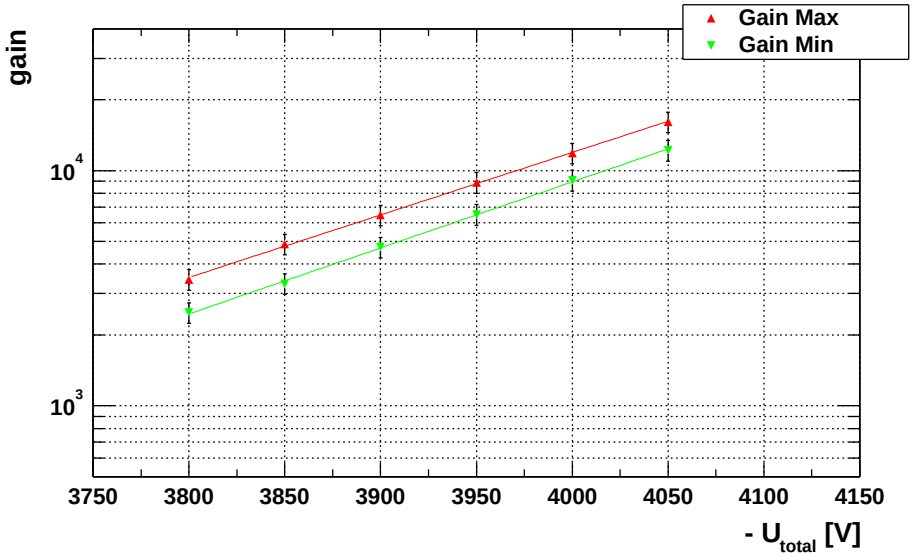

Figure 5.5: Minimum and maximum gain of a triple–GEM detector.

showing that the detector operates in a regime where the Townsend coefficient (see 3.2.3) is linearly dependent on the electric field.

The voltage needed to reach the nominal gain of ~ 8000 differs by about 50 V from detector to detector due to variations in the resistor values and in the geometric parameters of the GEM foils. The gain depends strongly on external parameters, especially on the air pressure. The fact that these parameters are not controlled during the measurements limits the time available for a complete scan to a few hours. After the calibration measurements are finished the test boards are removed and the detector is ready for mounting and bonding of the readout electronics.

5.3 Functionality Test of the Readout Electronics

Before the installation into the COMPASS spectrometer, the GEM detectors are tested with the final readout electronics. The test itself consists of two steps. The

first step is the recording of a noise spectrum of the full detector, using random triggers. This permits to find defects such as imperfect grounding or broken bonds. The second step is the test with a β source while the detector is being operated at a moderate gain ($\sim$ 5000). The aim is to record MIP electrons.

As was already mentioned, this cannot be done with X–ray irradiation, since the readout electronics does not posses any self–triggering capability. The test has to be done with particles that lose energy in the detector, but traverse it and can be detected behind the detector to generate the trigger. The β emitter ^{90}Sr with its short–lived daughter ^{90}Y is a straightforward option. The trigger is generated with two scintillators in coincidence. Figure 5.6 shows the setup used.

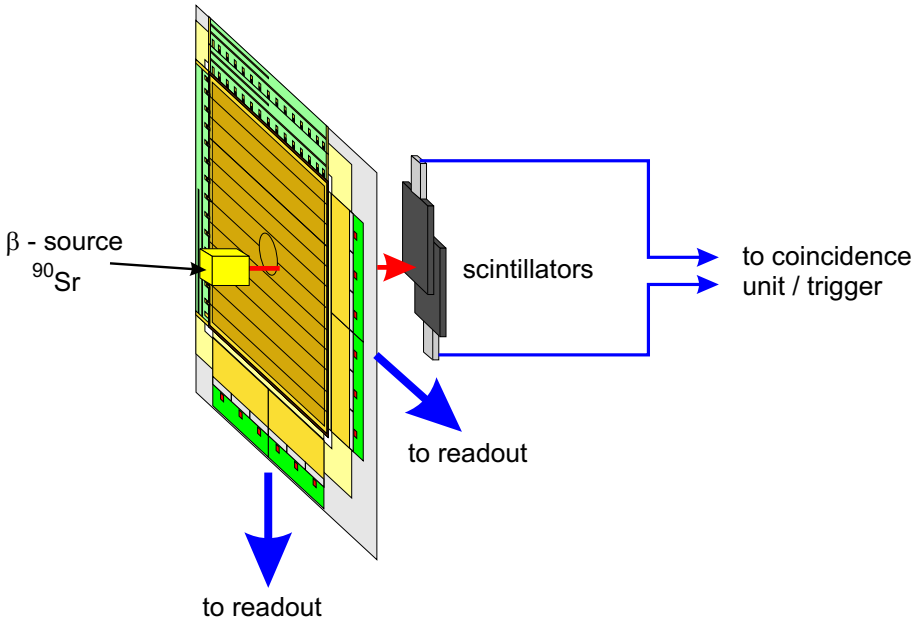

Figure 5.6: β test setup.

The ^{90}Sr source ($\sim$ 10 MBq) emits electrons with two different end point energies, 0.546 MeV from the ^{90}Sr decay and 2.283 MeV from the decay of the daughter ^{90}Y. If a detector in a fully assembled GEM station is tested, the triggering scintillators can only be placed behind the second GEM detector, which means that the electrons have to traverse both GEM detectors and both scintillators. This reduces the trigger rate considerably, since only the high–energy electrons pass through the full setup. Typical trigger rates are of the order of 10 Hz, which is enough for a rough test of the whole system.

After this test the detector is ready for the installation in the COMPASS spectrometer.

Chapter 6

Beam Tests

In April 2001, two GEM detectors were tested in a low intensity secondary beam of positive pions and protons. The goals of this beam time were the verification of the readout electronics with the complete COMPASS readout chain, the test of a silicon micro–strip detector and the study of the properties of two GEM detectors. The measurements were carried out in the T11 experimental area in the East Hall of the PS[1] accelerator at CERN.

6.1 The T11 Beam

The secondary particles for the T11 beam are produced by protons with a momentum of 24 GeV/c hitting a pencil–like production target made out of aluminum (diameter 5 mm, length 250 mm). The intensity of the incident protons is 2×10^{11} per pulse ($\sim$ 1 s). Since the beam line transports particles of a given pre–selected rigidity, the secondary beam is composed of different particle species. In our case these are protons, positive pions, and kaons produced in the target as well as pair–produced positrons originating from the 2γ decay of neutral pions. Table 6.1 shows the particle intensities per pulse, as delivered at the reference focus of T11, 28 m downstream from the production target. Due to their larger mass and shorter lifetime, the contribution of kaons is down by two orders of magnitude compared to the pion intensity.

The momentum of the particles was set to the maximum momentum of 3.6 GeV/c to keep multiple scattering effects as small as possible. The accuracy of the momentum of the particles at T11 is 1%. The divergence of the beam is 20 mrad in the vertical plane and 6 mrad in the horizontal plane, defined by the acceptance of the T11 beam line.

[1] Proton Synchrotron

Particle	Intensity/spill
p	3×10^5
π^+	3.5×10^5
K^+	$\sim 3 \times 10^3$
e^+	$\sim 5 \times 10^3$

Table 6.1: Secondary particle intensities at T11, normalized to 2×10^{11} protons incident on the production target. The momentum is p = 3.6 GeV/c, the acceptance window is $\Delta p/p = \pm 1\%$.

6.2 The Setup

In the T11 test beam, two GEM detectors and one silicon detector have been installed. The positions of these tracking detectors and of the scintillators used for the trigger system are shown in figure 6.1. The two GEM detectors TGEM10 and

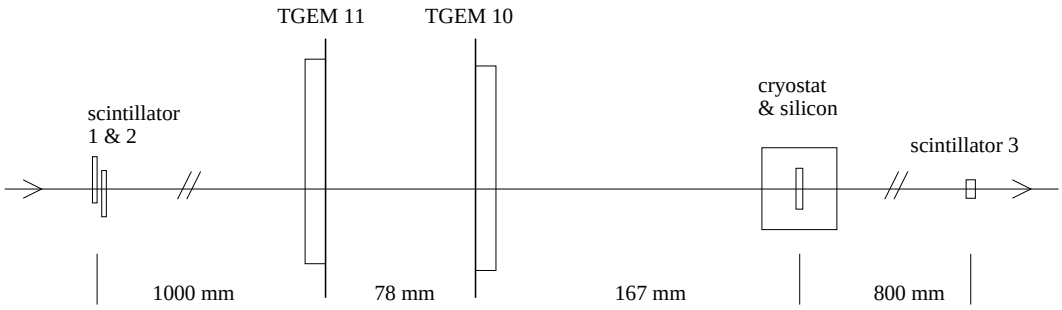

Figure 6.1: Geometry of the T11 setup. The focus point is approximately 25 cm upstream of the first trigger scintillators.

TGEM11 both have readout boards with 350 μm wide lower strips, and they both have sector boundaries up to 500 μm wide. The silicon detector was installed inside a stainless steel cryostat with thin entrance and exit windows, but was operated at ambient temperature.

TGEM10 and TGEM11 were mounted back to back on a common support frame, with a distance of 78 mm between the readout honeycombs. TGEM10 was rotated by 90 degrees with respect to TGEM11. TGEM10 read the horizontal coordinate (x) with the 350 μm strips and the vertical coordinate (y) with the 80 μm strips, vice versa for TGEM11. This is illustrated in figure 7.1.

The silicon micro–strip detector is a double sided silicon detector, which means that on each side of the wafer one projection is read out. The strips have an angle of 2.5° with respect to the wafer edges. The wafer itself can be rotated ±5° inside the cryostat. The silicon detector was only available for the last days of the beam test and permitted tracking studies.

6.3 Data Taking

6.3.1 First–Level Trigger

The trigger system for the T11 beam test consists of three scintillators. The two large scintillators upstream of the tracking detectors have an overlapping area of about 10×10 cm^2, the small scintillator downstream of the detectors covers an area of 5×2 cm^2. The scintillators are read out with photo diodes.

The trigger signal is generated by a four–fold majority coincidence unit. The trigger system can be operated in two modes. In the first mode, only the two large upstream scintillators are included in the coincidence. This allows scans of large areas. In the second mode, all three scintillators are requested. This mode is used for high statistics studies of small regions of the GEMs and for tracking runs together with the silicon micro–strip detector. The pulses of the scintillators were set in such a way that the trigger time was defined by scintillator 2 in the first mode and by the small finger scintillator 3 in the second mode.

Since the GEMs are read out in latch–all mode (see section 4.3.3), the large event size limits the sustainable trigger rate to ~ 1 kHz. To ensure stable running conditions for the readout system, a dead time of ~ 1 ms is implemented in the trigger.

6.3.2 Data Acquisition and Decoding

For the data acquisition in the T11 area, the full COMPASS readout chain was used (see figure 4.12). Each GEM detector was read out with one ADC module, both ADCs being controlled by one common GeSiCA module. The silicon detector was equipped with two ADC modules, since it has a total of 18 APV chips, and another GeSiCA.

The two GeSiCA modules transmit their data via optical link to a computer acting as readout buffer and event builder. As DAQ software the ALICE[2] acquisition system DATE [32] is used. For each valid trigger DATE writes the raw data taken from the detector front–ends to file. This data contains the strip amplitudes as well as several headers allowing GeSiCA identification, ADC identification, front–end chip identification as well as spill and event number assignment.

From this data stream the individual strip amplitudes for all detectors in the DAQ system have to be extracted and correctly assigned to the individual detector projections. For this task a program called `gemMonitor` is used [33]. This program, written in C++ using DATE and ROOT libraries, decodes the DATE data stream and writes the relevant information into a ROOT file.

[2]Heavy ion experiment at the LHC at CERN

Since the ADCs used in the test beam were not equipped with zero suppression routines, the full detector data was sent to the DAQ for each event. To reduce the size of the ROOT files `gemMonitor` subtracts the pedestals, corrects for common mode noise, and only writes the amplitudes and strip numbers i (between 0 and 767) of maximal 25 strips per projection to file. These 25 strips are the 5 strips with the highest amplitudes and the two strips on each side of that strip. For the modest particle intensities in the test beam the hit multiplicity is low and no data is lost in this operation.

For each detector decoded by `gemMonitor` a ROOT tree is created containing the strip amplitudes and noise and position information. Through this structure the stored information is easily accessible. The ROOT tree is used in the subsequent data analysis.

6.4 Online Analysis

This section gives an overview of the analysis methods that permit an online control of the detectors. Permanent monitoring of the detector performance ensures that possible problems during the data taking are detected as early as possible.

6.4.1 Cluster Finding

The search for clusters is done for each projection individually. The first step of the cluster finding algorithm is a peak search. To find peaks in the strip amplitudes of the detectors, one looks for a change of slope of the amplitude as a function of strip number i. A local maximum, characterized by a rising slope to the left and a falling slope to the right is classified as a peak.

The next step is to decide which (if any) of the peaks are valid clusters by applying amplitude cuts. By looking for local minima between peaks, the algorithm also takes the possibility of overlapping clusters into account.

To get the cluster amplitude, the amplitudes A_i of all strips that are more than $3\sigma_i$ (individual strip noise) above zero are summed up. If the total cluster amplitude is more than $5\sigma_c$ (RMS cluster noise σ_c) above zero , the cluster is accepted as a valid cluster. The RMS cluster noise is defined as

$$\sigma_c = \sqrt{\frac{\sum\limits_i \sigma_i^2}{n-1}}\,, \tag{6.1}$$

where n is the number of strips in the cluster.

The cluster center is calculated by the center of gravity method, taking the amplitude above threshold $A_i - 3\sigma_i$ for each strip in the cluster,

$$center = \frac{\sum_i (A_i - 3\sigma_i)\, i}{\sum_i (A_i - 3\sigma_i)}. \tag{6.2}$$

The sum over i runs over all strips above threshold.

6.4.2 Adjustment of the Trigger Latency and Signal Timing

An important issue is the timing of the signals in the detector. First, the right settings for the latencies of the detectors (common for all chips on a given detector) have to be determined. If, with increasing beam intensity, multiple hits become probable, it is necessary to decide which of the signals in the detector has the correct timing with respect to the trigger and thus belongs to the event of interest.

For the determination of the signal timing, the three consecutive samples read out with the APV chip have to be analyzed (see 4.3.1). They are 25 ns apart and have the amplitudes sample0, sample1, and sample2. These amplitudes contain information about the time evolution of the signal and thus permit the determination of the signal timing with respect to the trigger. Since the pulse height varies considerably from event to event, ratios of the samples are used [34].

For a good time resolution, sample2 should be located close to the maximum of the signal. Since the signal rises in less than 100 ns the case $0 <$ sample0 $<$ sample1 $<$ sample2 gives precise timing information, whereas the reverse case (due to the large falling time of $\sim$ 300 ns) is not useful for the extraction of the signal timing.

This can be seen from the latency scan shown in figure 6.2.

For the determination of the signal timing and for the verification of the latency settings, timing plots as shown in figure 6.3 are used. In all four plots in this figure, the ratio of sample1 and sample2 is plotted versus the ratio of sample0 and sample2. For correct timing the ratio sample1/sample2 should be larger than the ratio sample0/sample2, and both should be smaller than 1.

The second frame in this figure ("in time") shows the distribution of amplitude ratios for the correct latency settings. The four plots together illustrate how these ratios change with decreasing latency (signal sampled later). The bulk of the entries moves from the lower left region to the upper right region.

Even when the latency setting is correct, some entries are outside the expected region. This is caused by particles not correlated to the trigger. Events which are located in the upper right region, where sample0/sample2 is larger than sample1/sample2, and where both ratios are significantly larger than unity are sampled

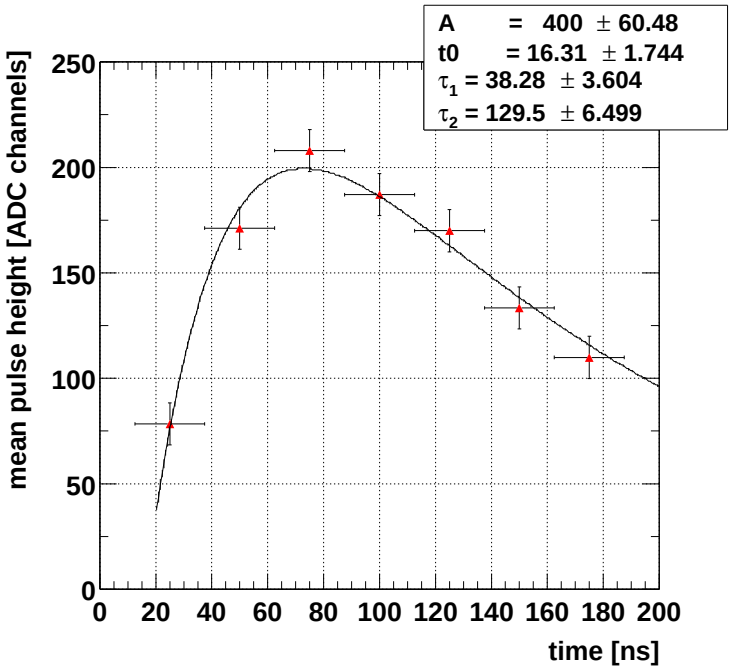

Figure 6.2: Latency scan at T11, the times in the inset are given in nanoseconds. For comparison: the response of the APV25 without detector is shown in figure 4.7.

on their falling edge. They represent particles which passed the detector before the triggering particle.

The location of a given event on this timing plot reflects the instant of the passage of the particle with respect to the readout cycle of the chip, which in turn is started by the trigger. However, the chip samples with its 40 MHz clock while the triggers are asynchronous. This introduces a 25 ns time jitter and causes the smeared timing plot.

6.4.3 Cluster Analysis

From the clusters obtained with the cluster finding algorithm, several properties of the detectors can be extracted. All values that are shown here have been obtained while taking data with the detector at nominal conditions (gain ~ 8000).

Figure 6.4 shows the distribution of the cluster charge. It follows a Landau distribution typical for minimum–ionizing particles and reflects the energy loss of the particles in the drift gap of the GEM detectors. Here, the fact that the beam consisted basically of two particle species, pions and protons, which have a different energy loss at the given momentum, has to be taken into account. For a discussion of the effects and for a comparison with data from a muon beam see section 8.2.2.

The cluster size is plotted in figure 6.5. The size of the clusters on the lower (350

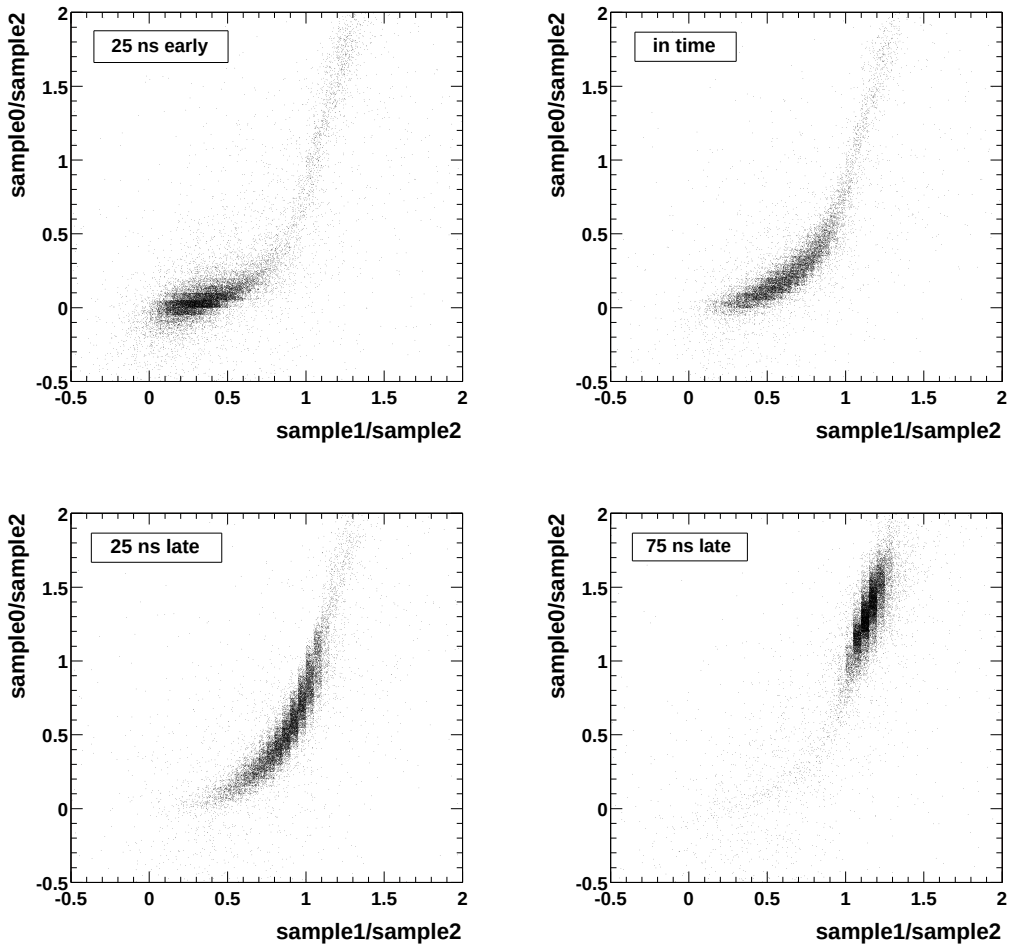

Figure 6.3: Pulse height ratios as determined by the 3 consecutive samples taken by the APV25. Shown are clockwise from the upper left: latency 25 ns too early, at the optimal position, 25 ns too late, and 75 ns too late.

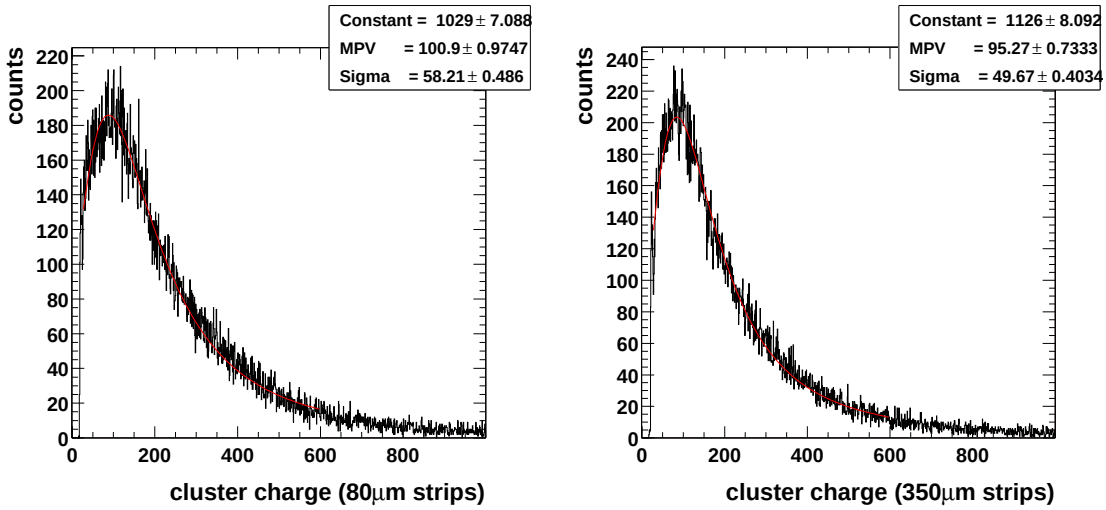

Figure 6.4: Cluster charge distribution on both readout coordinates.

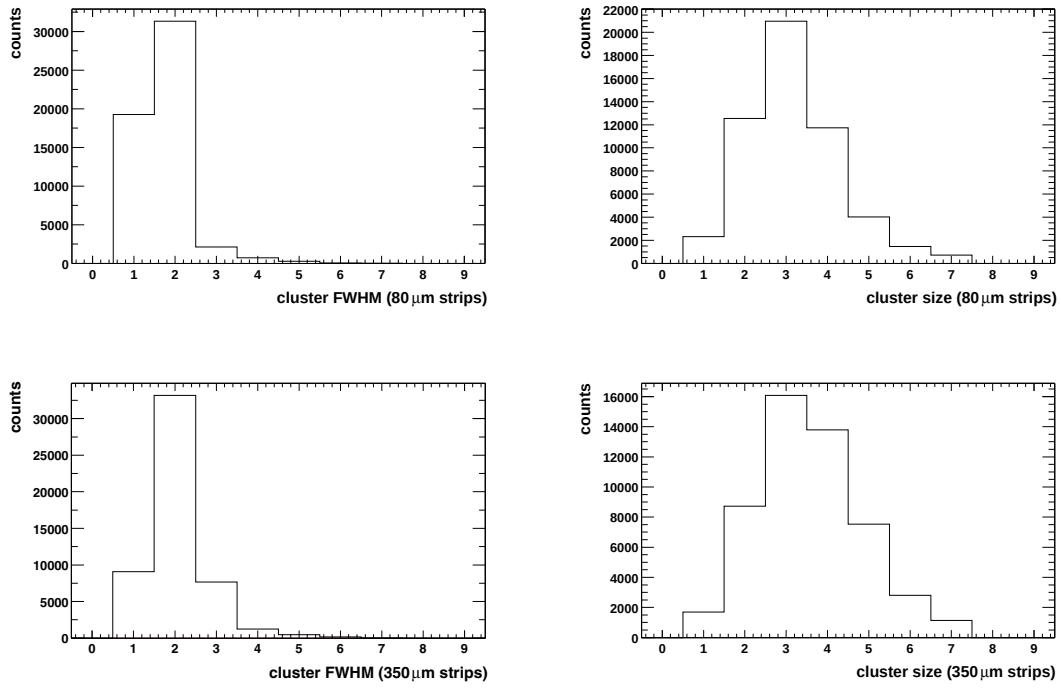

Figure 6.5: Cluster width and cluster size (FWHM) on both readout coordinates.

μm) readout strips is slightly larger (about 0.5 strips), since the charge cloud spreads between the strip layers.

Since the T11 beam has a low particle flux, the hit multiplicity is basically unity. The cluster multiplicity for both coordinates is shown in figure 6.6. Some of the multiple hits are due to reactions of the beam in the material upstream of the detector. Together with the cluster size (strips above threshold), the occupancy can be estimated from these figures.

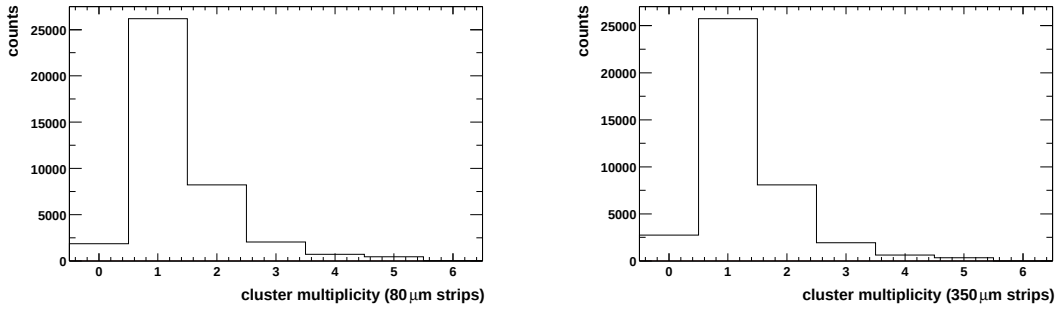

Figure 6.6: Cluster multiplicity on both readout coordinates.

To detect a particle, the signal generated by that particle in the detector has to be well above the noise level of the detector. The cluster noise, defined as the root mean square noise of all strips in the cluster, is shown in figure 6.7. The RMS cluster

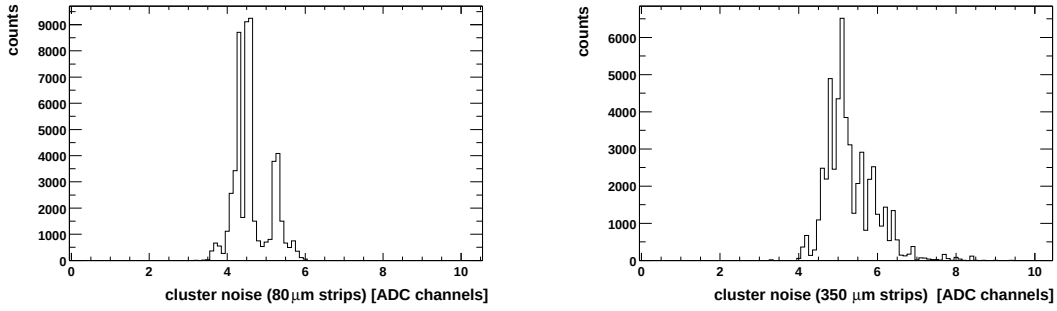

Figure 6.7: Cluster noise on both readout coordinates.

noise is defined in equation 6.1. The noise of the individual channels is measured in separate pedestal runs without particles.

A comparison of the cluster charge (figure 6.4) with the cluster noise shows that the full Landau spectrum is above the noise level, with a most probable amplitude in the order of 100 ADC channels, thus allowing efficient detection of minimum–ionizing particles at nominal settings.

6.5 Offline Analysis

In this section further investigations of the detector properties are presented. They demonstrate the performance of the GEM detectors.

6.5.1 Geometrical Properties

Selecting only events with single hits on both coordinates of the detector it is possible to calculate space points directly from the cluster centers found by the clustering algorithm. With these space points hit maps can be created. These hit maps show geometrical properties of the detector, like the location of spacers and sector boundaries on the GEM foils, and they illustrate the functionality of the central sector.

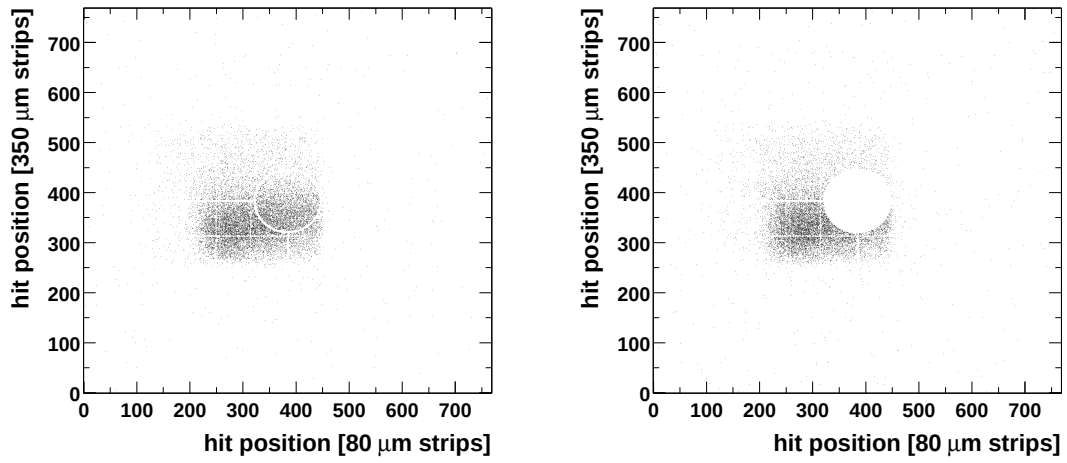

Figure 6.8: Hit maps with central sector on and off. Visible in the left frame are the inner circle of the spacer grid and two of the four bars connecting to it. The thin lines correspond to sector boundaries on the GEM foils (TGEM11).

Figure 6.8 shows hit maps with the central sector activated and deactivated, respectively. The shadow of the big scintillators used for triggering when taking this data is clearly visible. These maps show the inactive regions caused by the spacer grid and by the sector boundaries. The broad lines (horizontal and vertical) leading towards the center of the circular central sector and the circle around this sector are due to the spacer grid. The fine lines are sector boundaries. This figure shows TGEM11, while the other results presented in this section have been obtained with data from TGEM10. Note that TGEM11 was rotated 90° with respect to TGEM10.

Most of the high statistics data samples were taken together with the silicon detector, and to guarantee that a large fraction of all recorded particles passes through the

active area of the silicon detector, the small finger scintillator was added to the trigger. The hit map is shown in figure 6.9. In addition, both GEM detectors were moved slightly to one side. Therefore, the central sector is outside the beam region and is not visible in the hit map.

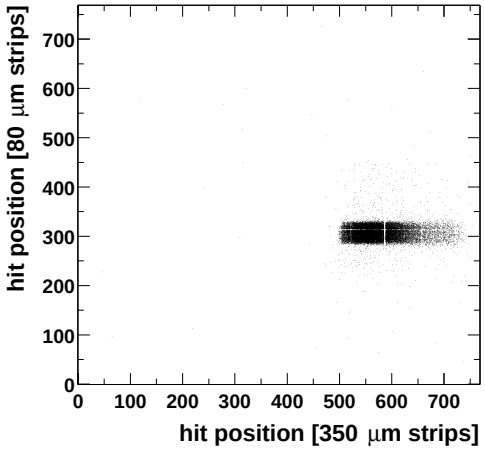

Figure 6.9: Hit map (TGEM10).

It is apparent from the hit maps of figures 6.8 and 6.9 that the dead regions caused by spacer grids, by sector boundaries on the GEM foils, and by dead strips decrease the efficiency of the detector in certain areas and will also have a negative influence on the spatial resolution in these regions. A closer look at these geometric features of the detectors is necessary to show whether an improvement, for example by more elaborate clustering algorithms, is possible.

As a first step, the total charge seen by each strip of the detector was summed up over a full run of $\sim$ 40 000 events. The result of this analysis is shown in figure 6.10. The two histograms are very much like the two corresponding projections

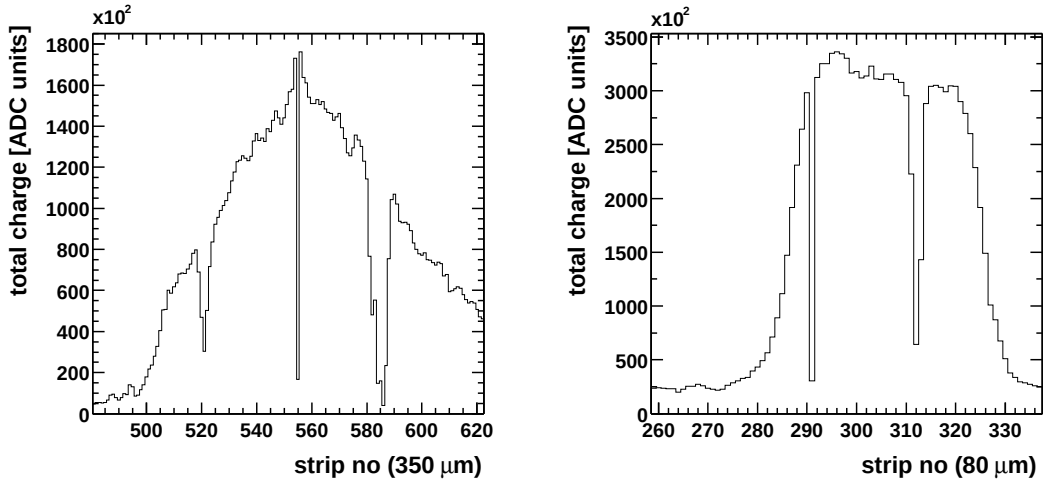

Figure 6.10: Charge in each strip summed up over a full run of $\sim$ 40 000 events, dead strips, spacers and sector boundaries are visible due to charge loss.

of the hit map in figure 6.9, the important difference being that the integral charge is shown and not the sum of the reconstructed hit positions. Even strips where no hits could be reconstructed might have seen some charge, and this allows to evaluate

how much information is really lost due to spacers, sector boundaries, and dead strips. The charge histograms are zoomed to show only the interesting region of the detector, where many particle tracks were recorded.

The detector for which the charge plots were created was TGEM10, oriented in the beam in such a way that the x coordinate is the side with 350 μm wide strips, and the y coordinate is the side with the 80 μm strips. That means that since the sector boundaries of the topmost GEM foil (GEM1, see figure 4.3) are parallel to the 350 μm strips, these boundaries are seen on the x coordinate, while the sector boundaries of the lower two GEM foils (parallel to the 80 μm strips) are seen on the y coordinate.

The different effects of the sector boundaries, depending on the position of the GEM foil, can be seen in the charge plots. On the 350 μm side, a sector boundary in GEM1 can be seen at strip 522, while on the 80 μm side, a boundary in the lower two GEM foils (GEM2 and GEM3) is located at strip 314. The region of charge loss is about one channel wider for the sector boundary in the upper GEM, while the relative charge loss (compared to neighboring channels) is noticeably higher for the sector boundary in the two lower GEM foils.

This can be understood by considering how the sector boundary affects a cluster. A sector boundary in GEM1 reduces the charge in the first multiplication step. Since the cluster spreads on its way down, the effect of the loss of charge is also spread, resulting in a wider region with missing charge. The loss of charge in the strip most affected by the boundary is reduced since charge from clusters outside the boundary region drifts into the affected area.

As far as the sector boundaries of the two lower foils GEM2 and GEM3 are concerned, the argument is exactly opposite. The effect is more localized since the drift path of the electrons is shorter and the cluster is already well developed when entering the second foil. Since there are two sector boundaries on top of each other the loss of charge is rather severe in the most affected strip.

On the 350 μm coordinate, the effect of the spacer grid is clearly visible around strip 584. Here, an area of four strips sees essentially no charge, making it impossible to reconstruct hits on the spacer grid. The reconstruction of hits near the edges of that region, however, might still be slightly improved by more elaborate clustering.

Strip number 556 on the 350 μm side and strip number 292 on the 80 μm side are dead strips, which means they do not see signals, only noise. Dead strips are mainly caused by broken bonds, either on the front–end cards themselves or between front–end card and detector. The noise of the dead channel depends strongly on the position of the missing bond. In figure 6.10, both dead strips are caused by broken bonds between detector and front–end card, leading to an almost normal noise in the strip (compared to very low noise if a bond right on the APV chip is broken). The influence of dead strips on the cluster reconstruction can be reduced

considerably by using a special cluster treatment in the region surrounding a dead strip.

One aspect of the clustering problems around dead strips and sector boundaries is that clusters may be split, thus being recognized as two clusters instead of one. This problem is solved by merging clusters in the critical regions which have peak positions that are less than maximum 3 strips apart.

The problem of missing information due to a broken strip can be overcome by fitting the cluster containing the dead strip with a Gaussian, thus interpolating the missing charge value. This method works very well for dead strips, especially on the 350 μm side, since there the cluster size is bigger and, correspondingly, the fit is better than on the 80 μm side. Figure 6.11 shows a mutilated cluster fitted with a Gaussian. In a case like this, the mean of the fit gives a better result for the position than the center of gravity method. Here, the fit moved the reconstructed hit position from the center of gravity at 557.3 to 556.8. This shift corresponds to 200 μm, which is quite substantial compared to the spatial resolution which is of the order of 50 μm.

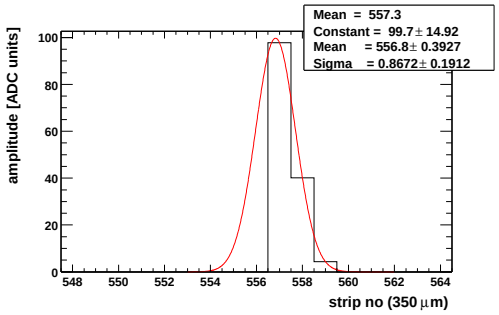

Figure 6.11: Fitted cluster over dead strip (strip no. 556, 350 μm strips).

The success of this method is demonstrated for strip number 556 on the 350 μm side. Figure 6.12 shows a comparison of the hit map without and with fit. It demonstrates

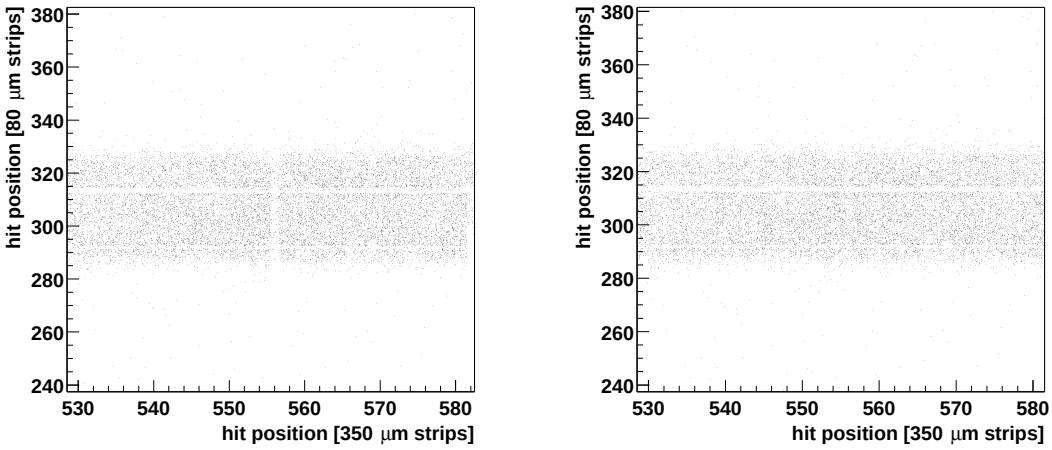

Figure 6.12: Hit map without and with fit for broken strip (TGEM10).

that the position information in the region of the dead strip is recovered to a large extent. In regions of sector boundaries or underneath the spacer bars the success of the fitting method is marginal since an important part of the information is lost. Tests with X–rays show an effect due to charging–up of the sector boundaries. The build–up of charge on the bare kapton in the boundaries changes the electric field and deflects the charge to either side of the boundary. A cluster shifted that way cannot easily be distinguished from a cluster not influenced by the sector boundary on the same position, thus making a recovery of the spatial resolution in the region of a boundary or a spacer extremely difficult. The signal from a particle directly in the center of a boundary will in most cases be lost completely, while hits close to the edge of these structures will be reconstructed in wrong positions. The situation might be improved by more elaborate reconstruction methods that take the displacement of charge into account.

6.5.2 Global Efficiency

By analyzing the data from a single detector, the global efficiency can be determined. This value is averaged over the full area covered by the triggering scintillators. The method to calculate this efficiency is to divide the number of events with at least one cluster found by the total number of incident particles, defined by the number of triggers given by the scintillator. From looking only at the data of one single detector, it is impossible to decide if the particle seen in the detector was the same that triggered the scintillators. For a more precise investigation of the efficiency of the GEM detectors, tracking is needed (see section 7.3). However, the dependence of the efficiency on the voltage over the detector, and thus on the gain, was investigated and is shown in figure 6.13.

On both coordinates the efficiency plateau is reached at a voltage of 4050 V, corresponding to a gain of ~ 8000. At this gain, the signal–to–noise ratio is approximately 20. The efficiency is $\sim 93\%$, due to the insensitive areas introduced by the spacer grid, by sector boundaries, and by dead strips.

Even in the plateau region, the gain still rises slowly with the voltage. This is mainly due to the higher electric fields that improve charge transfer and the higher gain. Clusters in the region of spacer grids and sector boundaries are partially collected on the readout, and can create a signal above threshold. However, these hits are still reconstructed in the wrong position.

6.5.3 Multiple–Hit Capability

When the detector is traversed by more than one particle within the resolution time (in the order of 15 ns),i.e., by particles from the same event, the problem of

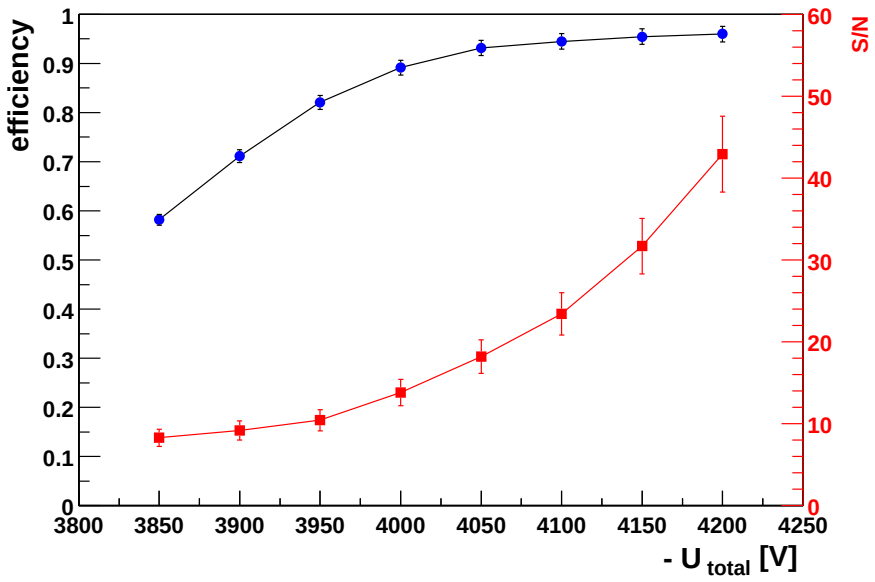

Figure 6.13: Global efficiency and signal–to–noise ratio for the 350 μm side. The noise on the 80 μm side (not shown) is lower, resulting in a better signal–to–noise ratio and slightly higher efficiency (TGEM11).

making the correct assignment of hits on both coordinates to give space points has to be solved. The charge generation is a statistical process that follows a Landau distribution. Thus, each particle in a stream of MIPs creates a different amount of charge and this charge is characteristic for the hit, almost like a fingerprint. The final charge cloud is shared between the two readout planes, so the amplitudes on both planes are correlated.

Figure 6.14 shows this charge correlation and the ratio of the charge deposited on the upper and lower readout plane. The readout board was designed in such a way that this ratio is close to unity, i.e., equal charge sharing. The variance of this ratio is $\sigma \sim 0.1$.

Since this correlation is quite narrow, the unique amplitude information can be used to assign hits on one plane correctly to their partners on the other plane. To resolve multiple hits by correctly assigning clusters on both planes, an algorithm operating on the maximum likelihood principle was developed.

From the measured cluster charge ratio, the probability for any combination of a cluster charge on the 350 μm coordinate (x) and a cluster charge on the 80 μm coordinate (y) of the readout plane can be extracted. It is approximated by the number of entries in the bin of the cluster charge ratio histogram appropriate for the two clusters being tested divided by the integral over the full cluster charge ratio histogram, see right frame of figure 6.14. With these probabilities an $m \times m$ probability matrix is constructed, where m is the hit multiplicity. The probability

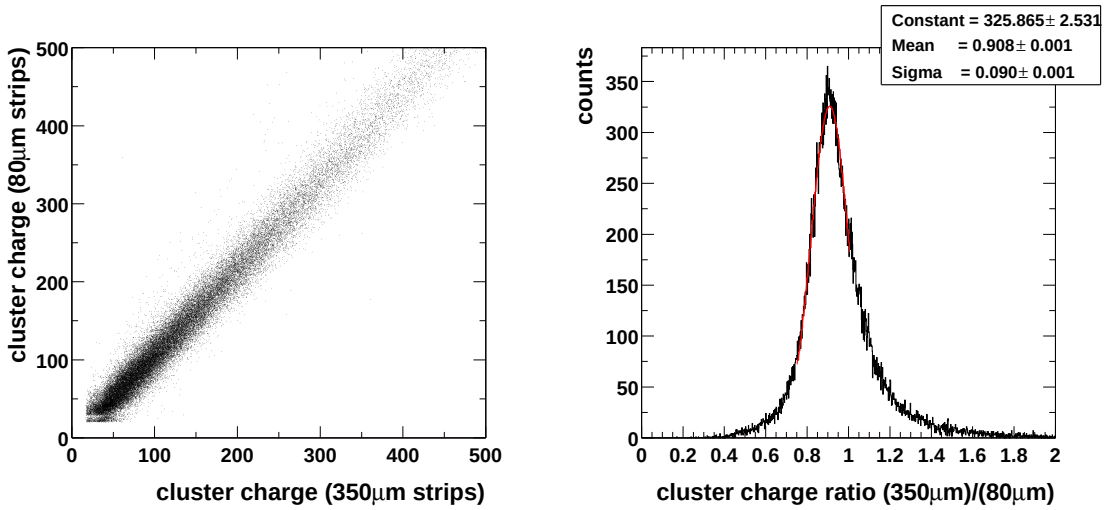

Figure 6.14: Left: charge correlation between readout planes; right: charge ratio (TGEM10).

is given by

$$\mathcal{P}_{i,j} = \frac{h(A_x(i)/A_y(j))}{\sum_{ch} h}. \tag{6.3}$$

Here, $\mathcal{P}_{i,j}$ is the probability, that cluster i on x and cluster j on y belong together, h is the histogram of the cluster charge ratio, with $h(r)$ being the number of entries corresponding to the ratio r, and $A_x(i)$ and $A_y(j)$ are the cluster charges for the i^{th} cluster on x and the j^{th} cluster on y, respectively.

From this probability matrix, the correct assignment of clusters on x and y has to be determined. To do this, the most likely combination has to be found by calculating the likelihood of each possible permutation and choosing the one with the maximum likelihood. There are $k = m!$ permutations, and each permutation corresponds to a different way $\pi_1, \pi_2, ..., \pi_m$ to arrange the integers $1, 2, ..., m$. The likelihood $\mathcal{L}_k$ is defined by

$$\mathcal{L}_k = \prod_{i=1}^{m} P_{i,\pi_i}. \tag{6.4}$$

Here, the indices π_i represent the $1^{st}, 2^{nd}, ..., m^{th}$ element of the permutation k.

Since the algorithm to calculate the likelihood is recursive, the CPU time needed to determine the permutation with the maximum likelihood can be shortened by skipping all subsequent steps once the likelihood at the current level drops below the maximum found so far.

To estimate the efficiency of this algorithm, events with multiple hits were artificially created from the beam data, using single–hit events and combining several of them into one multiple–hit event. In this procedure, the correct assignment between the readout coordinates was known, and could be compared to the output of the algorithm, allowing the evaluation of its performance. Figure 6.15 shows the per-

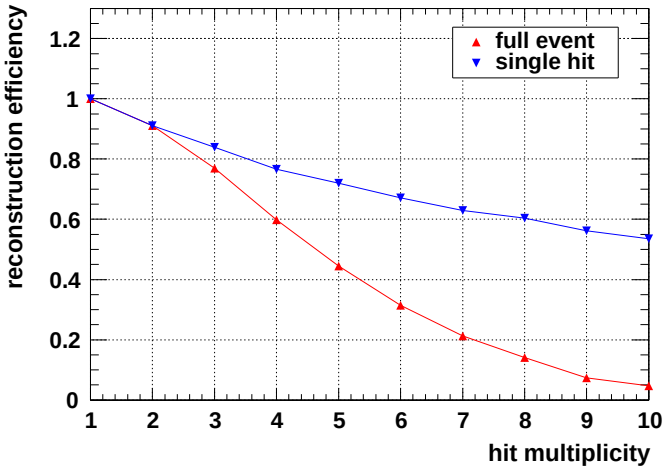

Figure 6.15: Efficiency of multiple hit reconstruction (TGEM10).

formance of the multiple hit reconstruction algorithm for hit multiplicities ranging from one to ten. In this figure, the full–event efficiency is the probability that a full event (all hits) is correctly reconstructed, single–hit efficiency is the probability, that a given hit is correctly reconstructed. The algorithm employed tries out all possible permutations and chooses the one with the maximum likelihood.

The two reconstruction efficiencies in figure 6.15 are related by $\mathcal{R}_{full}(m) = \mathcal{R}_{single}(m) \times \mathcal{R}_{full}(m-1)$, with $\mathcal{R}_{full}$ the full–event efficiency, $\mathcal{R}_{single}$ the single–hit efficiency and m the hit multiplicity. In the case of wrong assignments, one error immediately causes others, as can be seen from $\mathcal{R}_{full}(2) = \mathcal{R}_{single}(2)$. The results in figure 6.15 show that for a hit multiplicity of five for instance, more than 40% of all events are still reconstructed correctly.

The basic track reconstruction algorithm in COMPASS uses only detector projections for the track finding. The excellent charge correlation permits to combine pulse–height correlated hits on the two projections into space points and thus enhances the track reconstruction capability.

Chapter 7

Tracking Performance

The last data runs of the beam test were taken with the full setup, consisting of two GEM detectors (TGEM10 and TGEM11) and a double sided silicon micro–strip detector. The analysis of this data allows the evaluation of the tracking performance of the GEM detectors, the measurement of their efficiency on a sub–millimeter scale, and the investigation of the spatial resolution.

In order to investigate these properties, a program package was developed that is able to calculate particle tracks from the recorded data. These tracks are used in the subsequent analysis of the detector properties.

For the tracking runs, both GEM detectors were operated at their nominal voltage, 4000 V for TGEM10 and 4050 V for TGEM11. This corresponds to a gain of ~ 8000. As trigger the coincidence of all three scintillators is used (see section 6.3.1). The area covered by this trigger can be seen from the hit map on TGEM10 shown in figure 6.9.

7.1 The Coordinate System

In order to determine the tracks of particles with reference to a specific coordinate system, the positions and orientations of all tracking detectors involved have to be known with respect to this coordinate system. The intrinsic coordinates of each detector are given by the orthogonal system of readout strips of the detector. With the geometric arrangement of the detectors as illustrated in figure 7.1, the highest precision can be achieved when studying TGEM10 with the help of tracks generated from data taken by TGEM11 and the silicon detector.

The natural choice for the coordinate system is a system located in TGEM10, with the axes oriented as illustrated by the inset of figure 7.1. The plane z = 0 goes through the center of the drift gap. The origin of the detector–internal x,y–system is assumed to be located in the lower right corner of the readout plane. The x and y

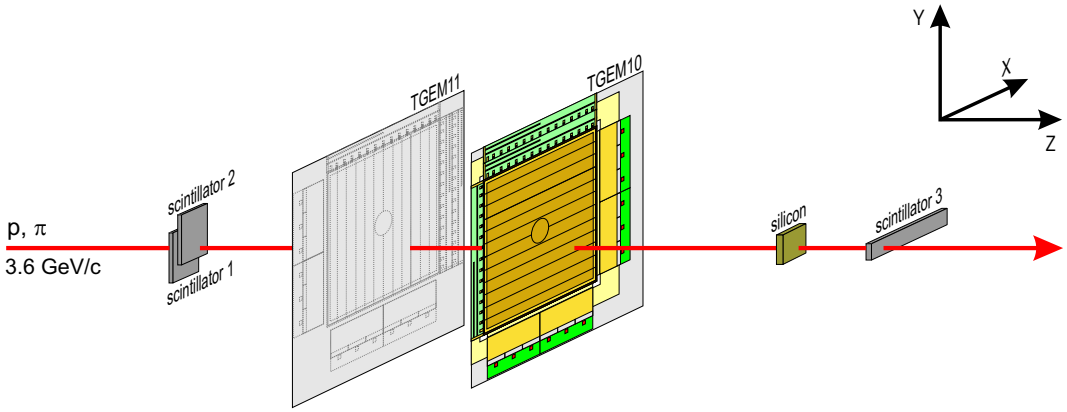

Figure 7.1: Experimental setup in the T11 area, showing the orientation of the detectors and the region where particle tracks are recorded (covered by all three scintillators).

coordinates are measured on the readout plane at z = 7.68 mm. This is illustrated in figure 7.2. Since the beam divergence is 20 mrad in the vertical direction, a displacement of 7.68 mm in the z coordinate corresponds to a displacement in the x,z–plane of up to 150 μm, which is significantly larger than the spatial resolution of the detectors. For a measurement of the spatial resolution it is therefore necessary to have precise knowledge of the z coordinate. The error introduced by the limited precision in z is kept small by selecting only particles in a restricted area, thus effectively reducing the relative divergence of the tracks.

The z coordinates of the other tracking detectors are determined by distance measurements, their x and y coordinates are obtained with the help of particle tracks. Direct measurements of the z coordinate are possible with a precision of $\sim$ 1 mm, which is larger than the uncertainty introduced by the detector–internal location of the z=0 plane.

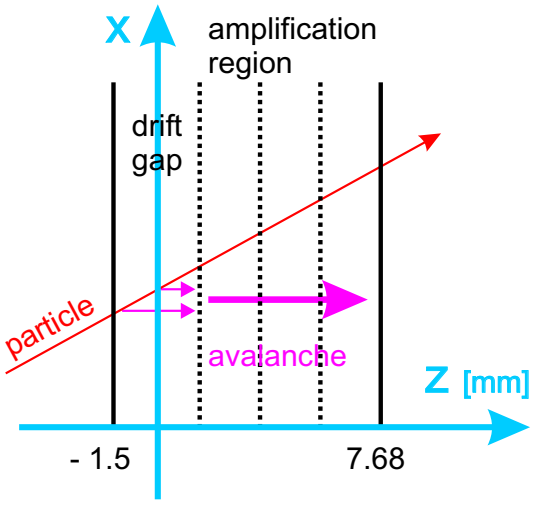

Figure 7.2: Global coordinate system located in TGEM10.

For a rough alignment in the x,y–plane, the hit correlations between different detectors are used. These correlations show the strip number of a hit in one detector versus the strip number of a hit in another detector on the same projection. To get a clean correlation without the ambiguities introduced by multiple hits, only events with single hits in all projections of all detectors are selected. Since the coordinate system is defined by the position of TGEM10, the correlations between

TGEM10 and TGEM11 and between TGEM10 and the silicon are examined. These correlations are shown in figure 7.3.

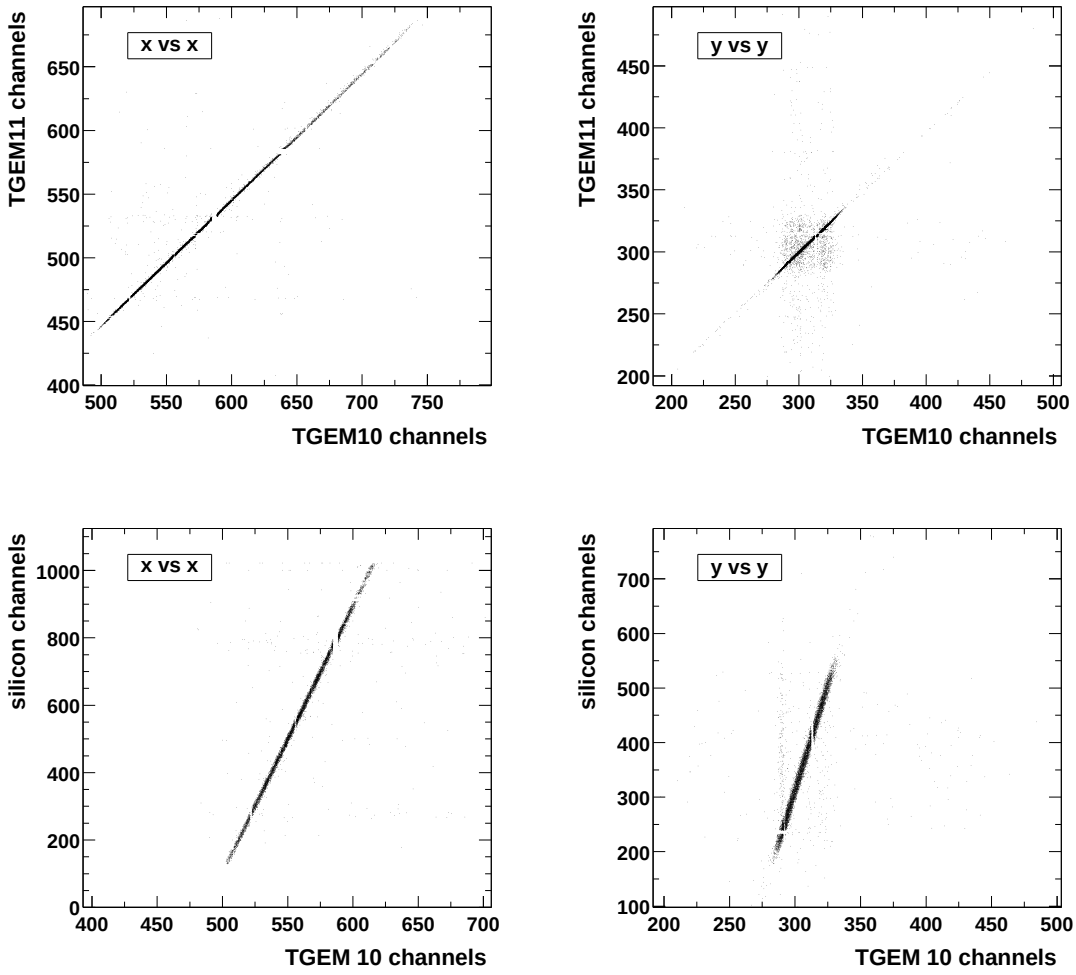

Figure 7.3: Hit correlations for the tracking detectors.

With the assumption that all tracks are parallel to the z axis, the relative positions of the detectors can be extracted from the hit correlations, since in that case each hit should have the same absolute x and y coordinates. The high statistics of the data is exploited by fitting straight lines to the data, thus determining the relative positions of the detectors. The slope of the line is the ratio of the pitches of the two detectors (since the units in figure 7.3 are detector strips), and the offset is the offset of the detector with respect to TGEM10 (also in detector strips). A comparison of the pitch determined from the fit with the real pitch of the detector shows whether the detectors are parallel to each other.

To improve the alignment tracks are generated (see 7.2) from the hits in two detectors and the position of the corresponding hit in the third detector is compared with the point predicted by the track. The offsets of the three detectors are adjusted

according to the discrepancies between prediction and real position. This procedure, however, is only necessary if one wants to determine the absolute position of the particle tracks, for example to study local properties of the detectors, such as efficiency or the influence of spacer grids. For the measurement of the spatial resolution, only the width of the distribution of residuals (distance from the calculated track) is significant, not the common offset due to a displacement in x or y coordinates of the detectors.

The next step necessary to improve the quality of the tracks is to determine the angle of the strips of the silicon detector with respect to TGEM10. This is done by overlaying the hit maps of both detectors in absolute coordinates. Then the angle of the silicon detector is corrected in such a way that the scintillator shadow on the silicon detector is parallel to the shadow on the GEM detector.

Table 7.1 gives the readout pitch of the detectors used in T11, while the parameters determined during the alignment procedure are listed in table 7.2.

Detector	pitch x [μm]	pitch y [μm]
TGEM10	400	400
TGEM11	400	400
silicon	51.75	54.667

Table 7.1: Readout pitch of the detectors

Detector	x [mm]	y [mm]	z [mm]	angle [°]
TGEM10	0	0	0	0
TGEM11	21.69 ± 0.05	0.23 ± 0.05	-99 ± 1	0
silicon	193.24 ± 0.05	112.61 ± 0.05	172 ± 1	-2.5 ± 0.5

Table 7.2: Alignment parameters; the global coordinate system is located in TGEM10, which is mounted on a common support frame together with TGEM11.

7.2 Tracks with FastTrack

To calculate particle tracks from the data and to use them for further analysis of the detector properties, the FastTrack program package was developed. It consists of several sub–programs that provide the different analysis tools used to obtain the results described in this chapter. It is written in C++ based on the ROOT ([30]) data analysis framework and can be executed within the ROOT environment.

Since the detectors are in an area without magnetic field, the trajectories of the particles are straight lines (without taking scattering effects into account, which mainly occur in the material of the detectors). FastTrack connects the hits in the detectors with a straight line and also allows to use two detectors to predict a

hit in the third detector. Figure 7.4 shows ten tracks reconstructed by the FAST-

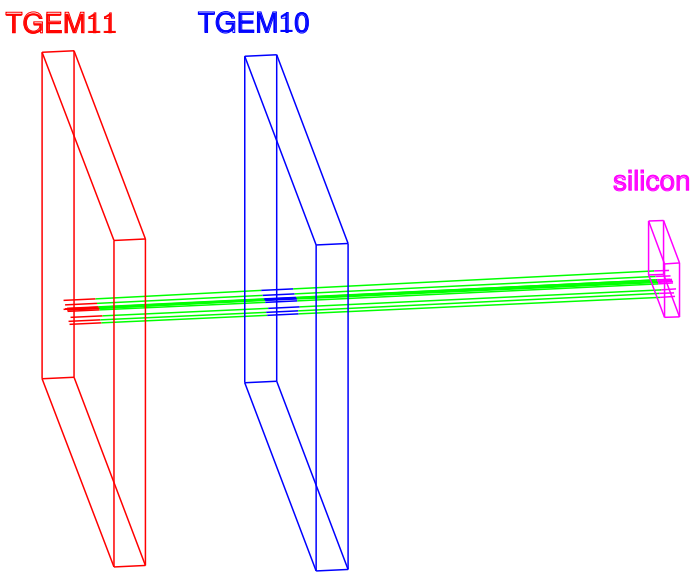

Figure 7.4: Reconstructed particle tracks, the area of the tracks is selected by the overlap of the trigger scintillators.

TRACK program using hits in all three tracking detectors. The contours of the three detectors (TGEM11, TGEM10, and the silicon detector) are drawn as a reference. The region in which tracks are reconstructed is defined by the overlap of the three trigger scintillators.

7.3 Efficiency

With the tracks provided by the FastTrack programs, the efficiency of the GEM detectors can be investigated on a local scale and an efficiency map can be produced. This mapping is not possible in dead areas of the track–defining detectors TGEM11 and silicon.

To evaluate the efficiency in a given region of TGEM10, tracks going through that region are selected and a prediction for the position of the hit in TGEM10 is made. Then it is checked if a hit was found in TGEM10 within a certain distance to the track. This maximum distance was set to 400 μm. The number of hits within the maximum distance to the track divided by the number of tracks going through the region of interest is the efficiency of that region.

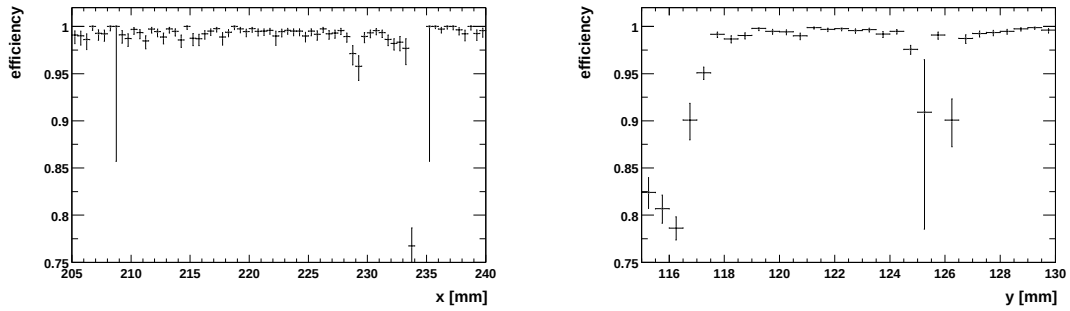

Figure 7.5: Efficiency in both projections of TGEM10, asymmetric errors from hypothesis test (see appendix A).

Figure 7.5 shows the efficiency in both projections of TGEM10. The error bars are determined with a hypothesis test. For a description of the method see appendix A. The size of the errors is influenced by the number of tracks in each bin. This means that in bins with large errors, only a few tracks were reconstructed because of inefficient areas in the track defining detectors. The inefficient region at x $\approx$ 235 mm in TGEM10 is caused by the spacer grid, the reduced efficiency at y $\approx$ 116 mm is due to a sector boundary.

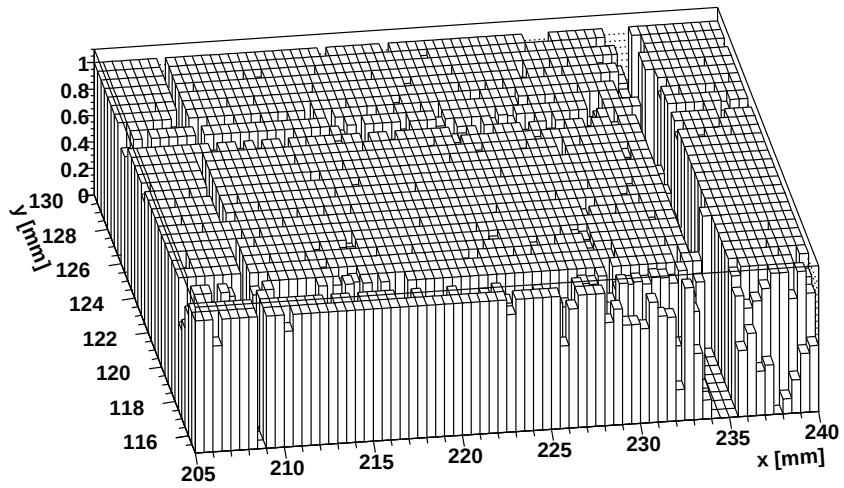

Figure 7.6: Efficiency map of TGEM10, cell size 0.25 mm^2.

The efficiency map of TGEM10 is shown in figure 7.6. The inactive region caused by the spacer grid at x $\approx$ 235 mm and areas with lower efficiency due to sector boundaries are clearly visible. The map was created by computing the efficiency in cells with the size of 0.5 mm $\times$ 0.5 mm.

To obtain the efficiency of TGEM10 in regions without spacers with good statistics, a large area without spacer grid was selected. In this region, for 205 mm $<$ x $<$ 234

mm and 118 mm < y < 130 mm, the efficiency was measured to be $99.0 \pm 0.1\%$.

7.4 Spatial Resolution

In the case of straight tracks, two detectors are sufficient to reconstruct a track. The uncertainty of this track is given by the spatial resolution of the two detectors and by the influence of scattering effects.

From the track reconstructed with two detectors the position of the hit in the third detector can be predicted and compared with the reconstructed position. The difference between predicted and reconstructed position, the residual, contains the track error and the spatial resolution of the third detector. To avoid extrapolation, one of the detectors defining the track should be located upstream, the other one downstream of the investigated detector.

Since TGEM10 is located between TGEM11 and the silicon detector, the spatial resolution of TGEM10 is measured using tracks defined by TGEM11 and the silicon. To limit the effect of alignment errors and dead strips in the silicon detector, only tracks in a small area are selected for the measurement. The distribution of the resulting residuals is plotted in figure 7.7.

Since the distribution of residuals is a convolution of the spatial resolution of TGEM10 and the track uncertainty, the track error has to be determined in order to be able to extract the spatial resolution. Four separate quantities contribute to the track error, namely the spatial resolution of TGEM11, the spatial resolution of the silicon detector, multiple scattering effects in the material of TGEM10, and multiple scattering in air. The two contributions from multiple scattering and the spatial resolution of the silicon detector can be combined into a total uncertainty of the position in the plane of the silicon detector, denoted Δx_{SIL}. The intrinsic resolution of the silicon detector is in the order of ~ 10 μm, the smallest of the three contributions to Δx_{SIL}.

The angular distribution of the particles due to multiple scattering through small angles is to a good approximation Gaussian and is characterized by a root mean square angular uncertainty of [11]

$$\Theta_0 = \frac{13.6MeV}{\beta cp} z\sqrt{x/X_0}\,(1 + 0.038\ln(x/X_0)) \tag{7.1}$$

with a precision better than 11%. Here p is the particle momentum in MeV/c, while βc and z are the velocity and charge number of the incident particle, respectively. In the case of pions of 3.6 GeV/c, $z = 1$ and $\beta \approx 1$, while $x/X_0 \approx 0.71\%$ for a COMPASS GEM detector (see table 4.1). The error in the measurement of the silicon detector due to multiple scattering in TGEM10 can be calculated from the

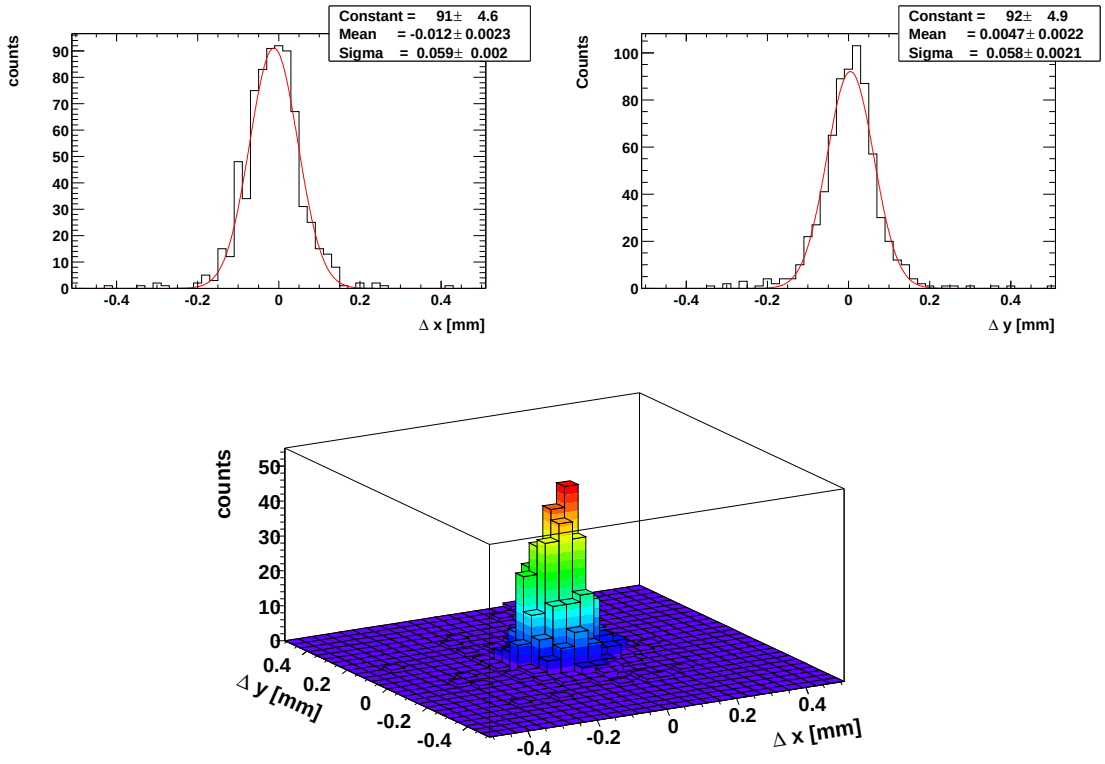

Figure 7.7: Distance of reconstructed hit from track in TGEM10 in both projections and as 3D plot. The widths of the distributions are $\sigma_x = 59 \pm 2\,\mu$m and $\sigma_y = 58 \pm 2\,\mu$m, indicating equal spatial resolution on both readout coordinates.

angle given by equation 7.1. Using the distance $z_{SIL} = 172 \pm 1$ mm between TGEM10 and the silicon one obtains

$$\Delta x_{SIL}^{TGEM10} = \Theta_0^{TGEM10} \times z_{SIL} = 50 \pm 5.5\,\mu\text{m}, \tag{7.2}$$

where the uncertainty of Θ_0^{TGEM10} corresponds to the 11% worst–case estimate [11].

In addition to this contribution, the effect of multiple scattering in air has to be taken into account. The 270 mm of air the particles traverse between TGEM11 (begin of the track) and the silicon detector (end of the track) correspond to $x/X_0 \approx 10^{-3}$. Since the scattering in air is a continuous process along the track, the relation between the error in the silicon detector and the mean scattering angle is modified as compared to Eq. (7.2) [11], resulting in

$$\Delta x_{SIL}^{Air} = \Theta_0^{Air} \times \frac{1}{\sqrt{3}}(z_{SIL} - z_{TGEM11}) = 14 \pm 1.5\,\mu\text{m}. \tag{7.3}$$

Scattering in the entrance foil of the silicon cryostat is negligible due to the small distance between foil and silicon.

Taking the multiple scattering in the material of TGEM10, the multiple scattering in the air and the spatial resolution of the silicon detector into account, the uncertainty in the silicon is

$$\Delta x_{SIL} = 52 \pm 6\,\mu\text{m}. \tag{7.4}$$

To calculate the spatial resolution from the sigma of the distribution of residuals Δx in TGEM10, the error of the track Δx_{Track} in that position has to be determined, using the geometry of the setup. The contributions to this error are illustrated in figure 7.8.

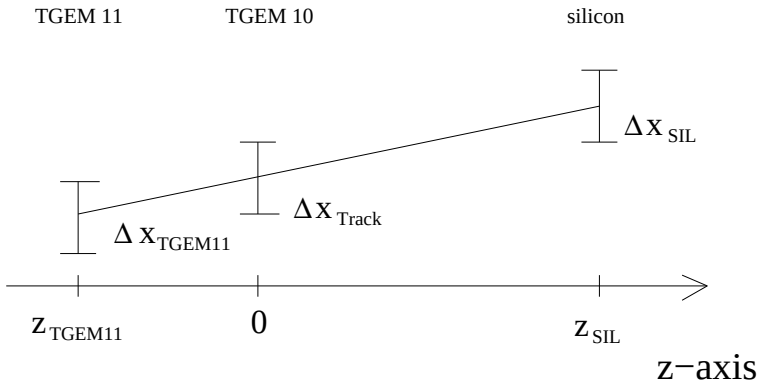

Figure 7.8: Uncertainties contributing to the track error in the z = 0 plane (position of TGEM10); z_{TGEM11} = -99 mm; z_{SIL} = 172 mm.

Starting from the geometry shown in figure 7.8 and with

$$x_{Track} = x_{TGEM11} - \frac{z_{TGEM11}}{z_{SIL} - z_{TGEM11}}(x_{SIL} - x_{TGEM11})\,, \tag{7.5}$$

the track error in the plane of TGEM10 is

$$\begin{aligned}(\Delta x_{Track})^2 &= \left[\frac{z_{TGEM11}}{z_{SIL} - z_{TGEM11}}\Delta x_{SIL}\right]^2 \\ &+ \left[\left(1 + \frac{z_{TGEM11}}{z_{SIL} - z_{TGEM11}}\right)\Delta x_{TGEM11}\right]^2 .\end{aligned} \tag{7.6}$$

The uncertainty of the distribution of residuals Δx is comprised of the track error Δx_{Track} and the spatial resolution of the GEM detector Δx_{GEM},

$$(\Delta x)^2 = (\Delta x_{GEM})^2 + (\Delta x_{Track})^2. \tag{7.7}$$

Using Eq. (7.6) and the assumption that both GEM detectors (the track–defining detector contributing to the track error and the detector under investigation) have the

same spatial resolution on both coordinates ($\Delta x_{TGEM10} = \Delta x_{TGEM11} = \Delta x_{GEM}$), this common resolution is

$$(\Delta x_{GEM})^2 = \frac{(\Delta x)^2 - \left[\frac{z_{TGEM11}}{z_{SIL}-z_{TGEM11}}\Delta x_{SIL}\right]^2}{1+\left[1+\frac{z_{TGEM11}}{z_{SIL}-z_{TGEM11}}\right]^2}. \tag{7.8}$$

With $\Delta x = 58\,\mu$m from the fit to the distribution of the distance from the track, $\Delta x_{SIL} = 52\,\mu$m, and the known geometry of the setup, the numerical value is

$$\Delta x_{GEM} = 46 \pm 3\,\mu\text{m}. \tag{7.9}$$

7.5 Discussion

The beam tests at the T11 experimental area were used to investigate the properties of two COMPASS GEM detectors. The signal properties, such as cluster size and noise where studied extensively. The efficiency was evaluated, confirming the need for a design change of the sector boundaries. The measurement of the spatial resolution demonstrated that the GEM detectors are capable of reaching a resolution better than 50 μm.

However, due to limitations concerning detector availability and time, not all possibilities were explored. The GEM detectors were not installed as stations, with one GEM rotated by 45° with respect to the other. Also, the signal differences due to particles with different energy loss were not studied. By switching the polarity of the beam line magnets, an almost pure pion beam would have been available..

Nevertheless, the essential goals of the beam test were reached. The performance of the readout system was studied in detail. A silicon micro–strip detector was tested simultaneously [35] and the tracking capability of the GEM detectors was investigated.

Chapter 8

First Runs in the COMPASS Spectrometer

From July 2001 on, the GEM detectors were installed in the COMPASS spectrometer and data was taken with a 160 GeV/c muon beam. As long as the final ADCs with zero suppression were not available, the DAQ system had to be run with a large dead time of 1.6 ms to avoid hang ups due to too high a data flow. Since the SPS spill is 4 s long, this limited the number of triggers to 2500 per spill.

In this chapter, the results of two runs recorded with the GEM station GM04 are presented. One run was taken with a low intensity beam ($\sim 10^6$ particles per spill), the other one with a high intensity beam ($\sim 2 \times 10^8$ particles per spill). The station GM04 is located downstream of RICH1.

8.1 The Detectors in the Spectrometer

In the COMPASS spectrometer, the GEM detectors are grouped in stations. Each station consists of two GEM detectors mounted back to back with a separation of 5 mm. One detector is rotated 45° with respect to the other. Every station measures four projections of each track. This enables the tracking algorithm to resolve ambiguities due to multiple hits in the detectors.

The GEM stations are fixed to the large area trackers (straw trackers between SM1 and RICH1, MWPCs further downstream). GEMs and large area trackers together form tracking stations with large angular acceptance and good spatial resolution in the inner region close to the beam. In a later stage it is foreseen to install silicon micro–strip detectors in front of the (inactive) center of the GEM detectors, to have tracking capabilities also inside a high–intensity beam. Figure 8.1 shows the upstream part of the spectrometer with the present positions for GEM tracking stations.

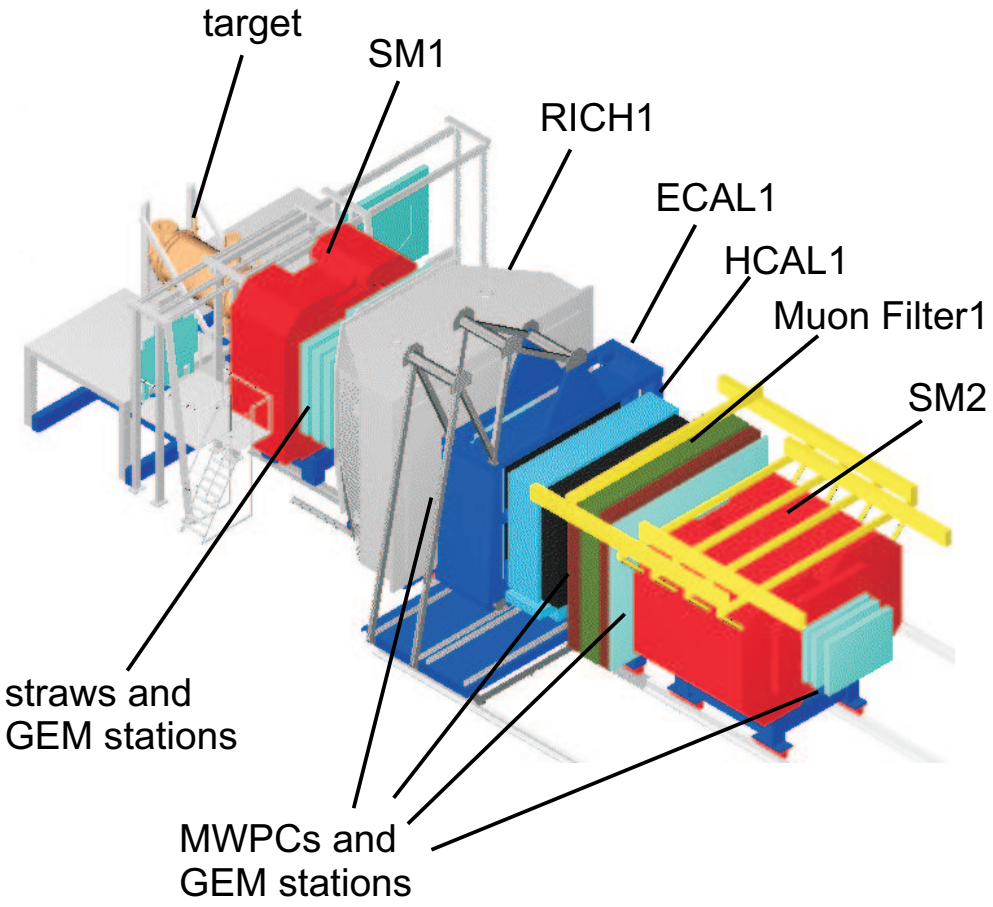

Figure 8.1: Positions of GEM stations in the COMPASS spectrometer.

The gas supply for the detectors comes from a central gas mixing system that guarantees the composition Ar:CO_2 (70/30) and controls the gas flow to the detectors. To minimize the water content of the gas, copper lines (or, where flexibility is necessary, stainless steel flexible tubes) are used up to the outer frames of the tracking stations. Only the last meter is covered with plastic pipes to limit the material in the acceptance.

High and low voltage are supplied from two power supply crates, one located near RICH1, the other one near SM2. That way, the maximum length of the power lines is 15 m, which keeps the voltage drop in the low voltage cables within acceptable limits. In addition, it is important to have the high voltage cables as short as possible to minimize their capacitance. A large capacitance of these cables reduces the ability of the HV power supply to detect discharges in the detector by monitoring for short current surges. In the case of a discharge the HV for the detector should be switched off automatically to protect the GEM.

The GeSiCA modules used to read out the ADCs are located farther away, leading to lengths of up to 90 m for the optical fibers. Differences in length have to be accounted for in the time settings for the individual detector stations.

8.2 Low–Intensity Running

The main purpose of low–intensity runs is to determine the alignment of the detectors in the spectrometer. With the magnets switched off the particles follow straight tracks through the experimental setup (scattering effects being neglected). The low intensity is necessary to avoid multiple hits, making unambiguous track reconstruction straightforward.

8.2.1 Start–Up Phase and Adjustment

Since it was the first time the GEM detectors were operated in the COMPASS beam, the voltage was raised very slowly over a period of one hour. To avoid unnecessary risks the voltage on the detectors was only raised up to 3950 V which corresponds to a gain of ~ 6000. The central sector was activated since the beam passes mainly through this region.

The GEM detectors were included in the COMPASS DAQ system and used the COMPASS trigger. For the low–intensity runs this trigger was derived from a beam counter that intercepted the full beam.

First, the proper timing for the signal had to be determined with a latency scan. The latency that was used for the data taking corresponds to a delay of 1.925 μs. This is the time difference between the passage of the particle through the GEM station and the arrival of the trigger signal at the readout chip. This delay has to be adjusted for each detector station since the different arrival times of the particles, depending on the position of the station, have to be taken into account.

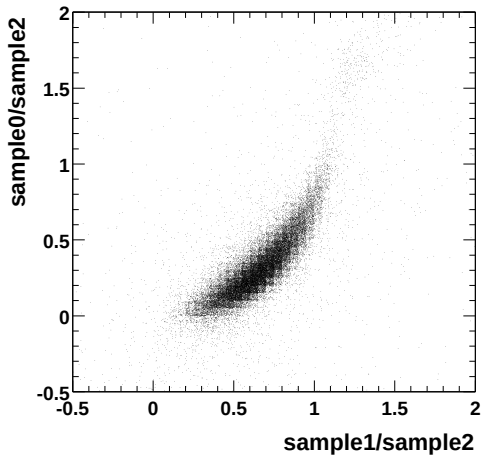

Figure 8.2: Timing plot for low–intensity beam (see section 6.4.2).

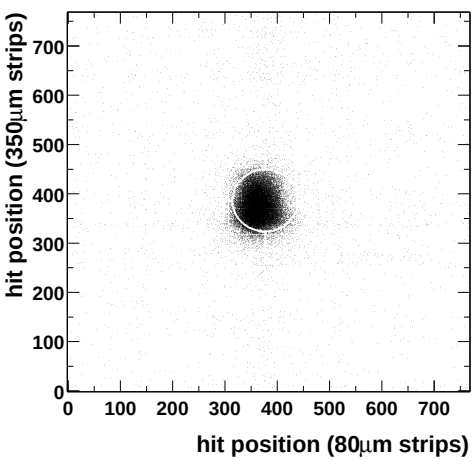

Figure 8.3: Hit map for low–intensity beam, SM1 off.

Figure 8.2 shows the timing plot of the low–intensity data. For an explanation of the timing plot see section 6.4.2. The signals are on their rising edge since the amplitude of the last sample is the highest and the ratio of sample 0 to sample 2 is smaller than the ratio of sample 1 to sample 2. The distribution of the entries along the timing curve is wider than in the test beam because the detector was operated at lower gain, with the effect of a less favorable signal to noise ratio.

The beam profile in the hit map of figure 8.3 is slightly off–center since the detectors are positioned in such a way that the beam goes through the center if the magnets are on. The effect is small since SM1 has a small bending power and since the station GM04 is only 4.9 m downstream of SM1.

8.2.2 Comparison with Test Beam Data

At the test beam in April (see chapter 6), data was taken with a similar beam intensity. This calls for a comparison between results from the low–energy mixed hadron beam at T11 and the high–energy muon beam in the COMPASS experiment.

Influences due to differences in the energy loss of the various particle species involved should be visible in the spectrum of the deposited energy per traversing particle. To serve as a reference, the Bethe–Bloch energy loss of the relevant particles is shown in figure 8.4.

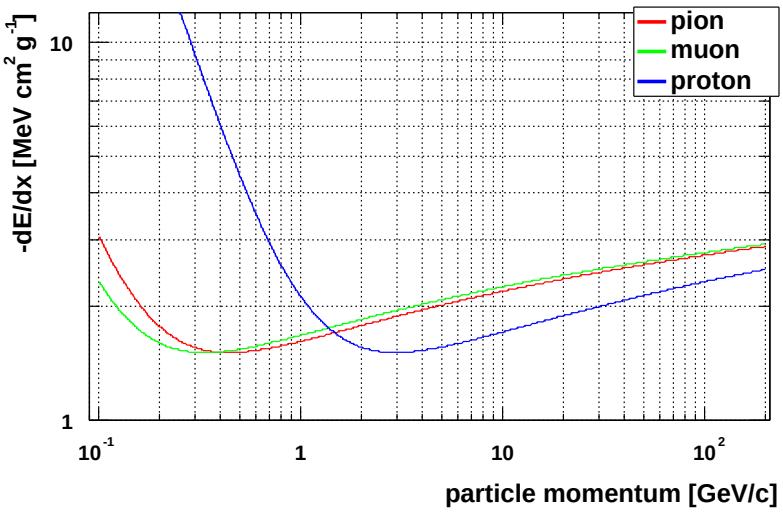

Figure 8.4: Energy loss for pions, muons, and protons in argon, as calculated using the Bethe–Bloch equation [11].

At the momentum of the beam particles in T11, 3.6 GeV/c, the energy loss of pions is $\sim 20\%$ higher than the energy loss of protons, due to the smaller mass and the correspondingly larger $\beta\gamma$ of the pion. Taking the relative intensities in the T11

beam into account (see table 6.1), the average energy loss of a particle in T11 is $\sim$ 1.75 MeV g^{-1} cm^2. The muons in the COMPASS beam have a momentum of 160 GeV/c and correspondingly a higher energy loss due to the logarithmic rise of dE/dx. Their energy loss is 2.9 MeV g^{-1} cm^2, approximately 1.6 times the average energy loss of the particles in T11.

This is reflected in the Landau distribution of the cluster charge in the GEM detectors shown in figure 8.5. For each trigger only one cluster, i.e., the cluster with the

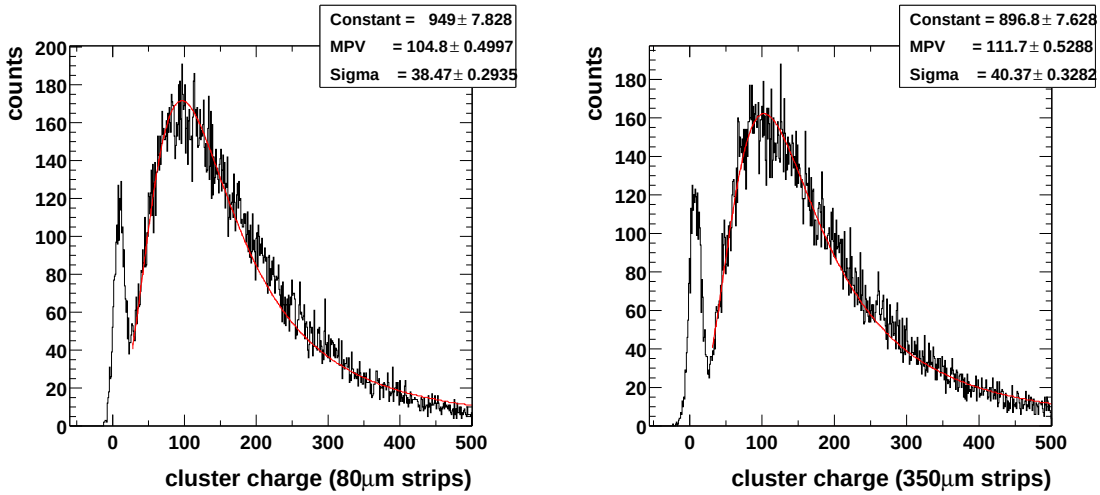

Figure 8.5: Cluster charge on both coordinates with low–intensity beam, no cut on the cluster amplitude.

maximum amplitude, is added to the histogram. The dead region due to the spacer grid around the central sector leads to events without real clusters. In the plot, this gives rise to the noise peak around zero. A good separation between the noise peak and the Landau distribution is apparent, and since the pulse height is comparable to the one in the T11 beam at 99% efficiency, a high efficiency for 160 GeV/c muons is realized even for the reduced gain. However, the gain of the GEM detectors in the COMPASS spectrometer has to be sufficient to detect scattered particles with lower momentum and correspondingly lower energy loss.

Comparing these plots with the Landau spectrum recorded at T11 (figure 6.4), it is apparent that the peak position is $\sim$ 15% higher for the data taken in the COMPASS beam. The gain of the detectors in the muon beam was $\sim$ 6000, compared to a gain of $\sim$ 8000 in T11, but the 60% higher energy loss of the muons more than compensates the lower gain in the muon run. In addition, the fact that the T11 beam contains basically two particle species with almost equal intensity but different energy loss, while the COMPASS beam is a pure muon beam, leads to a difference of $\sim$ 20% in the width of the Landau peak.

The fact that for the cluster charge plot of figure 8.5, the cluster with the highest amplitude is selected may introduce a bias towards higher values. However, with a

beam intensity in the order of 10^6 particles per spill (4 s), the interaction rate was not higher than in the T11 test beam, and about an order of magnitude too low for pileup to contribute significantly.

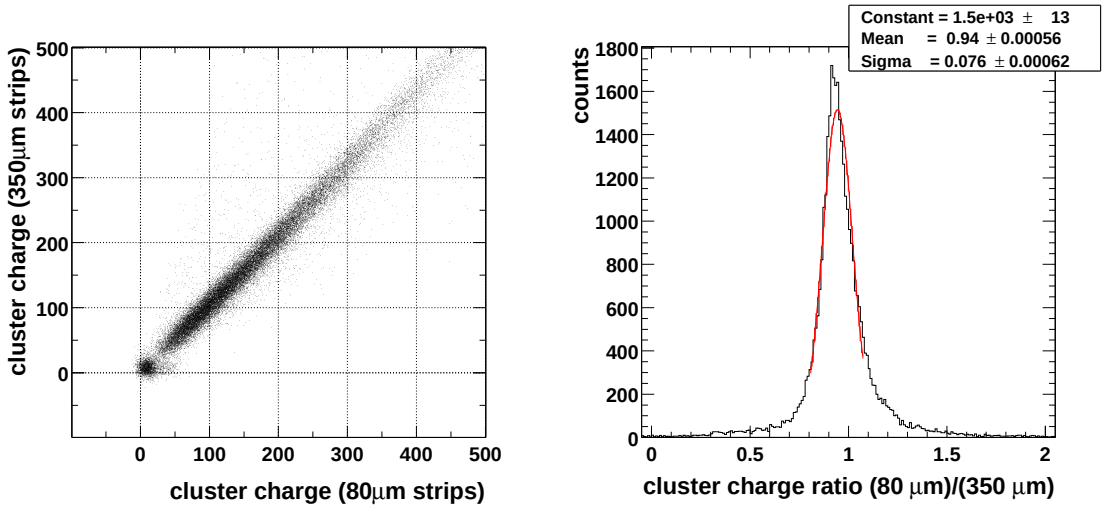

Figure 8.6: Charge correlation between readout planes and charge ratio.

As expected from the test beam data, the correlation between the cluster amplitude on the 80 μm and the 350 μm strips is very sharp, and provides the basis to resolve ambiguities due to multiple hits. The correlation plot and the cluster charge ratio for the low–intensity muon beam are shown in figure 8.6.

8.3 High–Intensity Running

In this section, first results from the operation of GEM detectors in the COMPASS spectrometer running at design beam intensity are presented. As for the low–intensity beam, the voltage was raised with great care, and the measurements were done at a gain of $\sim$ 5000, well below the nominal value of $\sim$ 8000. The central part of each GEM detector has to be switched off in order not to flood the electronics with signals and make hit reconstruction impossible.

To investigate the outer regions of the detectors, the COMPASS trigger covered the region from 25 mm out to 500 mm from the beam and thus triggered mainly on particles which traverse the active region of the GEM detectors. These particles are muons from the beam halo which did not pass through the target material.

Due to multiple hits and pile up of signals in the detector, the timing of the signals in the high–intensity beam is not as clear as in the low–intensity case. The timing plot in figure 8.7 shows signals with the right timing (on the rising edge) in the lower left region of the plot and signals of particles which passed before the particle

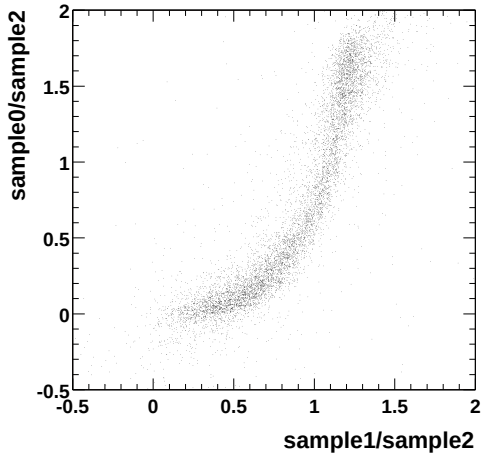

Figure 8.7: Timing plot for high–intensity beam (see section 6.4.2).

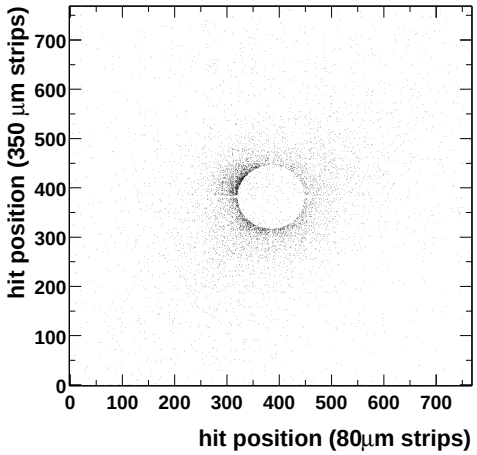

Figure 8.8: Hit map for high–intensity beam, SM1 on.

causing the trigger (on the falling edge) in the upper right region. Signals which are out of time usually are sampled on the falling edge since the fall time of the signal is much bigger than the rise time, making this type of wrong timing more probable.

The hit map in figure 8.8 shows the profile of the beam halo of the high–intensity muon beam. As already demonstrated in the beam test, the deactivation of the central sector of the GEM detectors works reliably.

The Landau spectrum on both projections of the detector for the high–intensity run without a cut on the cluster amplitude is shown in figure 8.9. Due to the reduced

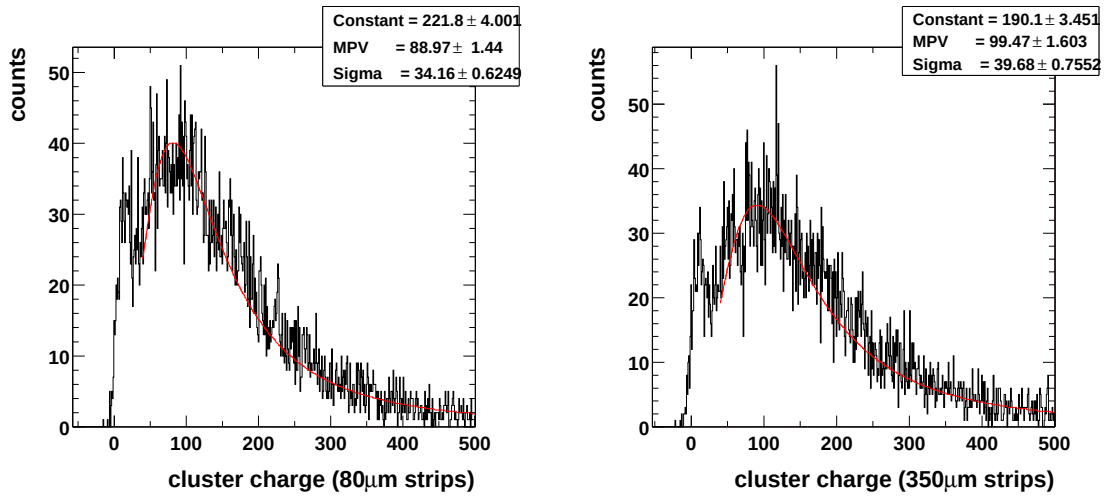

Figure 8.9: Cluster charge on both coordinates with high–intensity beam, no cut on the cluster amplitude.

gain of $\sim$ 5000, compared to $\sim$ 6000 for the low–intensity run, there is no clear

separation from the noise peak. In addition, the charge resolution of the spectrum is deteriorated due to contributions from signals with wrong timing. Again, the width of the Landau distribution is considerably smaller than in the test beam since the beam contained only 160 GeV/c muons.

Chapter 9

Conclusion and Outlook

The commissioning studies presented in this thesis have shown that the GEM detectors constructed for the COMPASS experiment at CERN fulfill the requirements for small area tracking in the spectrometer.

The results of the quality control and test procedures demonstrate that the detectors have a non–uniformity in gain of less than $\pm 15\%$ over their full active area and that they are able to achieve an energy resolution in the order of 20% for Cu X–rays, both findings being the result of the good homogeneity of the GEM foils.

From the data of an extended test of two COMPASS GEM detectors with a 3.6 GeV/c beam of minimum–ionizing protons and relativistic ($\beta\gamma = 25$) pions, important properties of the detectors could be extracted. Due to the excellent charge correlation between the two readout planes (1σ uncertainty below 0.1), events with multiple hits can be resolved with an efficiency of better than 40% for hit multiplicities of up to five in each projection. With a simple tracking analysis, the efficiency of the GEM detectors was measured to be $99.0 \pm 0.1\%$ for MIPs in areas not obstructed by support grids or sector boundaries on the foils. The spatial resolution of the detectors was determined to be $46 \pm 3\,\mu$m.

First results from the operation of the GEM detectors in the COMPASS spectrometer indicate that the detectors perform as expected from the test results. No discharges where seen during the high–intensity muon running, where the detectors have been exposed to 2×10^7 particles/spill from the beam halo.

Still open is the question of the time resolution of the detectors. With the data taken in the 2001 COMPASS physics run, the time resolution can be determined with the help of precise trigger time information to be extracted from the data stream.

An input protection network guards the APV25 front–end chip in the case of discharges in the detectors. Long–term use of the GEM detectors has to show the functionality of this discharge protection, especially in the harsh environment of the hadron beam.

Appendix A

Error Calculation for Efficiency Measurements

The efficiency is a quantity limited by the physical boundaries $\epsilon_{min} = 0$ and $\epsilon_{max} = 1$. Close to the physical limits the Gaussian error prescription $\sigma = \epsilon/\sqrt{N}$ is not applicable. In the formula, ϵ is the sample mean, σ is the square root of the variance, and N is the number of trials.

An efficiency measurement can be described as a repeated trial of a process with two possible outcomes (particle detected or particle not detected). This case is described by the discrete binomial distribution. Given a probability p for success in a single trial the probability $P(r)$ for r successes within N trials is

$$P(r) = \frac{N!}{r!(N-r)!}\, p^r (1-p)^{N-r}. \tag{A.1}$$

The mean and the variance of the binomial distribution are calculated by

$$\begin{aligned} \mu = &\quad \sum_r rP(r) &&= Np \\ &\quad \text{and} \\ \sigma^2 = &\quad \sum_r (r-\mu)^2 P(r) &&= Np(1-p). \end{aligned} \tag{A.2}$$

In an efficiency measurement, the estimator of the mean μ is determined and from the known number of trials the probability $p = \mu/N = \epsilon$ can be extracted. The errors for ϵ are necessarily asymmetric due to the boundary condition. They are determined by calculating the minimum and the maximum p for which the measured ϵ is still within 1 σ. This condition is described by

$$\epsilon_\sigma \pm \frac{1}{N}\sqrt{N\epsilon_\sigma(1-\epsilon_\sigma)} = \epsilon. \tag{A.3}$$

Here, the two solutions $\epsilon_{\sigma\pm}$ describe the two extreme values for the error bar, ϵ is the measured average efficiency. Note that the 1σ deviation in equation A.3 is given

by the square root of the variance defined in equation A.2 divided by N, since the efficiency $\epsilon = \mu/N$ is being determined while the variance in equation A.2 refers to $\mu = N\epsilon$. Solving equation A.3 for ϵ_σ yields

$$\epsilon_{\sigma\pm} = \frac{1+2N\epsilon}{2+2N} \pm \sqrt{\left(\frac{1+2N\epsilon}{2+2N}\right)^2 - \frac{N\epsilon^2}{1+N}}\,. \tag{A.4}$$

The asymmetric uncertainties concerning the local efficiency (figure 7.5) are calculated from equation A.4.

On the physical boundaries $\epsilon = 0$ and $\epsilon = 1$ the size of the error bars decreases with 1/N, while for $\epsilon = 0.5$ the size decreases with $1/\sqrt{N}$. This $1/\sqrt{N}$ dependence shows that in the case of $\epsilon = 0.5$ the Gaussian error prescription is applicable, as expected since the boundaries do not interfere in this case.

Appendix B

Photographs

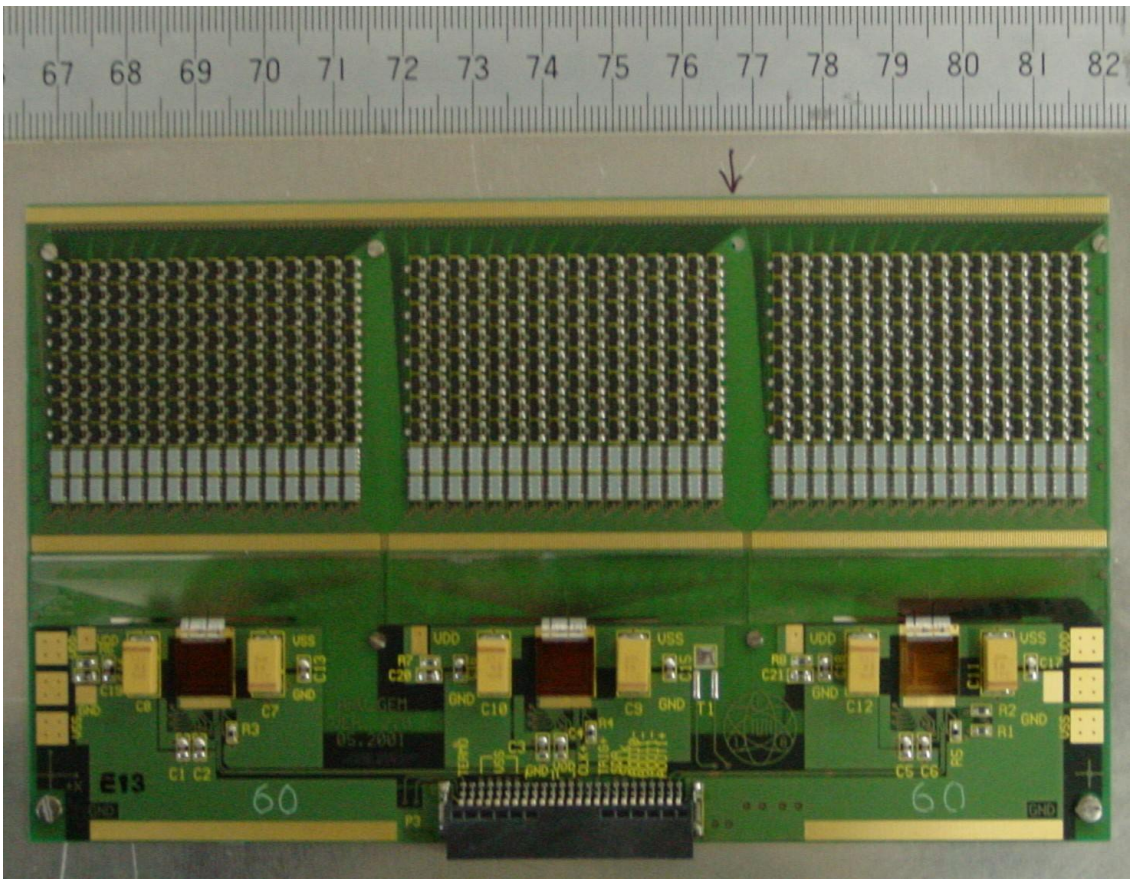

Figure B.1: Layout of front–end card with 384 data channels. Shown are the 3 APVs with their glass pitch adapters and protection circuits, each of the latter comprising a 2×16 array of four–fold capacitors (gray) and an 8×16 array of double diodes (black). The two large capacitors on either side of the APV chips act as noise filters for the power lines.

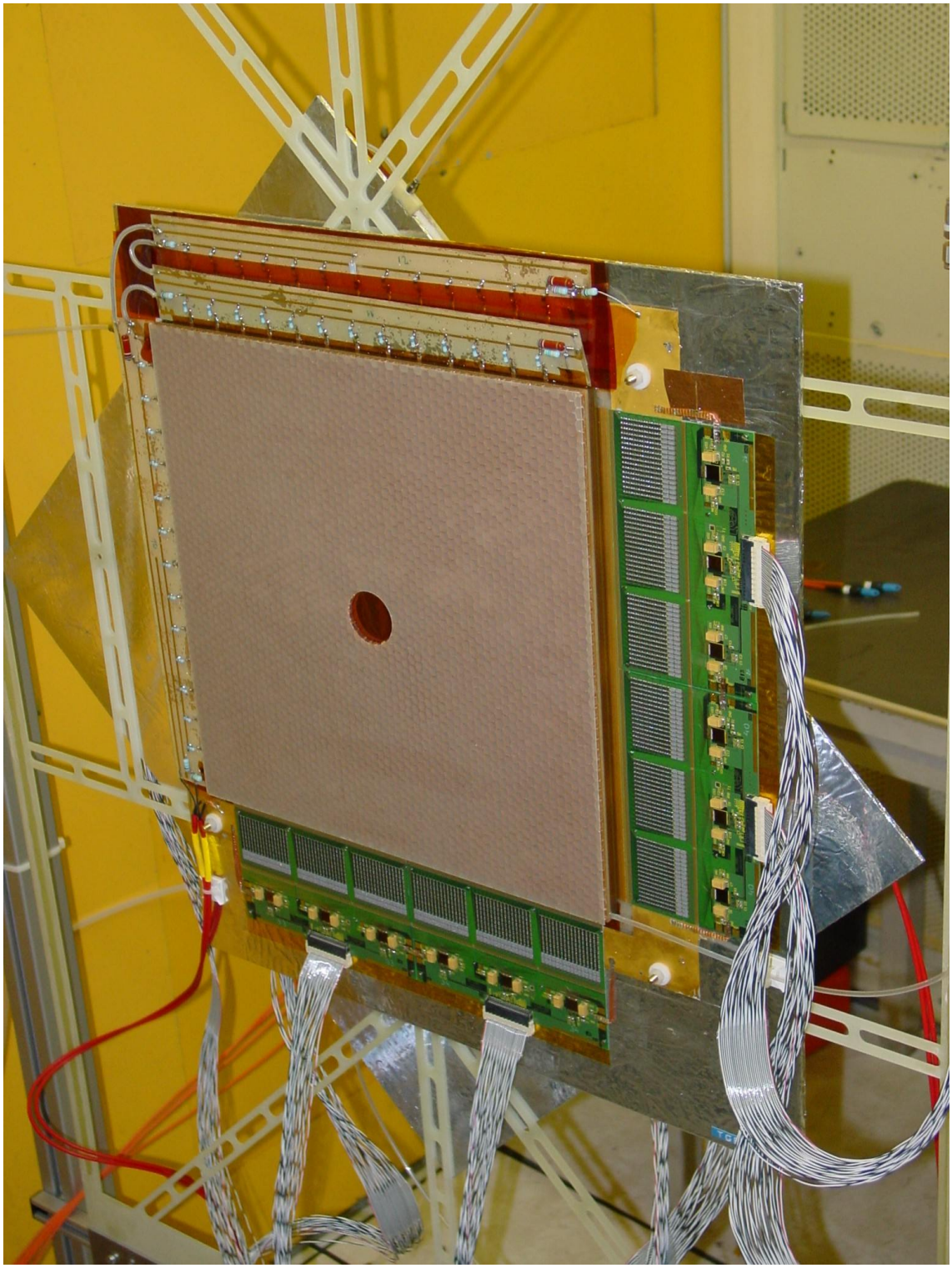

Figure B.2: Complete GEM Station. The HV distribution system (top, left) and the front–end electronics (right, bottom) are visible on the four sides of the front module. The rear module is mounted back to back and is rotated by 45°.

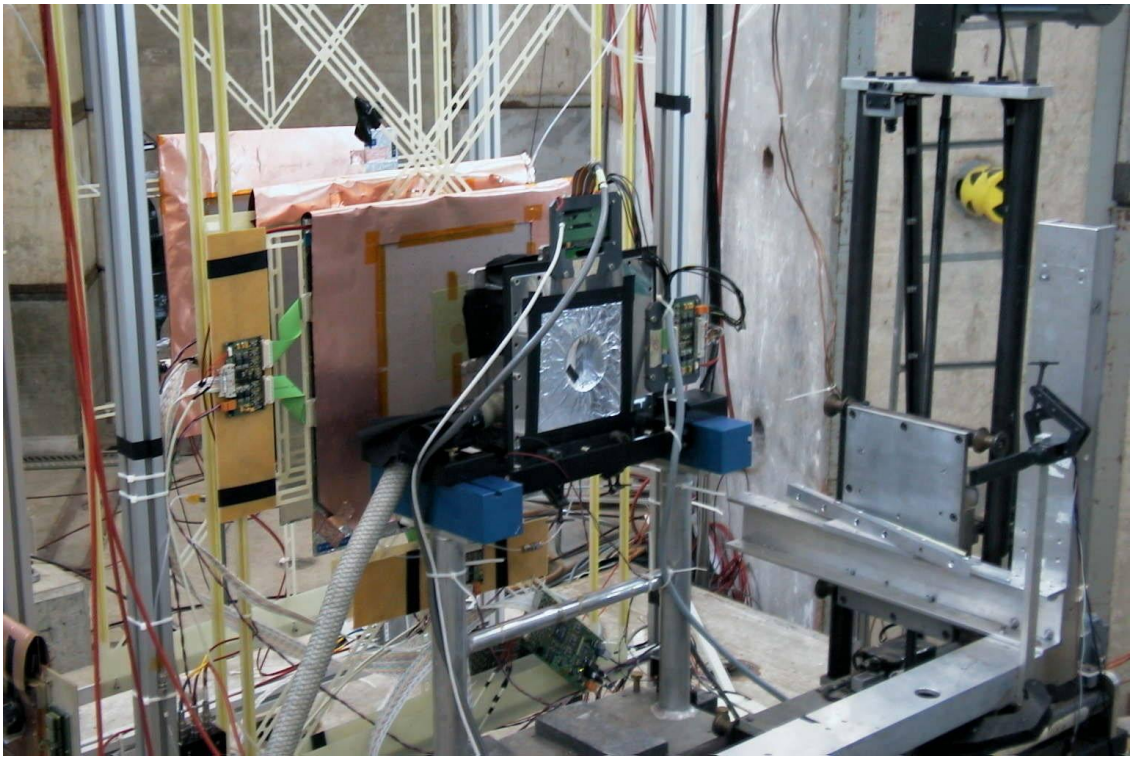

Figure B.3: T11 test beam setup as viewed from the downstream end of the area. The horizontal finger scintillator is visible near the right edge of the picture, while the silicon cryostat and the two GEM detectors TGEM10 and TGEM11 are seen in the center. The third GEM detector located further upstream did not participate in the data taking. The particle beam, traveling through air, enters from the rear.

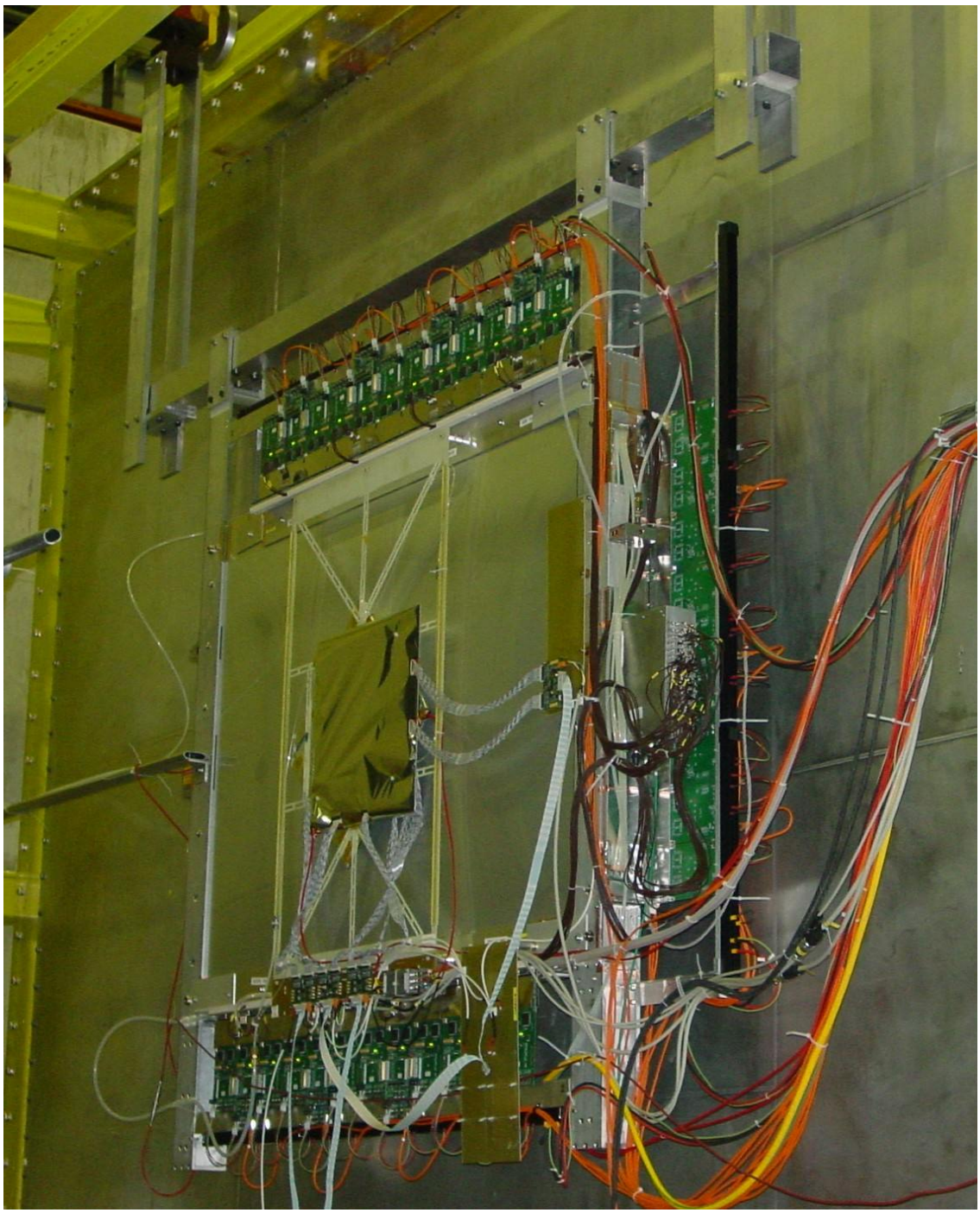

Figure B.4: GEM station GM04 in the COMPASS spectrometer, installed in the center of a MWPC behind RICH1. The GEM station, suspended by a thin stesalit frame, is covered by a 25 μm aluminized mylar noise shielding. One of the four repeater cards is mounted on the right border of the MWPC, the other three and the HV switch on the bottom, outside of the MWPC acceptance.

Bibliography

[1] The COMPASS Collaboration, "COMPASS: A Proposal for a Common Muon and Proton Apparatus for Structure and Spectroscopy", CERN/SPSLC 96-14, SPSC/P 297 (1996).

[2] A. Oed, "Position-sensitive Detectors with Microstrip Anode for Electron Multiplication with Gases", Nucl. Inst. Methods A263, 351 (1988).

[3] F. Sauli, "GEM: A new concept for electron amplification in gas detectors", Nucl. Inst. Methods A386, 531 (1997).

[4] J. Ashman et al., The European Muon Collaboration, "A Measurement of the Spin Asymmetry and Determination of the Structure Function g_1 in deep inelastic Muon-Proton Scattering", Phys. Lett. B 206, 364 (1988).

[5] S.J. Brodsky, J. Ellis, M. Karliner, "Chiral Symmetry and the Spin of the Proton", Phys. Lett. B 206, 309 (1988).

[6] D. Adams et al., The Spin Muon Collaboration, "Spin Structure of the Proton from polarized inclusive deep inelastic Muon-Proton Scattering", Phys. Rev. D 56, 5330 (1997).

[7] P.L. Anthony et al., The E 142 Collaboration, "Deep inelastic Scattering of polarized Electrons by polarized ^{3}He and the Study of the Neutron Spin Structure", Phys. Rev. D 54, 6620 (1996).

[8] A. Airapetian et al., The HERMES Collaboration, "Measurement of the Proton Spin Structure Function g_1^p with a pure Hydrogen Target", Phys. Lett. B 442, 484 (1998).

[9] A.W. Thomas, W. Weise, "The Structure of the Nucleon", Wiley-VCH (2001).

[10] R. Kuhn, "Simulations for the Measurement of the Polarizabilities of the Pion at COMPASS", Diploma Thesis, TU München (2001).

[11] D.E. Groom et al., Particle Data Group, "Review of Particle Physics", Eur. Phys. J. C 15, 1 (2000), `http://pdg.lbl.gov/`.

[12] F. Sauli, "Principles of Operation of Multiwire Proportional and Drift Chambers", CERN 77-09 (1977).

[13] M. Pieroth, J. Friedrich, P. Semmel, N. Voegler, J. LeRose, D. Zimmerman, "Radiation Tail in Electron Scattering: Approximations in the Calculation and Comparison to Measurements", Nucl. Inst. Methods B36, 263 (1989).

[14] G. Knoll, "Radiation Detection and Measurement", 3rd edition , Wiley (1999).

[15] K. Kleinknecht, "Detektoren für Teilchenstrahlung", B.G. Teubner (1984).

[16] W.R. Leo, "Techniques for Nuclear and Particle Physics Experiments", Springer (1987).

[17] A. Peisert, F. Sauli, "Drift and Diffusion of Electrons in Gases: A Compilation", CERN 84-08 (1984).

[18] B. Schmidt, "Microstrip gas chambers: Recent developments, radiation damage and long-term behavior", Nucl. Inst. Methods A419, 230 (1998).

[19] S. Bachmann, A. Bressan, L. Ropelewski, F. Sauli, A. Sharma, D. Mörmann, "Charge amplification and transfer processes in the gas electron multiplier", Nucl. Inst. Methods A438, 376 (1999).

[20] A. Bressan, M. Hoch, P. Pagano, L. Ropelewski, F. Sauli, S. Biagi, A. Buzulutskov, M. Gruwé, G. De Lentdecker, D. Mörmann, A. Sharma, "High rate behavior and discharge limits in micro-pattern detectors", Nucl. Inst. Methods A424, 321 (1999).

[21] S. Bachmann, A. Bressan, M. Capéans, M. Deutel, S. Kappler, B. Ketzer, A. Polouenkov, L. Ropelewski, F. Sauli, E. Schulte, L. Shekhtman, A. Sokolov, "Discharge mechanisms and their prevention in the gas electron multiplier (GEM)", CERN-EP/2000-151 (2000), submitted to Nucl. Inst. Methods.

[22] B. Grube, "The Trigger Control System and the Common GEM and Silicon Readout for the COMPASS Experiment", Diploma Thesis in preparation, TU München (2001).

[23] L.L. Jones, M.J. French, Q. Morrissey, A. Neviani, M. Raymond, G. Hall, P. Moreira, G. Cervelli, "The APV25 Deep Submicron Readout Chip for CMS Detectors", CERN-99-09 (1999).

[24] L.L. Jones, "APV25-S0 User Guide", `http://www.te.rl.ac.uk/med/`.

[25] M. Wiesmann, "Status of Silicon Detectors", Talk at the COMPASS Collaboration Meeting (September 2000).

[26] I. Konorov, private communication (2001).

[27] H. Fischer, J. Franz, A. Grünemaier, F.H. Heinsius, M. Hoffmann, F. Karstens, W. Kastaun, K. Königsmann, M. Niebuhr, M. Parr, R. Risken, T. Schmidt, H. Schmitt, A. Schweimler, J. Urban, M. von Hodenberg, I. Konorov, L. Schmitt, "The COMPASS Online Data Format", COMPASS Note 2001-8 (2001).

[28] PerkinElmer Instruments, `http://www.ortec-online.com/`.

[29] S. Kappler, CACO (2001).

[30] R. Brun et al., "ROOT Users Guide v0.7.2" (2001), `http://root.cern.ch/`.

[31] D.R. Lide, H.P.R. Frederikse (eds.), "CRC Handbook of Chemistry and Physics", 75^{th} edition, CRC Press (1994).

[32] CERN ALICE DAQ group, "ALICE DATE User's Guide, DATE 3.7", ALICE Internal Note/DAQ ALICE-INT-2000-31 v.2 (2001).

[33] B. Ketzer, gemMonitor (2001).

[34] J. Friedrich, private communication (2001).

[35] R. Wagner, "Commissioning of the Silicon Detectors for the COMPASS Experiment", Diploma Thesis in preparation, TU München (2001).

[36] National Institute of Standards and Technology, "Physical Reference Data", `http://physics.nist.gov/`.

Most of the work described in this thesis was done during a 10 months' detachment to CERN, where I stayed in the Gas Detector Development Group of Fabio Sauli. At this time, the design of the GEM detectors was already frozen. The mass production of the detectors was beginning in the EP-TA1 workshop.

I developed the quality control procedure for the detectors and performed the X–ray measurements for four modules. I tested the front–end electronics of the detectors and set up the readout tests with the beta source, again investigating four GEMs. I made a substantial contribution in the setup phase and took an important role during the two weeks long beam test at the PS accelerator, where the properties of two detectors were studied with minimum–ionizing particles. For the analysis of the test beam data I enhanced the existing cluster recognition software and developed the multiple hit simulation and the FastTrack tracking package. This software was instrumental for my extensive study of the efficiency, the multiple hit capability, and the spatial resolution of the GEMs. From July 2001 on, I took responsibility for the installation of 7 GEM stations in the COMPASS experiment at the SPS accelerator. I participated in the data taking during the COMPASS physics running and analyzed the data from the running–in of the GEMs.

Acknowledgements

I am grateful to Prof. Stephan Paul for proposing this interesting subject and for supporting my stay at CERN.

I thank Fabio Sauli for accepting me in his group at CERN, Bernhard Ketzer for supervising my work, Leszek Ropelewski, Steffen Kappler, Klaus Dehmelt, and Cem Altunbas for helpful advice and encouragement.

I am specially indebted to Igor Konorov and Boris Grube for their work on the electronics that turned the April 2001 test beam into a success. Further, I want to thank the Munich silicon team Michael Wiesmann, Rita de Masi, and Robert Wagner for their support during the beam time. Jan Friedrich was helpful for all kinds of questions. Sincere thanks to Roland Kuhn for support in programming matters and for good company during night shifts.